Università degli Studi di Pisa
Facoltà di Scienze Matematiche Fisiche e Naturali

Galileo Galilei School of Graduate Studies
Course of Applied Physics

Precision gravity measurements with atom interferometry

Ph.D. Thesis (XXIV° ciclo)
SSD - FIS/03

Candidate

Gabriele Rosi

Supervisors

Prof. Guglielmo M. Tino

Prof. Nicolò Beverini

2012

Contents

Chapter 1

Introduction

1.1 Matter-wave interferometry

Matter-wave interferometry has led to the development of new techniques for the measurement of inertial forces, finding important applications both in fundamental physics and in applied research. The remarkable stability and accuracy that atom interferometers have reached for acceleration measurements can play a crucial role for gravimetry. Atom interferometry is used for precise measurements of gravity acceleration [1, 2], Earth's gravity gradient [3, 4] and rotations [5]. Accelerometers based on atom interferometry have been developed for many practical applications including metrology, geodesy, geophysics, engineering prospecting and inertial navigation [6]. Ongoing studies show that the space environment will allow to take full advantage of the potential sensitivity of atom interferometers [7]. Recently, new interferometer schemes based on multiphoton transitions have been demonstrated [8] and further sensitivity improvements in measuring inertial force are expected. Moreover, general relativity tests at unprecedented precision level have been also proposed [9]. In this context it is clear how atom interferometry plays a crucial role in both fundamental and applied physics.

The first-matter wave interferometer was realized in 1947 by Enrico Fermi [10]. In that experiment slow neutrons were Bragg diffracted by crystal planes with different chemical composition; the relative sign of the neutron scattering length from different nuclei was measured. Some years later the first matter-wave interferometry experiment on electrons was performed using a Mach-Zehnder scheme, with crystals of few hundreds of atomic layers as mirrors [11, 84, 83]. At that time it was already clear that neutral matter was more adequate than charged particles or photons for realizing high sensitivity devices for acceleration detection. The reasons lie in the lower sensitivity with respect to perturbing electric and magnetic fields than charged particles. Moreover, typical speed can be much lower than c, allowing a longer interaction time within a fixed length scale. Neutrons were difficult to produce in laboratories because accelerators are needed; atoms, on the other side, do not easily penetrate matter and are easily blocked from surfaces. Matter wave interference patterns from atoms, as more complex and massive system, were observed in 1990s and several groups around the world started to realize atom interferometers experiments [12, 13, 14, 15]. In the first experiments that demonstrate the power of atom interferometry for accurate measurements of the Earth's gravity acceleration [1] and its gradient [3, 4], the separation and reflection of the atomic wave packet are achieved by using Raman atom interferometry, that is by inducing a Raman transition between internal states of the atoms by an electromagnetic field [16]. Two counter-propagating beams, with propagation vectors k_1 and $k_2 \sim -k_1$, whose frequency difference is resonant with an atomic two-level system (typically the ground-state hyperfine levels of alkali) , can drive a two-photon Raman transition. The internal state of the atom and its momentum are always coupled, as a consequence of momentum and energy conservation in the system atom+photons. Optical pulses are used to stimulate Raman transitions between states. These light pulses act on the atom matter-waves like mirrors and beam-splitter act on the light-wave in an optical interferometer. The resulting phase difference accumulated along the atom interferometer paths is given by

$$\phi = \vec{k}_{\text{eff}} \cdot \vec{a} T^2 \tag{1.1}$$

whenever an acceleration a is present and where $k_{\text{eff}} = k_2 – k_1 \sim -2k_1$ and T is the temporal separation between two interferometer pulses. Such method of using light pulses as beam splitters and mirrors proved to be advantageous and the second generation of atom interferometers mainly made use of this principle. Measurements of astonishing precision and with comparable – if not better – performance than state of the art classical instruments have been made, namely, by the two groups of Steven Chu and Mark Kasevich. Using atom interferometry, they were able to measure Earth gravity g with a precision of $2 \times 10^{-7}\text{m/s}^2/\sqrt{\text{Hz}}$ [6], Earth gravity gradient with a precision of $4 \times 10^{-8}\text{s}^{-2}/\sqrt{\text{Hz}}$ [17, 18] and rotations with an angular resolution better than $10^{-9}\text{rad/s}/\sqrt{\text{Hz}}$ [19].

In parallel, a third generation of atom interferometers, designed for new applications, has been developed [20, 21]. In particular, this thesis has been carried out on a gradiometer for the measurement of the Newtonian gravitational constant G in Florence [22].

1.2 The MAGIA experiment

1.2.1 Motivations

Nowadays most of the physical constants are known within a few parts per billion, in the worst cases some parts per million. One of the few exceptions is the Universal Gravitational Constant G, introduced for the first time by Newton in 1665 to describe the attractive force between all bodies with mass. Despite

$$|F| = G\frac{m_1 m_2}{r^2} \tag{1.2}$$

is one of the most known among all the physical laws, the last CODATA-recommended value of G has still a relative uncertainty of 1.2×10^{-4}:

$$G = 6.67384(80) \times 10^{-11}\,\text{m}^3\text{Kg}^{-1}\text{s}^{-2}\,(\text{CODATA}\,2010)$$

Starting with the first measurements at the 1% level [23], declared uncertainties were gradually reduced to $10^{-5}G$ [24]. Even considering the most recent ones though [25, 26, 27, 28, 29, 30, 31, 32], the results differ by several parts in 10^{-4} (see figure 1.1). Besides the purely metrological interest, there are several reasons why a more precise determination of G is important: in astronomy, the factor GM of astronomical objects can be determined extremely well and thus a better knowledge of G leads to a better knowledge of M, which in turn leads to a better physical understanding of celestial bodies; in geophysics, uncertainties of density and elastic parameters of the Earth

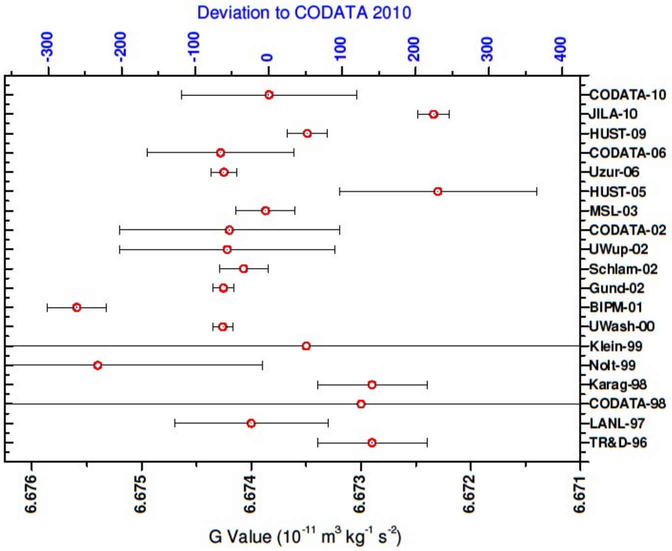

Figure 1.1: Published results of recent G measurements, together with the CODATA recommended 1998, 2002 and 2006 values. Relative deviation with respect to the last CODATA recommended value (2010) is also shown.

are directly related to the uncertainties on G; in theoretical physics, spatial variations of G are predicted by some theories; moreover, string theory assumes additional dimensions rolled up at small distances, causing a breakdown of the inverse square law of gravity.

The reasons for the difficulties in the determination of G can be found in the completely different nature of the gravitational force from the other forces: gravity cannot be shielded or compensated for. This very special property makes it the dominating force in the regimes of large neutral masses and large distances but the very same characteristic makes it very hard to measure in laboratory experiments. Its weakness allows other forces to contribute with big systematic effects in laboratory experiments. Furthermore the knowledge of G directly depends on the precision and accuracy in the determination of the induced gravitational field, so the position of the source masses and their density distribution are crucial parameters, but it can be difficult to accurately characterize them. Secondly, the majority of the experiments performed so far are based on macroscopic suspended masses; systematic effects and parasitic couplings in suspending fibers are not well understood and could be responsible for the observed discrepancies. There are only few methods, which do not rely on a torsion pendulum and there has been only one free fall experiment without any suspension [33], based on an optical Michelson interferometer with a free-falling corner cube on one interferometer arm. The large uncertainty level reached ($1.5 \times 10^{-3}G$) is due to the difficulty to characterize the behavior of a macroscopic mass (the falling corner). In particular, it is very difficult to isolate the contribution of the gravity attraction from effects produced by spurious electromagnetic fields. Instead, using microscopic masses as neutral atoms to probe the gravitational field generated by a well characterized source mass can solve this kind of problems. For all these reasons, atom interferometry represents an alternative and powerful method to attempt a new G determination.

1.2.2 Overview of the experiment

In the MAGIA experiment [34, 22] atom interferometry is used to perform a simultaneous measurement of the differential acceleration experienced by two clouds of cold rubidium atoms in the presence of a well characterized set of source masses. The measurement, performed for two different positions of the source masses, allows to determine the Newtonian gravitational constant from the precise knowledge of the source masses distribution.

Figure 1.2 shows a schematic of the MAGIA experiment.

The gravity gradiometer setup and the configurations of the source masses, C ("close") and F ("far") are visible. These two sets are symmetrically arranged around a vertical tube which defines the interferometer region. At the bottom of the apparatus, a magneto-optical trap (MOT) with beams oriented in a 1-1-1 configuration collects ^{87}Rb atoms. Using the moving molasses technique, the sample is launched vertically along the symmetry axis of the vacuum tube and cooled down to a temperature of about 2 μK. The gravity gradient is probed by two atomic clouds moving in free flight along the vertical axis of the apparatus and simultaneously reaching the apogees of their ballistic trajectories at 60 cm and 90 cm above the MOT. Shortly after launch the two atomic samples are velocity selected and prepared in the proper state using a combination of a Raman pulses and resonant blow-away laser pulses. The interferometers take place at the center of the vertical tube shown in figure 1.2. A sequence of three vertical velocity–selective Raman pulses is used to realize the interferometer. The first ($\pi/2$ pulse) splits the atomic wave packet, the second (π pulse) induces the internal and external state inversion and the third ($\pi/2$ pulse) recombines the matter waves after their different space–time evolution. After the Raman interferometry sequence, the population of the ground state is measured in a chamber placed just above the MOT by selectively exciting the atoms and detecting the resulting fluorescence. Each atom interferometer in the gravity gradiometer measures the local acceleration with respect to the common reference frame identified by the wave fronts of the Raman lasers. Therefore, even if the phase noise induced by vibrations on the retro-reflecting mirror completely washes out the atom interference fringes, the signals simultaneously detected on the upper and lower accelerometers remain coupled and preserve a fixed phase relation. As a consequence, when the trace of the upper accelerometer is plotted as a function of the lower one, experimental points distribute along an ellipse. The differential phase shift $\Phi = \phi_u - \phi_l$, which is proportional to the gravity gradient, is then obtained from the eccentricity and the rotation angle of the ellipse best fitting the experimental data [36]. In order to modulate the actual value of the gravity gradient, source masses are vertically displaced in two different configurations. The induced phase shift is thus measured as a function of masses positions, realizing in this way a double-differential scheme, suitable to isolate the effect of source masses from others biases of acceleration difference between the two clouds (Earth's gravity gradient, Coriolis forces, etc.). From the accurate knowledge of the mass distribution, the value of G can be determined. In particular, it is directly linked to the differential angle $\Delta\Phi = \Phi_C - \Phi_F$.

1.3 Organization of the thesis

The work presented here has been carried out in the context of the MAGIA experiment. In the following, a description of the structure of this thesis is given.

In chapter 2, a brief general introduction to atom interferometry from a theoretical point of view is provided. In chapter 3 we will give a comprehensive overview of the overall experimental apparatus, including the latest source masses characterization measurements. Also a detailed de-

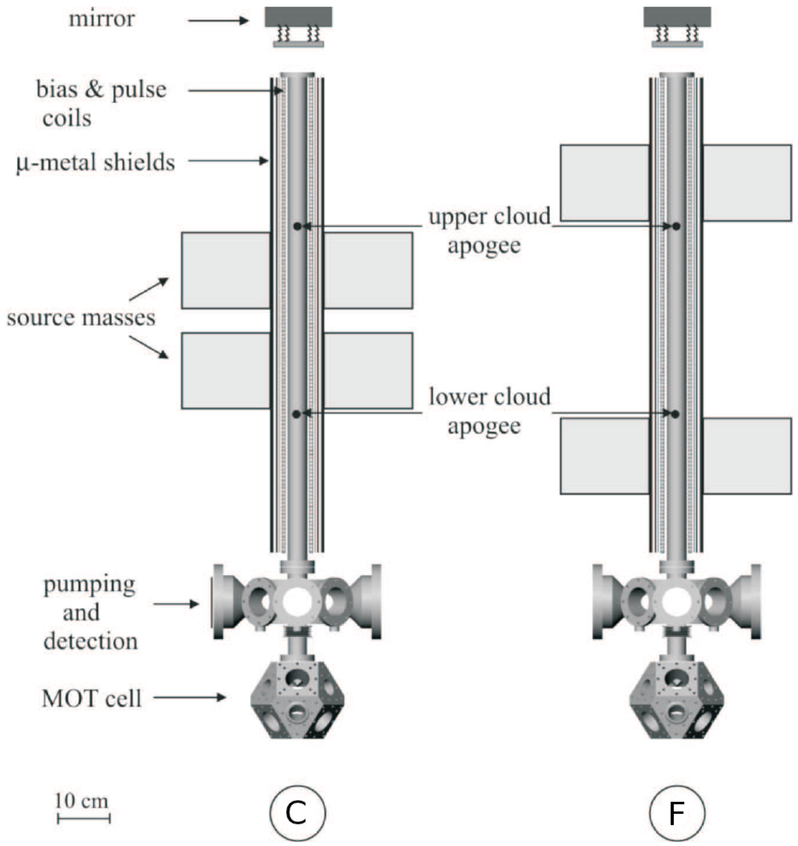

Figure 1.2: Scheme of the MAGIA experiment. ^{87}Rb atoms, trapped and cooled in a magneto-optical trap (MOT), are launched upwards in a vertical vacuum tube with a moving optical molasses scheme, producing an atomic fountain. Near the apogees of the atomic trajectories, a measurement of their vertical acceleration is performed by a Raman interferometry scheme. External source masses are positioned in two different configurations (C and F) and the induced phase shift is measured as a function of masses positions.

scription of the recent apparatus updates (2D-MOT and Raman lasers) is reported. Details about the experimental procedures adopted to prepare and manipulate ultracold Rb atoms can be found in chapter 4, together with a full discussion about signal analysis and experiment simulations. Finally, in chapter 5, all the experimental results obtained in the last four years (2009-2012) are collected and organized. In particular, the first section contains all the data regarding the gradiometer characterization, while we will spend the rest of the chapter to present the gravity measurements carried out, putting special emphasis on the latest G measurement.

Chapter 2

Cold atom interferometry

In order to realize an atom interferometer, coherent superposition of two quantum states of a single atom and wave packets recombination are required. Nowadays it is possible to realize them through laser radiation, whereby atoms can be cooled, trapped and manipulated . Specifically, light-induced transitions can be used to achieve the desired superposition by photons-to-atom momentum transfer. Afterwards atom internal states present different external degrees of freedom and consequently the interferometer will be sensitive to accelerating forces.

The two quantum states must have a lifetime longer than the experiment duration to avoid spontaneous emission. Ground-state hyperfine structures of alkali fit smoothly these requirements. Atom interferometer sensitivity depends essentially on two features: free evolution time and momentum transfer. In order to obtain large momentum transfer, stimulated Raman transitions have been chosen [37], using two counter propagating photons in the visible spectrum rather than a single one at microwave frequencies.

The present chapter will provide some tools for the calculation of the interferometric phase shift. The first part illustrates the derivation of the temporal evolution of a three-level atom in a light field, and we will use the results to evaluate the output of a three-pulses Raman interferometer. The second part explains how laser phase noise will affect the interferometer phase. In the present derivation, [38, 69] will be loosely followed. In this chapter Φ will indicate the phase shift between the atomic wave packets at the output of the interferometer and ϕ the Raman lasers phase difference.

2.1 Stimulated Raman transitions

To calculate the effect of stimulated Raman transitions, atoms described by a plane wave function with momentum $\mathbf{p}$ and position $\mathbf{r}$ are considered. The calculation will be limited to few states with defined momentum, first in the case of a three-level atom and later in the case of rubidium 87 (^{87}Rb).

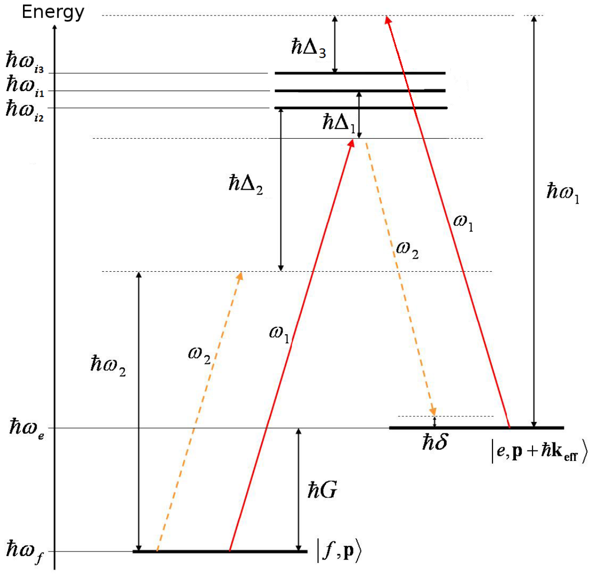

Figure 2.1: Three-level atom subjected to two electromagnetic fields

2.1.1 Three-level atom

Definition

We consider a three level (f, e and i) atom of mass M represented in figure 2.1, with rest energies $\hbar\omega_f^0$, $\hbar\omega_e^0$, $\hbar\omega_i^0$ in interaction with two electromagnetic fields (E_1 and E_2) of frequencies ω_1 and ω_2:

$$\begin{aligned}
\mathbf{E}_1(\mathbf{r},t) &= \hat{\epsilon}_1 E_1^0 e^{i(\omega_1 t - \mathbf{k}_1\mathbf{r} + \boldsymbol{\varphi_1^0(t)})} + c.c. \\
\mathbf{E}_2(\mathbf{r},t) &= \hat{\epsilon}_2 E_2^0 e^{i(\omega_2 t - \mathbf{k}_2\mathbf{r} + \boldsymbol{\varphi_2^0(t)})} + c.c. \qquad (2.1)
\end{aligned}$$

where $\hat{\epsilon}_1$and $\hat{\epsilon}_2$ denote beams polarizations, $\mathbf{k_1}$ and $\mathbf{k_2}$ are wave vectors,$\varphi_1^0(t)$ and $\varphi_2^0(t)$ indicate phases.

An atomic state can be described by its internal state and momentum. Now we suppose that the atoms are initially in the fundamental state $|f,\mathbf{p}\rangle$ with momentum $\mathbf{p}$. The total energy is:

$$\hbar\omega_f^0 + \frac{\mathbf{p}^2}{2M} = \hbar\omega_f \qquad (2.2)$$

The level$|f,\mathbf{p}\rangle$ is coupled to the excited level $|e,\mathbf{p}+\hbar\mathbf{k}_{\text{eff}}\rangle$ through the Raman transition, where $\mathbf{k}_{\text{eff}}$ is the effective wave vector given by $\mathbf{k}_{\text{eff}} = \mathbf{k}_1 - \mathbf{k}_2$. The level energy is equal to:

$$\hbar\omega_e^0 + \frac{(\mathbf{p}+\hbar\mathbf{k}_{eff})^2}{2M} = \hbar\omega_e \qquad (2.3)$$

In the present calculations we will use intermediate levels coupled to one of two fundamental levels through one of the two lasers fields.

These states are $|i, \mathbf{p} + \hbar\mathbf{k}_1\rangle$, $|i, \mathbf{p} + \hbar\mathbf{k}_2\rangle$, $|i, \mathbf{p} + \hbar(\mathbf{k}_1 + \mathbf{k}_{eff})\rangle$.

It is possible that others intermediate states can be coupled to the intermediate levels. Starting from $|i, \mathbf{p} + \hbar\mathbf{k}_2\rangle$ an atom can emit a photon with a wave vector $\mathbf{k}_2$ by stimulated emission towards the level $|e, \mathbf{p}\rangle$. It may be also that occurs a decay by stimulated emission of a photon with wave vector $\mathbf{k}_1$, toward one of two levels $|f, \mathbf{p} - \hbar\mathbf{k}_{eff}\rangle$, $|e, \mathbf{p} - \hbar\mathbf{k}_{eff}\rangle$. Likewise, from an intermediate level $|i, \mathbf{p} + \hbar(\mathbf{k}_1 + \mathbf{k}_{eff})\rangle$ an atom is coupled to the three levels $|f, \mathbf{p} + \hbar\mathbf{k}_{eff}\rangle$, $|f, \mathbf{p} - 2\hbar\mathbf{k}_{eff}\rangle$ and $|e, \mathbf{p} + 2\hbar\mathbf{k}_{eff}\rangle$.

These six levels can be neglected since:

- For these transitions, the detuning from the two-photon resonance condition is significantly higher than for the others and consequently the transition probabilities are much lower. The population in these levels will be negligible compared to that of the considered levels;
- They do not participate in the coupling between the two ground states.
- Two-photon light shift induced by these levels on the ground states is also negligible
- They do not induce spontaneous emission

The energies of the three intermediate levels, as shown in figure 2.1, are given by the following equations:

$$\begin{aligned}\hbar\omega_i^0 + \frac{(\mathbf{p} + \hbar\mathbf{k}_1)^2}{2M} &= \hbar\omega_{i1}\\ \hbar\omega_i^0 + \frac{(\mathbf{p} + \hbar\mathbf{k}_2)^2}{2M} &= \hbar\omega_{i2}\\ \hbar\omega_i^0 + \frac{(\mathbf{p} + \hbar(\mathbf{k}_1 + \mathbf{k}_{eff}))^2}{2M} &= \hbar\omega_{i3}\end{aligned} \tag{2.4}$$

We indicate with $\triangle_1$ the detuning between the laser E_1 and the transition$|f, \mathbf{p}\rangle \rightarrow |i, \mathbf{p} + \hbar\mathbf{k}_1\rangle$, with $\triangle_3$ the detuning between the same laser and the transition $|e, \mathbf{p} + \hbar\mathbf{k}_{eff}\rangle \rightarrow |i, \mathbf{p} + \hbar(\mathbf{k}_1 + \mathbf{k}_{eff})\rangle$ and with $\triangle_2$ the detuning between the laser E_2 and $|f, \mathbf{p}\rangle \rightarrow |i, \mathbf{p} + \hbar\mathbf{k}_2\rangle$ transition. Furthermore G will represent the frequency related to the transition $|f, \mathbf{p}\rangle \rightarrow |e, \mathbf{p} + \hbar\mathbf{k}_{eff}\rangle$ and finally δ denotes the detuning of G with respect to the frequency difference of the two Raman laser:

$$\begin{aligned}\triangle_1 &= \omega_1 - (\omega_{i1} - \omega_f)\\ \triangle_3 &= \omega_1 - (\omega_{i3} - \omega_e)\\ \triangle_2 &= \omega_2 - (\omega_{i2} - \omega_f)\\ G &= \omega_e - \omega_f\\ \delta &= (\omega_1 - \omega_2) - (\omega_e - \omega_f)\end{aligned} \tag{2.5}$$

To be effective the Raman transition must verify the two-photon resonance condition. Denoting by δ^{AC} the differential light shift of the two fundamental levels [16], the two-photon resonance condition is written as

$$(\omega_1 - \omega_2) = (\omega_e^0 - \omega_f^0) + (\omega_D + \omega_R) + \delta^{AC} \tag{2.6}$$

The frequencies ω_D e ω_R are respectively the Doppler shift and the shift due to recoil:

$$\omega_D = \frac{\mathbf{p}\mathbf{k}_{eff}}{M} \tag{2.7}$$

$$\omega_R = \frac{\hbar\left|\mathbf{k}_{eff}\right|^2}{2M} \tag{2.8}$$

Temporal evolution

In absence of external potentials the five levels previously introduced are eigenstates of the system. Therefore, neglecting the contribute of the others eigenstates, the wave function can be decomposed into the following five eigenfunctions with amplitude probabilities C_f, C_e, C_{i1}, C_{i2}, C_{i3}:

$$\begin{aligned} |\Psi(t)\rangle &= C_f\,|f,\mathbf{p}\rangle + C_e\,|e,\mathbf{p}+\hbar\mathbf{k}_{eff}\rangle + C_{i1}\,|i,\mathbf{p}+\hbar\mathbf{k}_1\rangle \\ &+ C_{i2}\,|i,\mathbf{p}+\hbar\mathbf{k}_2\rangle + C_{i3}\,|i,\mathbf{p}+\hbar(2\mathbf{k}_1-\mathbf{k}_2)\rangle \end{aligned} \tag{2.9}$$

In presence of laser radiation the Hamiltonian is no longer diagonal and is given by

$$\begin{aligned} H &= \hbar\omega_f\,|f,\mathbf{p}\rangle\,\langle f,\mathbf{p}| + \hbar\omega_e\,|e,\mathbf{p}+\hbar\mathbf{k}_{eff}\rangle\,\langle e,\mathbf{p}+\hbar\mathbf{k}_{eff}| \\ &+ \hbar\omega_{i1}\,|i,\mathbf{p}+\hbar\mathbf{k}_1\rangle\,\langle i,\mathbf{p}+\hbar\mathbf{k}_1| \\ &+ \hbar\omega_{i2}\,|i,\mathbf{p}+\hbar\mathbf{k}_2\rangle\,\langle i,\mathbf{p}+\hbar\mathbf{k}_2| \\ &+ \hbar\omega_{i3}\,|i,\mathbf{p}+\hbar(2\mathbf{k}_1-\mathbf{k}_2)\rangle\,\langle i,\mathbf{p}+\hbar(2\mathbf{k}_1-\mathbf{k}_2)| \\ &- \mathbf{D}(\mathbf{E}_1+\mathbf{E}_2) \end{aligned} \tag{2.10}$$

where $\mathbf{D}$ is the electric dipole operator associated with the transition to the intermediate state. In these calculations we will not take into account spontaneous emission from the intermediate levels because they are poorly populated during the Raman transition. This is reasonable since we operate at large detuning $\triangle_1 \gg \Gamma$, where Γ is the natural linewidth of the transition. If needed, calculations for the spontaneous emission can be done with a perturbative treatment.

To compute the time evolution of the wave function it is necessary to diagonalize the new Hamiltonian and to determine the system eigenstates. We can then derive the time evolution using the new base before returning to the initial one. After a preliminary change of variable $C_k = c_k e^{-i\omega_k t}$, Schrödinger's equation gives rise to the following system:

$$\begin{aligned}
\dot{c}_f &= -i\Omega^*_{f1} e^{-i(\omega_{i1}-\omega_f)t}\cos[\omega_1 t+\varphi^0_1(t)]c_{i1} \\
&\quad -i\Omega^*_{f2} e^{-i(\omega_{i2}-\omega_f)t}\cos[\omega_2 t+\varphi^0_2(t)]c_{i2} \\
\dot{c}_e &= -i\Omega^*_{e1} e^{-i(\omega_{i3}-\omega_e)t}\cos[\omega_1 t+\varphi^0_1(t)]c_{i3} \\
&\quad -i\Omega^*_{f2} e^{-i(\omega_{i1}-\omega_e)t}\cos[\omega_2 t+\varphi^0_2(t)]c_{i1} \\
\dot{c}_{i1} &= -i\Omega_{f1} e^{-i(\omega_f-\omega_{i1})t}\cos[\omega_1 t+\varphi^0_1(t)]c_f \\
&\quad -i\Omega^*_{e2} e^{-i(\omega_e-\omega_{i1})t}\cos[\omega_2 t+\varphi^0_2(t)]c_e \\
\dot{c}_{i2} &= -i\Omega_{f2} e^{-i(\omega_f-\omega_{i2})t}\cos[\omega_2 t+\varphi^0_2(t)]c_f \\
\dot{c}_{i3} &= -i\Omega_{e1} e^{-i(\omega_e-\omega_{i3})t}\cos[\omega_1 t+\varphi^0_1(t)]c_e
\end{aligned} \tag{2.11}$$

where Ω_{jk} is equal to:

$$\Omega_{jk} = -2\frac{\langle i|\,\mathbf{D}\hat{\epsilon}_{\mathbf{k}}\mathbf{E}^0_k\,|j\rangle}{\hbar} \tag{2.12}$$

then, applying the rotating wave approximation (RWA), we neglect the terms that oscillate at optical frequencies. Equations become:

$$\begin{aligned}
\dot{c}_f &= -i\frac{\Omega^*_{f1}}{2}e^{i(\triangle_1 t+\varphi^0_1(t))}c_{i1} - i\frac{\Omega^*_{f2}}{2}e^{i(\triangle_2 t+\varphi^0_2(t))}c_{i2} \\
\dot{c}_e &= -i\frac{\Omega^*_{e1}}{2}e^{i(\triangle_3 t+\varphi^0_1(t))}c_{i3} - i\frac{\Omega^*_{e2}}{2}e^{i((\triangle_1-\delta)t+\varphi^0_2(t))}c_{i1} \\
\dot{c}_{i1} &= -i\frac{\Omega_{f1}}{2}e^{i(\triangle_1 t+\varphi^0_1(t))}c_f - i\frac{\Omega_{e2}}{2}e^{-i((\triangle_1-\delta)t+\varphi^0_2(t))}c_e \\
\dot{c}_{i2} &= -i\frac{\Omega^*_{f2}}{2}e^{i(\triangle_2 t+\varphi^0_2(t))}c_f \\
\dot{c}_{i3} &= -i\frac{\Omega^*_{e1}}{2}e^{i(\triangle_3 t+\varphi^0_1(t))}c_e
\end{aligned} \tag{2.13}$$

Adiabatic elimination of the intermediate coefficients

At this stage is possible to reduce the number of unknown parameters using adiabatic elimination. We will verify that the coefficients of the levels $|i\rangle$ oscillate with frequency $\triangle_1$ while the coefficients c_e e c_f vary much more slowly, due to the fact that $\triangle_1$ is large compared to all the Rabi frequencies Ω_{jk}. Temporal evolution of c_i, if c_f and c_e are almost constant, is:

$$\begin{aligned}
c_{i1} &= \frac{\Omega_{f1}}{2\triangle_1}e^{-i(\triangle_1 t+\varphi^0_1(t))}c_f + \frac{\Omega_{e2}}{2(\triangle_1-\delta)}e^{-i((\triangle_1-\delta)t+\varphi^0_2(t))}c_e \\
c_{i2} &= \frac{\Omega_{f2}}{2\triangle_2}e^{-i(\triangle_2 t+\varphi^0_2(t))}c_f \\
c_{i3} &= \frac{\Omega_{e1}}{2\triangle_3}e^{-i(\triangle_3 t+\varphi^0_1(t))}c_e
\end{aligned} \tag{2.14}$$

Replacing these results in the first two equations of 2.13 yields:

$$\begin{aligned}
\dot{c}_f &= -i\left(\frac{|\Omega_{f1}|^2}{4\triangle_1}+\frac{|\Omega_{f2}|^2}{4\triangle_2}\right)c_f - i\left(\frac{\Omega^*_{f1}\Omega_{e2}}{4(\triangle_1-\delta)}e^{i(\delta t+\varphi^0_1-\varphi^0_2)}\right)c_e \\
\dot{c}_e &= -i\left(\frac{|\Omega_{e1}|^2}{4\triangle_3}+\frac{|\Omega_{e2}|^2}{4(\triangle_1-\delta)}\right)c_e - i\left(\frac{\Omega_{f1}\Omega^*_{e2}}{4\triangle_1}e^{-i(\delta t+\varphi^0_1-\varphi^0_2)}\right)c_f
\end{aligned} \tag{2.15}$$

Operating with a large detuning, the condition $\triangle_1 \gg \delta$ always holds. We will therefore approximate $(\triangle_1-\delta)\simeq\Delta_1$. For the same reason we have $\triangle_1 \gg \omega_D$ and $\triangle_1 \gg \omega_R$, so the following further approximations can be applied: $\triangle_3 \simeq (\triangle_1+G)$, $\triangle_2 \simeq (\triangle_1-G)$.

Then we define the effective Rabi frequency Ω_{eff}, the hyperfine levels light shift Ω^{AC}_f e Ω^{AC}_e and the phase difference ϕ^0 between the two laser:

$$\begin{aligned}
\Omega_{eff} &= \frac{\Omega_{f1}\Omega^*_{e2}}{2\Delta_1} \\
\Omega^{AC}_f &= \frac{|\Omega_{f1}|^2}{4\triangle_1}+\frac{|\Omega_{f2}|^2}{4(\triangle_1-G)} \\
\Omega^{AC}_e &= \frac{|\Omega_{e1}|^2}{4(\triangle_1+G)}+\frac{|\Omega_{e2}|^2}{4\triangle_1} \\
\phi^0 &= \varphi^0_1(t)-\varphi^0_2(t)
\end{aligned} \tag{2.16}$$

This allows us to rewrite the equation 2.15 in the following form:

$$\begin{aligned}
\dot{c}_f = -i\left(\Omega^{AC}_f c_f + \tfrac{\Omega^*_{eff}}{2}e^{i(\delta t+\phi^0)}c_e\right) \\
\dot{c}_e = -i\left(\Omega^{AC}_e c_e + \tfrac{\Omega_{eff}}{2}e^{-i(\delta t+\phi^0)}c_f\right)
\end{aligned} \tag{2.17}$$

It is also possible to define the differential light shift δ^{AC}, the total light shift AC and generalized Rabi frequency Ω_R:

$$\begin{aligned}
\delta^{AC} &= \Omega^{AC}_e - \Omega^{AC}_f \\
AC &= (\Omega^{AC}_e + \Omega^{AC}_f) \\
\Omega_R &= \sqrt{\Omega^2_{eff}+(\delta-\delta^{AC})^2}
\end{aligned} \tag{2.18}$$

Applying the change of variable $c_f = a_f e^{-i\left(\frac{AC-\delta}{2}\right)t}$ e $c_e = a_e e^{-i\left(\frac{AC+\delta}{2}\right)t}$, the following equation system with variable coefficients is obtained:

$$\begin{cases}
\dot{a}_f &= -\frac{i}{2}\left((\delta-\delta^{AC})a_f + \Omega^*_{eff}e^{i\phi^0}a_e\right) \\
\dot{a}_e &= -\frac{i}{2}\left(\Omega_{eff}e^{-i\phi^0}a_f - (\delta-\delta^{AC})a_e\right)
\end{cases} \tag{2.19}$$

This system is well known and its solution can be found in [39]. Temporal evolution of a_f and a_e coefficients is

$$\begin{aligned}
a_f(t_0+\tau) &= \left(\cos\left(\frac{\Omega_R\tau}{2}\right) - i\frac{\delta-\delta^{AC}}{\Omega_R}\sin\left(\frac{\Omega_R\tau}{2}\right)\right)a_f(t_0) \\
&\quad -ie^{i\phi^0}\frac{|\Omega_{eff}|}{\Omega_R}\sin\left(\frac{\Omega_R\tau}{2}\right)a_e(t_0) \\
a_e(t_0+\tau) &= -ie^{-i\phi^0}\frac{|\Omega_{eff}|}{\Omega_R}\sin\left(\frac{\Omega_R\tau}{2}\right)a_f(t_0) \\
&\quad +\left(\cos\left(\frac{\Omega_R\tau}{2}\right) + i\frac{\delta-\delta^{AC}}{\Omega_R}\sin\left(\frac{\Omega_R\tau}{2}\right)\right)a_e(t_0)
\end{aligned} \tag{2.20}$$

Introducing the notation $\cos\theta = \frac{\delta-\delta^{AC}}{\Omega_R}$ and $\sin\theta = \frac{|\Omega_{eff}|}{\Omega_R}$ and performing a change of variable in order to get the coefficients c_f e c_e, we have:

$$\begin{aligned}
c_f(t_0+\tau) &= \left(\cos\left(\frac{\Omega_R\tau}{2}\right) - i\cos\theta\sin\left(\frac{\Omega_R\tau}{2}\right)\right)e^{-i(AC-\delta)\frac{\tau}{2}}c_f(t_0) \\
&\quad -ie^{i(\delta t_0+\phi^0)}\sin\theta\sin\left(\frac{\Omega_R\tau}{2}\right)e^{-i(AC-\delta)\frac{\tau}{2}}c_e(t_0) \\
c_e(t_0+\tau) &= -ie^{-i(\delta t_0+\phi^0)}\sin\theta\sin\left(\frac{\Omega_R\tau}{2}\right)e^{-i(AC+\delta)\frac{\tau}{2}}c_f(t_0) \\
&\quad +\left(\cos\left(\frac{\Omega_R\tau}{2}\right) - i\cos\theta\sin\left(\frac{\Omega_R\tau}{2}\right)\right)e^{-i(AC+\delta)\frac{\tau}{2}}c_e(t_0)
\end{aligned} \tag{2.21}$$

It should be noted that the coefficients c_f e c_e oscillate at Ω_R frequency, in agreement with the hypothesis of adiabatic elimination

$$\triangle_1 \gg \Omega_R = \frac{\Omega_{f1}\Omega^*_{e2}}{2\Delta_1} \tag{2.22}$$

Finally, with a last change of variables, we go back to the $|f,\mathbf{p}\rangle$ base. Bearing in mind the identity $\delta+\omega_e-\omega_f=\omega_1-\omega_2$, the system evolution equations are the following:

System evolution:

$$\begin{aligned}
C_f(t_0+\tau) &= \left(\cos\left(\frac{\Omega_R\tau}{2}\right) - i\cos\theta\sin\left(\frac{\Omega_R\tau}{2}\right)\right)e^{-i(AC-\delta+2\omega_f)\frac{\tau}{2}}C_f(t_0) \\
&\quad -ie^{i((\omega_1-\omega_2)t_0+\phi^0)}\sin\theta\sin\left(\frac{\Omega_R\tau}{2}\right)e^{-i(AC-\delta+2\omega_f)\frac{\tau}{2}}C_e(t_0) \\
C_e(t_0+\tau) &= -ie^{i((\omega_1-\omega_2)t_0+\phi^0)}\sin\theta\sin\left(\frac{\Omega_R\tau}{2}\right)e^{-i(AC-\delta+2\omega_e)\frac{\tau}{2}}C_f(t_0) \\
&\quad +\left(\cos\left(\frac{\Omega_R\tau}{2}\right) - i\cos\theta\sin\left(\frac{\Omega_R\tau}{2}\right)\right)e^{-i(AC-\delta+2\omega_e)\frac{\tau}{2}}C_e(t_0)
\end{aligned} \tag{2.23}$$

Transition	Phase shift for $\Omega_{eff}\tau = \frac{\pi}{2}$	Phase shift for $\Omega_{eff}\tau = \pi$
$\lvert f\rangle \rightarrow \lvert f\rangle$	$-\theta^0 + (-AC + \delta - 2\omega_f)\frac{\tau}{2}$	-
$\lvert e\rangle \rightarrow \lvert f\rangle$	$(\omega_1 - \omega_2)t_0 + \phi^0$ $-\frac{\pi}{2} + (-AC + \delta - 2\omega_f)\frac{\tau}{2}$	$(\omega_1 - \omega_2)t_0 + \phi^0$ $-\frac{\pi}{2} + (-AC + \delta - 2\omega_f)\frac{\tau}{2}$
$\lvert f\rangle \rightarrow \lvert e\rangle$	$-(\omega_1 - \omega_2)t_0 - \phi^0$ $-\frac{\pi}{2} + (-AC - \delta - 2\omega_e)\frac{\tau}{2}$	$-(\omega_1 - \omega_2)t_0 - \phi^0$ $-\frac{\pi}{2} + (-AC - \delta - 2\omega_e)\frac{\tau}{2}$
$\lvert e\rangle \rightarrow \lvert e\rangle$	$\theta^0 + (-AC - \delta - 2\omega_e)\frac{\tau}{2}$	-

Table 2.1: Phase shift acquired under Raman pulses

Special cases: $\frac{\pi}{2}$ pulse and π pulse

It is interesting to treat the special case where the resonance condition has occurred and the total and differential light shifts are neglected. The initial state is chosen such that $C_f(t_0)$=1 and $C_e(t_0)$=0. The equation 2.23 can be simplified to give:

$$
\begin{aligned}
C_f(t_0 + \tau) &= \cos\left(\frac{|\Omega_{eff}|\,\tau}{2}\right) e^{-i\omega_f\tau} \\
C_e(t_0 + \tau) &= -ie^{-i((\omega_1 - \omega_2)t_0 + \phi^0)} \sin\left(\frac{|\Omega_{eff}|\,\tau}{2}\right) e^{-i\omega_e\tau}
\end{aligned}
\tag{2.24}
$$

When the pulse duration is such that $|\Omega_{eff}|\,\tau = \frac{\pi}{2}$, a coherent equiprobable superposition between the two hyperfine levels is achieved. When the pulse duration satisfies, instead, $|\Omega_{eff}|\,\tau = \pi$, the wave function is transferred from $|f\rangle$ to $|e\rangle$ and vice versa.

These are the two types of pulses that allow us to create the interferometer sequence. The wave function acquires a phase equal to the phase difference of the Raman laser. More accurate evaluation of the acquired phase shift can be performed from equation 2.23. Results are presented in table 2.1. The term θ^0 stands for the phase of $\cos\left(\frac{|\Omega_{eff}|\tau}{2}\right) - i\cos\theta\sin\left(\frac{|\Omega_{eff}|\tau}{2}\right)$. Finally it is worth pointing out that noninteracting atoms does do not interfere at the end of the interferometer.

2.1.2 ^{87}Rb atom and laser sources configuration

The rubidium atom (^{87}Rb) employed in the experiment has not a simple three-level energy structure. The figure 2.1.2 shows the energy levels of ^{87}Rb related to the D_2 transition (see Appendix A for more information), together with the frequencies of the laser used for the Raman transition. As levels $|f\rangle$ and $|e\rangle$ we are going to use the two ground-state hyperfine levels with Zeeman sub-level $m_F = 0$: $\left|5S_{1/2},\, F = 1,\, m_F = 0\right\rangle$ $\left|5S_{1/2},\, F = 2,\, m_F = 0\right\rangle$. The lasers are nearly tuned at the transition frequency to the level$\left|5P_{3/2}\right\rangle$. Due to the selection rules for electric dipole and considering the two-photons transition case, only the two hyperfine levels $\left|5P_{3/2},\, F^{'} = 1\right\rangle$ and $\left|5P_{3/2},\, F^{'} = 2\right\rangle$ are involved in the Raman transition. Moreover the coupling with each of the four levels $\left|5P_{3/2},\, F^{'} = 0 \rightarrow 3\right\rangle$ can a priori induce a shift light.

According with the figure 2.3, in which the polarization and the spatial configuration adopted by each of the laser beams is shown, the Raman lasers enter from below with equal linear polarization

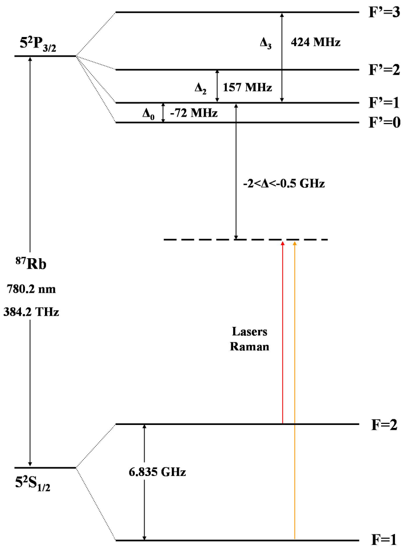

Figure 2.2: ^{87}Rb D_2 transition electronic energy structure. Energy levels are not in scale.

and exit from above. After passing through a quarter wave plate they are retro reflected by a mirror, thus obtaining a lin⊥lin configuration in the interferometer region. Theoretically, both pairs of counter-propagating beams can make the two-photon transition. However, an initial speed of the wave packet higher than the atomic recoil velocity is sufficient to select only one pair by Doppler effect. Now we proceed to the calculation of Ω_{eff}, Ω_f^{AC} and Ω_e^{AC} bearing in mind the Rb electronic structure. For this purpose is convenient to define as $\triangle$ the detuning from the level $\left|5P_{3/2}, F^{'}=1\right\rangle$ and similarly with Δ_0, Δ_2 and Δ_3 the frequency differences among $|F=1\rangle$ and $\left|F^{'}=0\right\rangle$, $\left|F^{'}=2\right\rangle$, $\left|F^{'}=3\right\rangle$.

We rewrite 2.16 determining a new effective Rabi frequency and light shifts:

$$\begin{aligned}
\Omega_{eff} &= \sum_k \frac{\Omega^*_{k,f1}\Omega_{k,e2}}{2(\Delta+\triangle_k)} \\
\Omega_f^{AC} &= \sum_k \frac{\left|\Omega_{k,f1}\right|^2}{4(\Delta+\triangle_k)} + \frac{\left|\Omega_{k,f2}\right|^2}{4(\triangle+\triangle_k-G)} \qquad (2.25) \\
\Omega_e^{AC} &= \sum_k \frac{\left|\Omega_{k,e1}\right|^2}{4(\Delta+\triangle_k+G)} + \frac{\left|\Omega_{k,e2}\right|^2}{4(\triangle+\triangle_k)}
\end{aligned}$$

where $\Omega_{kmn} = -\frac{\left\langle i,F^{'}=k\left|\mathbf{D}\hat{\epsilon}_\mathbf{n}\mathbf{E}_n^0\right|m\right\rangle}{\hbar}$ represents the Rabi frequency related to the laser E_n that couples the ground level $|m\rangle$ and the intermediate level $\left|i,F^{'}=k\right\rangle$. Taking into account the polarization of the beams and Clebsch-Gordan coefficients given in Appendix A, we obtain:

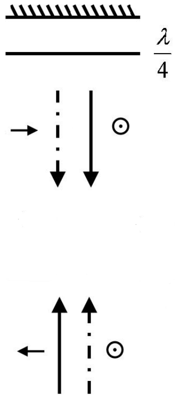

Figure 2.3: Raman beams configuration. Solid and dashed lines indicate the propagation direction. Beam polarizations are also shown.

$$\Omega_{eff} = \frac{\Omega_1\Omega_2}{2}\left(\frac{1}{24\triangle}+\frac{1}{8(\triangle-\triangle_2)}\right) \tag{2.26}$$

$$\Omega_f^{AC} = \frac{\Omega_1}{4}\left(\frac{5}{24\Delta}+\frac{1}{8(\triangle-\triangle_2)}\right)+\frac{\Omega_2^2}{4}\left(\frac{5}{24(\triangle-G)}+\frac{1}{8(\triangle-\triangle_2-G)}\right) \tag{2.27}$$

$$\begin{aligned}\Omega_e^{AC} = {} & \frac{\Omega_1^2}{4}\left(\frac{1}{120(\triangle+G)}+\frac{1}{8(\triangle-\triangle_2+G)}+\frac{1}{5(\triangle-\triangle_3+G)}\right) \\ & +\frac{\Omega_2^2}{4}\left(\frac{1}{120\triangle}+\frac{1}{8(\triangle-\triangle_2)}+\frac{1}{5(\triangle-\triangle_3)}\right)\end{aligned} \tag{2.28}$$

where $\Omega_1$and $\Omega_2$are the single beam Rabi frequencies:

$$\begin{aligned}\Omega_1 &= \frac{2DE_1^0}{\hbar} \\ \Omega_2 &= \frac{2DE_2^0}{\hbar}\end{aligned} \tag{2.29}$$

2.1.3 Light shift

Total shift

Table 2.1 shows how the light shift is involved in the phase shift imprinted by Raman pulses during the various interferometer stages. The total light shift AC adds an identical phase shift on the two

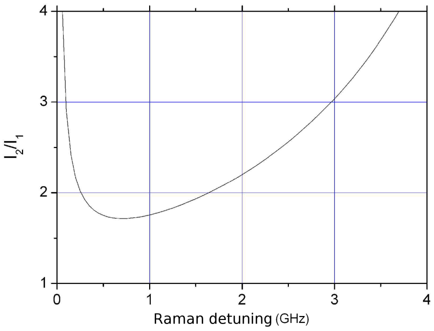

Figure 2.4: Value of the intensity ratio that cancels the differential light shift as a function of the detuning

arms of the interferometer in the presence of a $\frac{\pi}{2}$ pulse since the two wave packets are overlapped. Instead, under a π pulse, the wave packets have a vertical separation of approximately a few tenths of millimeter. In the ideal case in which the beams pass through perfect optics, it is expected that the intensities of the lasers are not amplitude modulated and therefore identical in both positions. Since the optics are not ideal, it is reasonable to expect amplitude modulation of the beams. As a results the atoms are affected by a different light shift and thus an extra phase shift will come out at the interferometer output.

Differential shift

The differential phase shift δ^{AC} occurs through the phase θ^0 when $\frac{\pi}{2}$ pulses take place. Such phase is not the same for both $\frac{\pi}{2}$ pulses, which translates into a additional phase shift (θ_1^0-θ_3^0), where θ_k^0 is the phase shift caused by k-th pulse. From equations 2.27 e 2.28 we can evaluate a intensity ratio $\frac{I_2}{I_1} = \frac{\Omega_2^2}{\Omega_1^2}$ such that $\Omega_f^{AC} = \Omega_e^{AC}$ so that the differential light shift is canceled. The intensity ratio expression is:

$$\frac{I_2}{I_1} = \frac{\left(\frac{1}{60(\triangle+G)} + \frac{1}{4(\triangle-\triangle_2+G)} + \frac{2}{5(\triangle-\triangle_3+G)}\right) - \left(\frac{5}{12\triangle} + \frac{1}{4(\triangle-\triangle_2)}\right)}{\left(\frac{5}{12(\triangle-G)} + \frac{1}{4(\triangle-\triangle_2-G)}\right) - \left(\frac{1}{60\triangle} + \frac{1}{4(\triangle-\triangle_2)} + \frac{2}{5(\triangle-\triangle_3)}\right)} \tag{2.30}$$

In figure 2.4 the zero-light-shift intensity ratio is plotted as a function of the detuning $\triangle$. In further calculations will be assumed to stay always in zero differential light shift condition. $R(\triangle)$ will indicate the particular intensity ratio value at which this condition holds.

2.2 Atom Interferometer

The interferometer is constituted by a sequence of three Raman pulses $\frac{\pi}{2}$-π-$\frac{\pi}{2}$, separated by a free evolution time T (figure 2.5). The three pulses have the same laser power, but time durations that are respectively τ-2τ-τ.

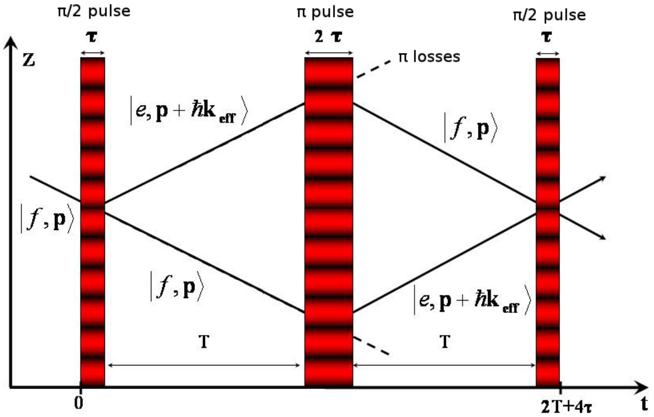

Figure 2.5: Schematic illustration of a vertical, symmetrical light pulse interferometer.

The first pulse puts the atom wave function in a coherent superposition of the two hyperfine states, transferring the two photons momentum. During the first time evolution interval T, the two arms of the interferometer split up. The second pulse acts on each of the two arms of the interferometer and exchange hyperfine levels of the two wave packets as well as their speed. Atoms that do not perform the π, transition, called "π losses" in figure 2.5, do not interfere because the separation between wave packets will be large compared to their spatial extension. After the πpulse the two wave packets approach and overlap after a second time interval T. Finally, the last pulse $\frac{\pi}{2}$ recombines the two arms of the interferometer.

2.2.1 Atomic interferometer modeling

Using previous results about Raman transitions, it is possible to model the atomic interferometer to compute the sensitivity to accelerations and to various experimental sources of noise, such as laser phase, vibrations, quantum projection.

Transfer matrix

To model the interferometer, it is convenient to rewrite the equations 2.23 in matrix form

$$\begin{pmatrix} C_f(t_0+\tau) \\ C_e(t_0+\tau) \end{pmatrix} = M(t_0, \phi, \Omega_{eff}, \tau) \begin{pmatrix} C_f(t_0) \\ C_e(t_0) \end{pmatrix} \tag{2.31}$$

where $M(t_0, \phi, \Omega_{eff}, \tau)$ is the transfer matrix of a single Raman pulse. Let us suppose to be in the ideal case in which the differential light shift is canceled thanks to the appropriate intensity ratio, the total light shift AC provides no phase shift and the resonance condition is verified. The transfer matrix is then

$$M(t_0,\phi,\Omega_{eff},\tau)= \tag{2.32}$$
$$\begin{pmatrix} \cos\left(\frac{|\Omega_{eff}|\tau}{2}\right)e^{-i\omega_f\tau} & -ie^{i((\omega_1-\omega_2)t_0+\phi)}\sin\left(\frac{|\Omega_{eff}|\tau}{2}\right)e^{-i\omega_f\tau} \\ -ie^{-i((\omega_1-\omega_2)t_0+\phi)}\sin\left(\frac{|\Omega_{eff}|\tau}{2}\right)e^{-i\omega_e\tau} & \cos\left(\frac{|\Omega_{eff}|\tau}{2}\right)e^{-i\omega_e\tau} \end{pmatrix}$$

The transfer matrix corresponding to the free time evolution is derived from the previous matrix setting Ω_{eff} to zero. The matrix simplifies to give:

$$M(T)=\begin{pmatrix} e^{-i\omega_f T} & 0 \\ 0 & e^{-i\omega_e T} \end{pmatrix} \tag{2.33}$$

According to this formalism, the system after the full interferometer sequence is described by the product of five transfer matrices corresponding to different pulses and time intervals T. Neglecting the phase change during each pulse, we define the Raman phases related to the three pulses as ϕ_1, ϕ_2, ϕ_3. The origin of the time coordinates has been chosen in the middle of the π pulse. The transfer matrix of the interferometer is written as:

$$M_{interf}=M(T+\tau,\phi_3,\Omega_{eff},\tau)M(T)M(-\tau,\phi_2,\Omega_{eff},2\tau)M(T)M(-T-2\tau,\phi_1,\Omega_{eff},\tau) \tag{2.34}$$

Since the initial state is $|f\rangle$ ($C_f(-T-2\tau)=1$ and $C_e(-T-2\tau)=0$), we proceed to the calculation of the interferometer output with the aid of the formalism just described. The resulting transition probability is:

$$P=|C_e(T+2\tau)|^2=\frac{1-\cos(\phi_1-2\phi_2+\phi_3)}{2} \tag{2.35}$$

The interferometric phase Φ, i.e. the phase difference between the two arms of the interferometer, is then given by $\Phi=\phi_1-2\phi_2+\phi_3$. Taking into account the phase θ^0 (table 2.1) at the time of the first and last pulse, respectively θ_1^0 and θ_3^0, the interferometric phase becomes:

$$\Phi=\phi_1-2\phi_2+\phi_3+\theta_1^0-\theta_3^0 \tag{2.36}$$

This result shows that the interferometer is sensitive to phase noise over the three Raman pulses and to all the effects that modify the transition frequency between the first and third pulse.

2.2.2 Sensitivity function

Calculation

In this section the goal is to calculate the evolution of the phase in the presence of the laser pulses. We will use a formalism developed for atomic clocks for calculating the influence of the local oscillator noise [73]. Basically we are going to evaluate the response of the interferometer to an infinitesimal phase variation $\delta\phi$ as a function of the time t at which such variation occurs. This formalism also allows us to calculate the gravity acceleration sensitivity, taking into account the finite duration of the Raman pulses.

If the phase difference among the Raman laser undergoes a phase jump $\delta\phi$ at time t, this will result in a variation δP of the measured transition probability P. The sensitivity function is defined as the limit of $\delta\phi$ going to zero of the δP and $\delta\phi$ ratio:

$$g_s(t) = 2 \lim_{\delta\phi \to 0} \frac{\delta P(\delta\phi,\, t)}{\delta\phi} \tag{2.37}$$

The interferometric phase shift Φ is established through the measurement of transition probability. Thus it is convenient to be in a situation where the interferometric phase is $\frac{\pi}{2}$ on total. Now we can develop in series the equation 2.35, taking the first order:

$$P(\delta\phi,\, t) = \frac{1 \pm \delta\Phi(\delta\phi,\, t)}{2} \tag{2.38}$$

The interferometric phase is directly calculated from the sensitivity function through the expression:

$$g_s(t) = \underset{\delta\phi \to 0}{lim} \frac{\delta\Phi(\delta\phi,\, t)}{\delta\phi} \tag{2.39}$$

where the phase jump $\delta\phi$ takes place during the free evolution time. In the case of a phase jump between the second and the third pulse will use the equation 2.35 with $\phi_1 = \phi + \pi/2$, $\phi_2 = \phi$ and $\phi_3 = \phi + \delta\phi$. The resulting value of the sensitivity function is $+1$. Similarly, the sensitivity function is -1 when the phase jump is performed between the first and the second pulse. Finally, when the phase shift takes place outside the interferometer sensitivity function is zero.

To evaluate the sensitivity when the phase change occurs within a pulse, the corresponding transfer matrix (equation 2.34) is split into two matrix product. The first matrix describes the evolution of the system until the time t using the phase value ϕ and the second one describes the evolution until the pulse end using the phase value $\phi + \delta\phi$. For example, when the phase shift occurs within the first pulse, the transfer matrix becomes

$$M_{t,\delta\phi}(-T-2\tau,\, \phi,\, \Omega_{eff}, \tau) = M(t,\, \phi+\delta\phi,\, \Omega_{eff,}\, -T-\tau-t) M(-T-2\tau,\, \phi,\, \Omega_{eff},\, t+T+2\tau) \tag{2.40}$$

Setting$|\Omega_R|\,\tau = \pi/2$, the sensitivity function during each of the three pulses is depicted in figure 2.6 and its analytical expression is:

$$g_s(t) = \begin{cases} \sin(\Omega_R(t+T)) & -T-2\tau < t < -T-\tau \\ -1 & -T-\tau < t < -\tau \\ \sin(\Omega_R t) & -\tau < t < \tau \\ 1 & \tau < t < T+\tau \\ \sin(\Omega_R(t-T)) & T+\tau < t < T+2\tau \end{cases} \tag{2.41}$$

Interferometric phase shift calculation

The interferometric phase shift can be calculated for any evolution of the Raman phase $\phi(t)$ with the aid of the sensitivity function:

$$\delta\Phi = \int_{-\infty}^{+\infty} g_s(t) d\phi(t) = \int_{-\infty}^{+\infty} g_s(t) \frac{d\phi(t)}{dt} dt \tag{2.42}$$

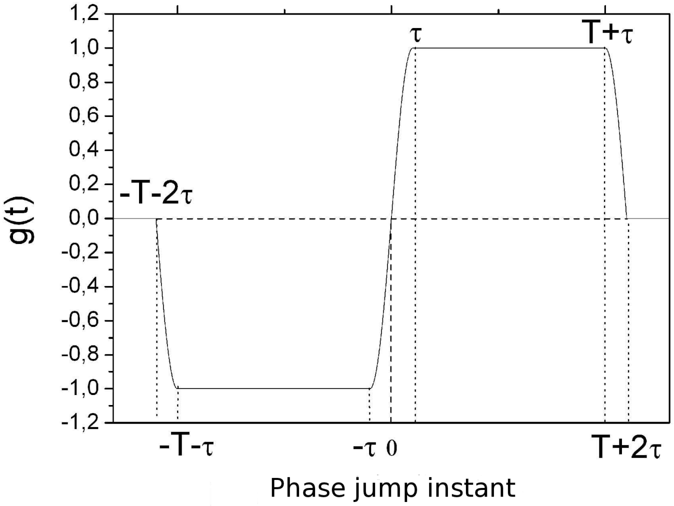

Figure 2.6: Sensitivity function $g_s(t)$ as a function of the phase jump instant [38, 69].

In presence of gravity atoms are accelerated. To stay in the context of previous calculations, we consider a reference system in which free falling atoms have an initial velocity v_0. Atoms undergo a instantaneous phase difference equal to:

$$\phi(t) = \frac{k_{\text{eff}} g t^2}{2} + k_{\text{eff}} v_0 t + \phi^0(t) \tag{2.43}$$

The optical Raman phase $\phi^0(t)$ is externally controlled and a noise study will be presented later. Due to the symmetry of the function $g_s(t)$, the initial velocity v_0 does not induce any phase shift. The calculation of the interferometric phase finally shows an expression compatible with [40] equal to:

$$\delta\Phi = \int_{-\infty}^{+\infty} g_s(t) k_{\text{eff}} g t dt \tag{2.44}$$

$$\delta\Phi = k_{\text{eff}} g (T + 2\tau)(T + \frac{4\tau}{\pi}) \tag{2.45}$$

In performing the calculations we assumed that the resonance condition is verified for all three pulses. Due to the Doppler effect this assumption is not true for typical values of T used. In order to preserve the resonance condition, we add a linear frequency ramp α on one of the two Raman lasers. Consequently, the equation 2.45 becomes:

$$\boxed{\delta\Phi = (k_{eff} g - \alpha)(T + 2\tau)(T + \frac{4\tau}{\pi}) \qquad (2.46)}$$

This expression finally allows to measure the value of the acceleration of gravity g by determining the value of α_0 for which the frequency ramp cancels the gravity induced phase shift.

2.2.3 Sensitivity to phase noise

Transfer function

The effect of the laser phase noise on the interferometric measurement can be also evaluated. In this case we do not know a priori the temporal evolution of the phase. On the other hand, it is possible to measure the phase noise spectrum in Fourier space. It is convenient to perform an analysis for a sinusoidal-like phase noise of frequency ω and phase ψ in order to obtain the transfer function $H(\omega)$. Then we will use it to calculate the standard deviation of the interferometric noise knowing the noise spectrum.

Consider a phase noise of the form $\phi(t) = A_0\cos(\omega_0 t+\psi)$. The derivative is $\frac{d\phi(t)}{dt} = -A_0\omega_0\sin(\omega_0 t+\psi)$ and the interferometric phase shift is

$$\delta\Phi = \int_{-\infty}^{+\infty} -g_s(t)A_0\omega_0\sin(\omega_0 t+\psi)dt \tag{2.47}$$

The Fourier transform of $g_s(t)$ in given by

$$G(\omega) = \int_{-\infty}^{+\infty} e^{-i\omega t}g_s(t)dt \tag{2.48}$$

if the replacement of $e^{-i\omega t}$ with $\cos(\omega t) - i\sin(\omega t)$ is performed, since the function $g_s(t)$ is odd, the integral of $\cos(\omega t)$ is zero. Therefore, the Fourier transform of $g_s(t)$ is written as:

$$G(\omega) = \int_{-\infty}^{+\infty} -i\sin(\omega t)g_s(t)dt \tag{2.49}$$

In a similar way, to calculate the interferometric phase the term $\sin(\omega_0 t+\psi)$ it is expanded in $\sin(\omega_0 t)\cos(\psi) + \cos(\omega_0 t)\sin(\psi)$. The integral of $\cos(\omega_0 t)\sin(\psi)$ is null and we find the expression:

$$\delta\Phi = A_0\omega_0\int_{-\infty}^{+\infty} -g_s(t)\sin(\omega_0 t)\cos(\psi)dt \tag{2.50}$$

and finally:

$$\delta\Phi = -iA_0\omega_0 G(\omega_0)\cos(\psi) = -A_0\omega_0\cos(\psi)\left|G(\omega_0)\right| \tag{2.51}$$

Taking repeated measures supposing a random uniformly distributed phase ψ, the standard deviation of the interferometric phase fluctuations is $\sigma_\Phi = A_0\omega_0\left|G(\omega_0)\right|/\sqrt{2}$. In presence of a phase noise spectral density $S_\Phi(\omega)$ the variance of the interferometric phase fluctuations becomes

$$\sigma_\Phi^2 = \int_0^{+\infty}\left|\omega G(\omega_0)\right|^2 S_\phi(\omega)\frac{d\omega}{2\pi} \tag{2.52}$$

Is now also possible to define the transfer function of the interferometer as $H(\omega) = |\omega G(\omega)|$. The Fourier transform of the sensitivity function $g_s(t)$ (see equation 2.6) is:

$$G(\omega) = \frac{4i\Omega_R}{\omega^2-\Omega_R^2}\sin\left(\frac{\omega(T+2\tau)}{2}\right)\left(\cos\left(\frac{\omega(T+2\tau)}{2}\right)+\frac{\Omega_R}{\omega}\sin\left(\frac{\omega T}{2}\right)\right) \tag{2.53}$$

Thus the transfer function of the interferometer has the following expression:

$$H(\omega) = \frac{4\omega\Omega_R}{\omega^2 - \Omega_R^2} \sin\left(\frac{\omega(T+2\tau)}{2}\right)\left(\cos\left(\frac{\omega(T+2\tau)}{2}\right) + \frac{\Omega_R}{\omega}\sin\left(\frac{\omega T}{2}\right)\right) \tag{2.54}$$

$H(\omega)$ presents several remarkable features (see figures 2.7 and 2.8):

- It vanishes periodically when ω is a multiple of $\frac{2\pi}{T+2\tau}$. This corresponds to frequencies such that an integer number of oscillations takes place between each couple of Raman pulse through the factor $\sin\left(\frac{\omega(T+2\tau)}{2}\right)$.
- At high frequencies we can replace the square of the transfer function with its mean value given by:

$$\overline{H(\omega)^2} = \frac{4\Omega_R^4}{(\Omega_R^2 - \omega^2)^2}\left(\frac{3}{2} + \frac{3\omega^2}{4\Omega_R^2} - \left(\sin\frac{\pi\omega}{2\Omega_R} + \frac{\omega}{2\Omega_R}\right)^2\right) \tag{2.55}$$

- When the frequencies considered are large compared to the Rabi frequency, the phase fluctuations takes an average value over the pulse duration. The transfer function behaves as a first order low pass filter and scales as $\frac{\sqrt{2}\Omega_R}{\omega}$ for $\omega \gg \Omega_R$. This effect is due to the factor $\frac{4\omega\Omega_R}{\omega^2-\Omega_R^2}$. The cutoff frequency is about $\frac{\Omega_R}{\pi}$.
- On the other hand, $H(\omega)$ shows a high pass filter behavior below $f = 1/(\pi T)$, determined only by the duration of the interferometer sequence.
- Finally the last factor, $\cos\left(\frac{\omega(T+2\tau)}{2}\right) + \frac{\Omega_R}{\omega}\sin\left(\frac{\omega T}{2}\right)$, introduces a second set of zeros which depend on the value of Ω_R. Is difficult to deduce intuitively this latter feature and it was verified by measuring the transfer function with an atomic gyroscope [41].

Thanks to this formalism now we are able to evaluate the effect of any phase-frequency perturbations. In particular, we are going to develop the calculations for the Raman phase noise and for seismic vibrations.

Phase noise sensitivity

We want to estimate the sensitivity achievable with a gravimeter respect to a given phase noise spectral density. The standard deviation on a single measure is not a suitable tool to determine the sensitivity of the gravimeter [42]. For this purpose it is more convenient to introduce the Allan variance of the interferometric phase fluctuations. We define the repetition time T_c of a single measurement and τ_m the total integration time, multiple of T_c ($\tau_m = mT_c$). Thus the Allan variance is defined as follow:

$$\sigma_\Phi^2(\tau_m) = \frac{1}{2}\lim_{n\to\infty}\left\{\frac{1}{n}\sum_{k=1}^{n}(\overline{\delta\Phi}_{k+1} - \overline{\delta\Phi}_k)^2\right\} \tag{2.56}$$

where $\overline{\delta\Phi}_k$ is the total of the measured phase shifts in the time interval $[t_k, t_{k+1}]$= $[-T_c/2+kmT_c$, $-T_c/2+(k+1)mT_c]$. Computing the total value $\overline{\delta\Phi}_k$, with the help of the sensitivity function, we obtain:

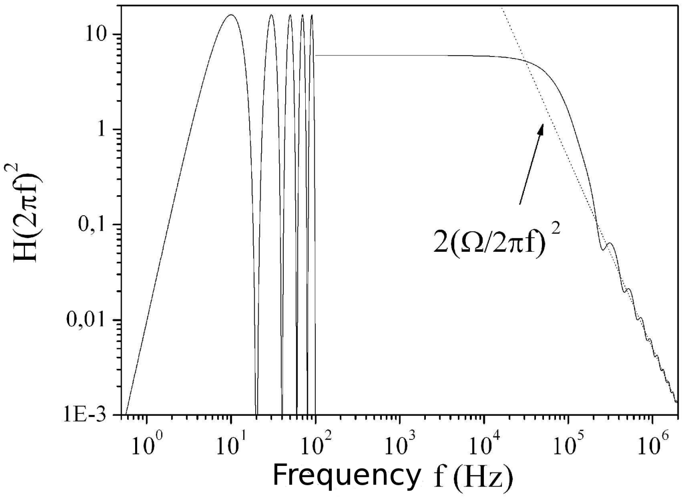

Figure 2.7: The square of the transfer function $H(2\pi f)$ for a typical values of $\Omega_R = 2\pi \times 50$ kHz and $T = 50$ms. The total value of the transfer function is shown for frequencies above 100 Hz [38, 69].

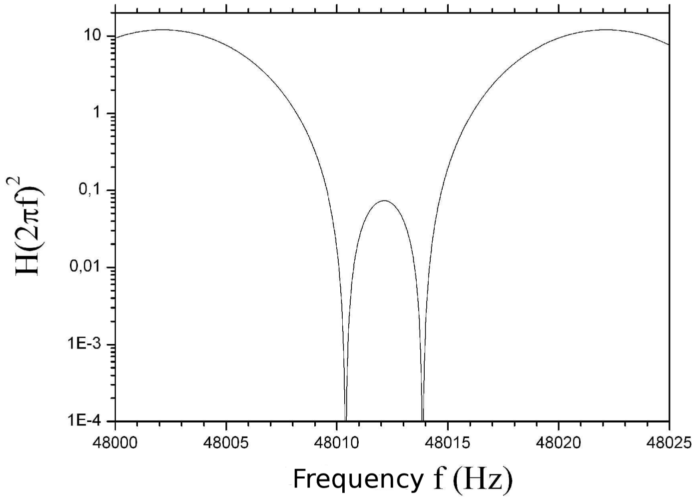

Figure 2.8: The square of the transfer function $H(2\pi f)$ around the Rabi frequency. The two zeros of the sensitivity function are shown, one at a frequency of multiple of $\frac{1}{T+2\tau}$, the other due to the last factor of the sensitivity function [38, 69].

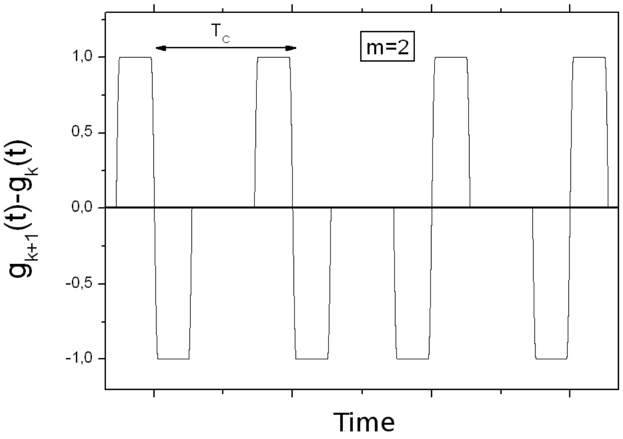

Figure 2.9: Sensitivity function associated to a two-measurements Allan variance [38, 69].

$$\begin{aligned}\overline{\delta\Phi}_k &= \frac{1}{m}\sum_{i=1}^{m}\int_{t_k+(i-1)T_c}^{t_k+iT_c} g_s(t-t_k-(i-1)T_c-T_c/2)\frac{d\phi}{dt}dt \\ &= \frac{1}{m}\int_{t_k}^{t_{k+1}} g_k(t)\frac{d\phi}{dt}dt \end{aligned} \tag{2.57}$$

with

$$g_k(t)=\sum_{i=1}^{m} g_s(t-kmT_c-(i-1)T_c) \tag{2.58}$$

defined as the sensitivity function for m measurement cycles.
The difference in sequence $\overline{\delta\Phi}_{k+1}-\overline{\delta\Phi}_k$ turns out to be:

$$\overline{\delta\Phi}_{k+1}-\overline{\delta\Phi}_k=\frac{1}{m}\int_{-\infty}^{+\infty}(g_{k+1}(t)-g_k(t))\frac{d\phi}{dt}dt \tag{2.59}$$

The figure 2.9 describes the sensitivity function corresponding to $\overline{\delta\Phi}_{k+1}-\overline{\delta\Phi}_k$. The goal is to compute the Allan variance for a random phase $\phi(t)$ characterized by a noise spectral density $S_\phi(\omega)$. For a sufficiently long integration time, the assumption that the measures are not correlated holds. Therefore, the Allan variance can be written as

$$\sigma_\Phi^2(\tau_m)=\frac{1}{2}\frac{1}{m^2}\int_0^{+\infty}|\omega G_m(\omega)|^2 S_\phi(\omega)\frac{d\omega}{2\pi} \tag{2.60}$$

in which $G_m(\omega)$ is the Fourier transform of $g_{k+1}(t) - g_k(t)$. $G_m(\omega)$ can be easily derived from $G(\omega)$ and the result is

$$|G_m(\omega)|^2 = 4\frac{\sin^4(\omega m T_c/2)}{\sin^2(\omega T_c/2)}\,|G(\omega)|^2 \tag{2.61}$$

The function $|G_m(\omega)|^2$ tends to a Dirac delta comb for increasing integration times:

$$\lim_{\tau_m\to\infty} |G_m(\omega)|^2 = \frac{2m}{T_c}\sum_{j=-\infty}^{+\infty}\sum \delta(\omega - j2\pi f_c)\,|G(\omega)|^2 \tag{2.62}$$

where $f_c = \frac{1}{T_c}$ is the cycle frequency. Replacing this expression into equation 2.60 the Allan variance simplifies to give finally

$$\boxed{\sigma_\Phi^2(\tau_m) = \frac{1}{\tau_m}\sum_{n=1}^{\infty} |H(2\pi n f_c)|^2\, S_\phi(2\pi n f_c) \tag{2.63}}$$

The equation 2.63 shows that the sensitivity of the interferometer is limited by an *aliasing* effect: the noise at any frequency multiple of f_c appears as a low frequency noise. This expression will be used later to evaluate the influence of laser phase noise. In the special case of white noise $S_\phi(\omega) = S_\phi^0$ one obtains:

$$\sigma_\Phi^2(\tau_m) = \left(\frac{\pi}{2}\right)^2 \frac{S_\phi^0}{\tau_m}\frac{T_c}{\tau} \tag{2.64}$$

From the last formula is evident that the interferometric phase noise increases by reducing the pulse duration is τ. As an example we evaluate the level of white noise corresponding to an interferometric phase noise of about 1 mrad rms for measurement. As a $\frac{\pi}{2}$ pulse duration we will take $\tau = 5$ μs and we consider $\tau_m \sim T_c$. According to previous equations the white noise spectral density will be less than or equal to -117 dBrad^2/Hz.

In the case of an atom gradiometer, two spatially separated atomic samples are interrogated by the same Raman light in order to realize two simultaneous atom interferometers. Consequently, most of the phase noise contributions are rejected thanks to the differential measurement.

Sensitivity to acceleration and vibration

The same formalism is also suitable to describe the sensitivity to vibration noise. As mentioned before the two Raman beams are overlapped and sent to the atoms through an optical fiber. Afterward they are retro-reflected to allow the counter-propagating Raman transition. The shift of an optical component before the retro-reflection does not induce, to first order, a differential phase shift. The interferometer is not sensitive to the movements of the optics except on the back reflection path. When the retro-reflection mirror moves of a quantity δz, the phase of the retro-reflected beam changes by $\delta\phi = 2\mathbf{k}_i\delta z \simeq \mathbf{k}_{eff}\delta z$. In a similar fashion as we did for the function $g_s(t)$, we define the sensitivity function to acceleration $g_a(t)$ with respect to an infinitesimal change in acceleration δ_a

$$g_a(t) = 2\lim_{\delta_a\to 0}\frac{\delta P_a(\delta_a, t)}{\delta_a} \tag{2.65}$$

$g_a(t)$ can be derived from the phase sensitivity function $g_s(t)$ by noting that:

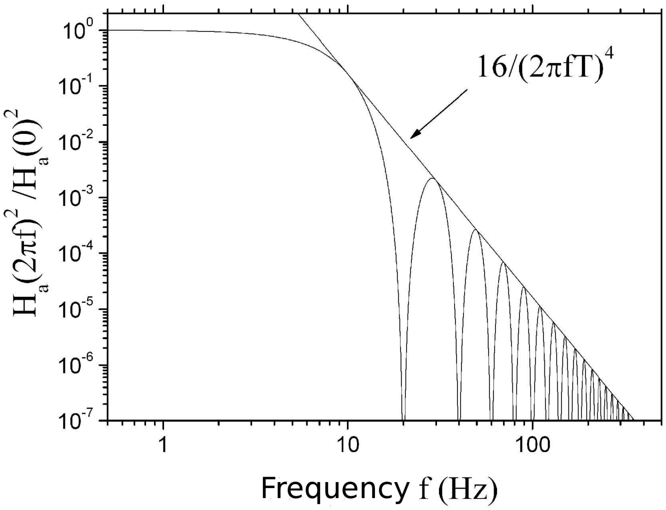

Figure 2.10: The square of the acceleration transfer function $H_a(\omega)$ for $2T = 100$ ms [38, 69].

$$g_s(t) = \frac{1}{k_{eff}} \frac{d^2 g_a(t)}{dt^2} \tag{2.66}$$

All that remains is to deduce the transfer function $H_a(\omega)$ associated to $g_a(t)$:

$$|H_a(\omega)|^2 = \frac{k_{eff}^2}{\omega^4} |H(\omega)|^2 \tag{2.67}$$

Starting from the acceleration noise spectral density $S_a(\omega)$ it is possible to calculate the Allan variance from the equation 2.63 also in presence of acceleration noise :

$$\boxed{\sigma_\Phi^2(\tau_m) = \frac{k_{eff}^2}{\tau_m} \sum_{n=1}^{\infty} \frac{|H(2\pi n f_c)|^2}{(2\pi n f_c)^4} S_a(2\pi n f_c) \qquad (2.68)}$$

The sensitivity function to acceleration is shown in figure 2.10. It behaves as a second order low pass filter with a cutoff frequency $f_0 = \frac{1}{2T}$. The value of this frequency is 10 Hz with $T = 50$ ms and therefore the system is not sensitive to high frequency vibrations.

If we are in presence of an acceleration white noise S_a^0, the interferometer sensitivity is:

$$\sigma_\Phi^2(\tau) = \frac{k_{eff}^2 T^4}{2} \left(\frac{2T_c}{3T} - 1 \right) \frac{S_a^0}{\tau} \tag{2.69}$$

As in the previous example, we want to stay below 1 mrad of interferometric phase shift per measurement. Consequently, the required acceleration white noise turns out to be 3×10^{-8} m/s^2/Hz$^{1/2}$ or less. The ground vibration noise is typically 2×10^{-7} m/s^2/Hz$^{1/2}$ at 1 Hz and rises up to about

5×10^{-5} m/s^2/Hz$^{1/2}$ at 10 Hz. As a consequence, a good seismic isolation system or a vibration correction method is mandatory for performing sensitive measurements.

Regarding the gradiometer case, the seismic induced noise is also well rejected, thanks to the differential measurement scheme.

2.2.4 Influence of the lasers propagation delay

The delay induced by the difference of the laser beams paths makes the interferometer sensitive to the fluctuations of the absolute frequency of the lasers [71]. As a consequence, such effect sets an ultimate limit on the sensitivity of an atom interferometer, independently by all the other parameters (free evolution time, momentum transfer).

In the following, we will use the formalism developed in the previous sections to evaluate the link between frequency and interferometric phase noise. The phase difference ϕ imprinted onto the atoms by the counter-propagating Raman beams is given by $\phi(t) = \phi_1(t) - \phi_2'(t)$, where $\phi_1(t)$ and $\phi_2'(t)$ are respectively the phases of the downward-propagating master laser and of the retro-reflected slave laser. If the atomic sample is placed at a distance L from the retro-reflecting mirror and considering a perfect Raman lasers phase coherence we can write:

$$\phi(t) = \phi_1(t) - \phi_2'(t) = \phi_1(t) - \phi_2(t - t_d) = \phi_1(t) - \phi_1(t - t_d) \tag{2.70}$$

where $t_d = 2L/c$ is the propagation delay. The interferometer phase shift Φ_d induced by fluctuation of ϕ can be expressed using the sensitivity function $g(t)$ previously described:

$$\Phi = \int_{-\infty}^{+\infty} g(t) \frac{d\phi(t)}{dt} dt = \int_{-\infty}^{+\infty} g(t) \left[\frac{d\phi_1(t)}{dt} - \frac{d\phi_1(t - t_d)}{dt} \right] dt = \int_{-\infty}^{+\infty} \left[g(t) - g(t + t_d) \right] \nu_1(t) dt \tag{2.71}$$

From this last expression it is possible to deduce the transfer function Z, which converts Raman laser frequency noise into interferometer phase noise σ_Φ. Passing into the frequency domain and after some algebra we get the following expression:

$$\sigma_\Phi^2 = \int_0^{+\infty} |Z(\omega)|^2 S_{\nu_1}(\omega) \frac{d\omega}{2\pi} \tag{2.72}$$

where $S_{\nu_1}(\omega)$ in the power spectral density (PSD) of the master laser frequency noise and $|Z(\omega)|$ can be written in terms of the transfer function $H(\omega)$ (see equation 2.54):

$$|Z(\omega)| = 2 \sin\left(\frac{\omega t_d}{2} \right) \frac{|H(\omega)|}{\omega} \tag{2.73}$$

The function $H(\omega)$ behaves as a low pass first order filter with a cutoff frequency $f_c \sim \tau^{-1}$. Considering that typically $t_d \sim 1 - 10$ ns and $f_c \sim 10 - 100$ kHz, we can assume that $f_c t_d \ll 1$. Therefore, the amplitude of the transfer function is finally:

$$|Z(\omega)| \approx t_d \, |H(\omega)| \tag{2.74}$$

In the case of a white frequency noise ($S_{\nu_1}(\omega) = S_{\nu_1}^0$), the interferometer phase noise becomes:

$$\sigma_\Phi^2 \approx \frac{\pi^2}{4\tau} t_d^2 S_{\nu_1}^0 \tag{2.75}$$

This last result gives a simple evaluation of the level of white frequency noise required to reach a given sensitivity, for given retro-reflection delay and Raman pulse duration. The same expression can be suitable also for an atom gradiometer. It is then quite straightforward to conclude that the gradiometer phase noise induced by the lasers propagation delays only depends on the clouds separation l, which yields $t_d = 2l/c$. Under our typical working condition ($l = 0.3$ m, $\tau = 12$ μs, $S_{\nu_1}^0 = 3.2\times10^4$ Hz^2/Hz), we obtain a differential acceleration sensitivity limit of $\sim 1.5\times10^{-9}$g/$\sqrt{\text{Hz}}$.

2.2.5 Phase shift calculation: general treatments

In the previous sections a purely quantum mechanical approach to the phase shift calculation has been presented. Such procedure is quite complete for resolving the simple case of constant gravity acceleration and it is particularly suitable to evaluate, through the use of the transfer function formalism, the effects of the phase noise on the interferometer readout. However, the resolution of the time dependent Schrödinger equation in presence of a general gravitational potential [77, 78] presents several difficulties, principally due to the very different nature of the atomic evolution during interactions with light fields compared to the periods of the free propagation. The most obvious solution to this issue is to treat separately the two cases and then combine the results. Moreover, if $\tau \ll T$, the interaction terms can be simply neglected considering beam splitters and mirror pulses as infinitesimally short.

In this context, we present here a quick overview of the two main theoretical treatments developed in the past years for analyzing a Mach-Zender interferometer $\pi/2 - \pi - \pi/2$ with temporal pulses separation T and atoms that follow a classical trajectory $z(t)$. The first, called path-integral method, is based on path-integral formalism while the second, called Bordé method, introduces significant simplifications.

The path-integral prescription [79] states that the total phase shift Φ can be computed from the sum of three terms:

$$\Phi = \Phi_e + \Phi_l + \Phi_s \tag{2.76}$$

Φ_e represents the free evolution term defined as

$$\Phi_e = \frac{1}{\hbar} \oint_\Gamma L(z, \dot{z}) dt \tag{2.77}$$

where Γ is the classical path and $L(z, \dot{z})$ the classical Lagrangian. Φ_l is defined as the sum of the Raman laser phase φ at the Raman pulse space time coordinates (z_i, t_i):

$$\varphi(z_i, t_i) = k_{eff} z_i - \omega_{eff} t_i \tag{2.78}$$

The rules to correctly sum such phase terms to obtain Φ_l can be found in [40].

Finally, the third term Φ_s represents the phase shift contribution due to the eventual path separation $\triangle z$ at the final $\pi/2$ pulse and it holds

$$\Phi_s = \frac{k_{eff} v \triangle z}{v_r} \tag{2.79}$$

where v_r is the recoil velocity and v the average output speed of the two interferometer paths [85].

The second method, widely explained in [80], asserts that the interferometer phase can be simply obtained using the following expression:

$$\Phi = k_{eff}\left(z_0 - z_1 - z_2 + \frac{z_3 + z_4}{2}\right) \tag{2.80}$$

in which z_0 is atomic position at the first $\pi/2$ pulse, z_1 and z_2 the positions at the central π pulse and z_3 and z_4 the positions at the final $\pi/2$ pulse.

Both methods are exact in the case of a quadratic Lagrangian. For instance, considering the case of a constant gravity gradient γ, described by the Lagrangian

$$L(z, \dot{z}) = \frac{1}{2}m\dot{z}^2 - mgz + \frac{m\gamma z^2}{2} \tag{2.81}$$

we obtain for both the presented approaches the following expression for Φ, setting $z_0 = 0$ as boundary condition:

$$\Phi = -k_{eff}gT^2 + \frac{k_{eff}\gamma T^3}{12}(12v_0 + 6v_r - 7gT) + \frac{k_{eff}\gamma^2 T^5}{360}(90v_0 + 45v_r - 31gT) \tag{2.82}$$

where v_0 is the initial atom velocity. In the case of a gradiometer, i.e. two interferometers spatially separated by a distance Δh, we can also evaluate the differential phase shift $\Delta\Phi_{grad}$:

$$\Delta\Phi_{grad} = k_{eff}\Delta h\gamma T^2\left(1 - \frac{7}{12}\gamma T^2 - \frac{31}{360}\gamma^2 T^4\right) \tag{2.83}$$

In our typical experimental conditions ($\Delta h \simeq 30$ cm, $T = 160$ ms and $\gamma \sim -2g/R_t \sim 3\times10^{-6}\text{s}^{-2}$, where R_t is the earth radius) the leading order in γ produces a phase shift of $\Delta h \times 1.12 = 0.336$ rad, while the second order is 4.5×10^{-8} times smaller (~0.015 μrad).

Regarding the more general case of a non-quadratic Lagrangian, often the exact solution is not evaluable. However, as described in [79], in presence of small non quadratic terms, a perturbative approach can be easily applied to both the presented techniques, giving reliable results at least to the first order.

2.2.6 Systematic shifts

Any external force induces an acceleration on the atomic motion and, consequently, a displacement of the atom with respect to the laser wavefronts. Previously we put our attention only on the phase shift induced by the acceleration of gravity. In this section we will discuss other possible phase shift sources that can contribute to the systematic error and thus they must be taken into account.

Effect of Raman wavefront

This effect depends essentially on the details of the front-wave distortions introduced by the retro-reflecting optics, which are not in common between the upwards and downwards Raman beams. During the interferometer sequence distortions are translated into an additional phase shift that affects atoms with a nonzero radial velocity. In principle, such offset can be numerically evaluated by studying the surface conformation of the interested optics. Unfortunately *in situ* analysis are not feasible. Consequently, deformations caused by mechanical stress cannot be taken into account. Also the attempt to extrapolate the interferometer phase shift at zero cloud temperature (no transversal atomic motion) does not give definitive results [87]. For all these reasons an accurate evaluation of this effect in a gradiometer is not trivial. It is reasonable to assume a partial compensation due to the fact that upper and lower interferometer share the same Raman light. In this sense an accurate clouds centering along the vertical can help to maximize the cancellation.

Coriolis force

Using the same procedure we are going to evaluate the effect on the phase shift due to rotation of the earth as well. In a rotating frame we are dealing with the Coriolis acceleration

$$\mathbf{a_c} = -2\mathbf{\Omega} \times \mathbf{v} \tag{2.84}$$

where $\mathbf{a_c}$ is the acceleration of the particle in the rotating system, $\mathbf{v}$ is the velocity of the particle in the rotating system, and $\mathbf{\Omega}$ is the angular velocity vector. Therefore the phase shift is equal to

$$\Delta\Phi_{rot} = -2\mathbf{v} \cdot (\mathbf{k}_{\mathrm{eff}} \times \mathbf{\Omega})T^2 \tag{2.85}$$

Atoms are approximately launched or released along the vertical direction, but the finite temperature of the ensemble implies a horizontal velocity spread. Furthermore, due to launch errors, $\mathbf{v}$ can have a small component perpendicular to $\mathbf{k}_{eff}$. Suppose now that the Raman beams propagate exactly along the vertical direction. If the interferometer measurement is performed at a latitude θ_l, the Earth rotation around its axis gives a contribution to the phase shift of

$$\Delta\Phi_{rot} = -2\Omega \mathrm{v}_{\mathrm{we}} k_{\mathrm{eff}} T^2 \cos\theta_l \tag{2.86}$$

where v_{we} is the horizontal velocity along the east-west direction. Here the horizontal velocity along north-south direction gives no shift being in the plane defined by $\mathbf{k}_{eff}$ and $\mathbf{\Omega}$. If two atomic clouds trajectories have different inclinations their horizontal velocity would be different, so a differential Coriolis term will rise

$$\Delta\Phi_{rot,up} - \Delta\Phi_{rot,dw} = -2\Omega\Delta \mathrm{v}_{\mathrm{we}} k_{\mathrm{eff}} T^2 \cos\theta_l \tag{2.87}$$

Our experiment is realized in Sesto Fiorentino (near Florence, Italy), that is located at a latitude θ_l= 43°50'07"N. Considering that Ω= 7.29×10^{-5} rad/s, for $T = 160$ ms and k_{eff}= 1.61×10^7 m^{-1} we have a differential shift of about 41 mrad for each mm/s of east-west velocity difference. This problem could be reduced for example using a different interferometer configuration by dropping atoms instead of launching them upwards. In this case the horizontal velocity transferred would be orders of magnitude smaller. If launching atoms is mandatory, a careful characterization of the trajectory has to be done.

Magnetic fields

To reduce the sensitivity to magnetic field only $m_F = 0$ atoms are involved in the interferometer. However second-order Zeeman effect will be always present and must be taken into account. The energy shift generated by a magnetic field B is described by the well-known Breit-Rabi formula:

$$U_m(z) = -\frac{\mu_B^2(g_J - g_I)^2}{2h\Delta_{hf}}B(z)^2 \tag{2.88}$$

where μ_B is the Bohr magneton, g_J and g_I are fine structure and nuclear Landè factors, h is the Planck's constant and Δ_{hf} the hyperfine splitting frequency. In presence of a vertical magnetic gradient, atoms are subject to an acceleration equal to

$$\boldsymbol{a_m} = \frac{1}{m}\nabla\left(\frac{\mu_B^2(g_J - g_I)^2}{2h\Delta_{hf}}B^2\right)\hat{\mathbf{z}} = \frac{2h}{m}\alpha B\frac{dB}{dz}\hat{\mathbf{z}} \tag{2.89}$$

where m is the ^{87}Rb mass and α is 575 Hz/Gauss^2 for D$_2$ transition. Considering a constant vertical magnetic gradient B' along the interferometer region and a distance Δh between samples, the corresponding bias Φ_m can be written as

$$\phi_m = \mathbf{k}_{\text{eff}}\left(\mathbf{a}_{\mathbf{m},\mathbf{Up}} - \mathbf{a}_{\mathbf{m},\mathbf{Dw}}\right)T^2 = k_{\text{eff}}\frac{2h}{m}\alpha\left(\triangle B_{Up-Dw}\right)B'T^2 = k_{\text{eff}}\frac{2h}{m}\alpha\Delta h B'^2T^2 \tag{2.90}$$

Under our experimental conditions ($B' \simeq 10^{-4}$ Gauss/mm, $T = 160$ ms and Δh=30 cm) corrections are in the order of $\simeq$ 5 mrad, corresponding to a few percent of the earth gravity gradient.

In addition to the mechanical effects, the magnetic field produces also an additional phase term ϕ_M directly connected to the small transition frequency change induced by the potential $U_m(z)$. To evaluate such term, it is sufficient to introduce $U_m(z)$ in the Lagrangian 2.81 and calculate

$$\phi_M = \frac{1}{\hbar}\oint U(z(t))dt = 2\pi\alpha\oint B(z(t))^2dt \tag{2.91}$$

This can be done with a good approximation performing the integration along the trajectory calculated neglecting the influence of $U_m(z)$.

For instance, let us suppose to turn a magnetic field on, uniform in the region around the atom (hence with no forces acting on it), during the second half of the interferometer sequence. Thus accumulated phase shift will be:

$$\phi_M = 2\pi\alpha\int_T^{2T} B(t)^2dt \tag{2.92}$$

A rectangular 10 ms long magnetic pulse of 100 mG, for example, provides a phase shift of 361 mrad.

Chapter 3

Experimental apparatus

In this chapter a complete description of the MAGIA experimental apparatus will be provided. More details can be found in [43, 44]. This chapter is organized in four parts. The first section describes the setup of the laser sources used to cool down and manipulate the atoms. A particular emphasis will be put on the novel *External Cavity Diode Laser* (ECDL) with interference filter and the new Raman laser system. A brief overview on the vacuum system of the experiment will be provided in the second section . The third part contains a full description of the 2D-MOT module recently installed in the experiment as an efficient cold atom source. Finally, in the fourth section, we will discuss about the source masses and their support.

3.1 Laser system

One of the most important issues of the experiment is to produce all the optical frequencies that are needed to perform mechanical and internal state manipulation of the atoms. To achieve this goal an appropriate choice of the laser sources is required. Furthermore a correct tuning of the laser frequencies respect to the Rb transitions is necessary. In this section a comprehensive explanation regarding these topics will be provided. Henceforth $\nu_{F\to F'}$ will label the ^{87}Rb transition frequency $\left|5S_{1/2},\, F\right\rangle \to \left|5P_{3/2},\, F^{'}\right\rangle$.

3.1.1 ECDL laser as light source

Nowadays in atomic physics experiments laser diodes are widely used as light sources thanks to their low price and large availability. Especially in the MAGIA experiment all transitions lie around 780 nm, which is easily accessible by laser diodes. Usually, the main disadvantage consists in their very wide spectrum (natural laser linewidth $\triangle\nu_d \sim 40$ MHz), much larger than the natural width of the typical atomic transitions employed ($\frac{\Gamma}{2\pi} \sim 6$ MHz). In order to fix this problem an external cavity is used to introduce an additional laser optical feedback and a wavelength selection element. For this purpose the most common setup is the *Littrow* configuration in which the diode laser output beam, once collimated, is sent on a diffraction grating (*Grating External Cavity Laser*, GECL) and the first diffraction order is sent back as optical feedback, while the zeroth order is the output beam. The external cavity is thus constituted by the diode laser surface and the diffraction grating. The laser line width is given by the scaling law [45]:

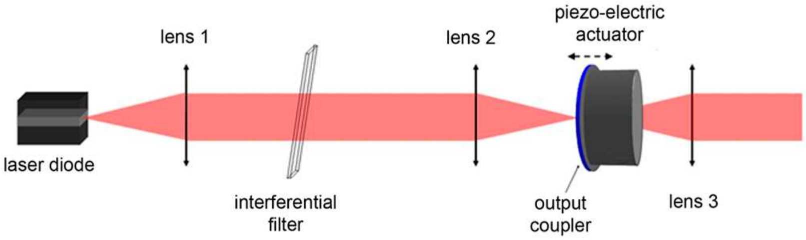

Figure 3.1: Schematic drawing of an extended cavity diode laser with interference filter [72].

$$\triangle v_{ECL} = \left(\frac{n \cdot l_d}{l_{ECL}} \right)^2 \triangle v_d \tag{3.1}$$

where n is the diode refractive index, l_d is the diode length and l_{ECL} is the external cavity length. For typical values ($n \sim 2$, $l_d \sim 1-2$ mm , $l_{ECL} \sim 5-10$ cm) we expect a reduction of the spectral width by a factor 100.

In terms of long term stability one of the weak point of the *Littrow* setup is due to the fact that the same element (the grating) acts as wavelength selector and optical feedback source. In the MAGIA experiment achieving long integration time without losing the lasers lock is crucial and a more stable ECDL geometry is required. Therefore, we decided to adopt a novel ECDL scheme realized by using a partially reflecting mirror as output coupler and an *Interference Filter* for wavelength selection (*Filter External Cavity Laser*, FECL [72]). The complete setup is sketched in figure 3.1 and can be summarized as follows: the beam coming from the diode is collimated by a first lens and travels into the cavity passing through the filter. Afterwards it is focused on a semi-reflecting mirror and a fraction of the light (10-30%) is back-reflected to realize the optical feedback. The remaining fraction is thus collimated again by a third lens to form the output beam. The fine frequency tuning is realized by the piezoelectric crystal that holds the mirror. This is the so called *cat's eye* configuration.

This mounting scheme has many remarkable properties. First, the injection is preserved for a large number of defects in the alignment of the cavity and the piezoelectric crystal movement does not change at all the beam pointing. Indeed when the beam focal point is placed on the mirror surface the sensitivity to mirror misalignment is strongly reduced. Second, the interference filters have a maximum transmission at 780 nm for an incident angle of 6° respect to the normal and an acceptance angle of ±1° (see figure 3.2).

As a consequence, the selected frequency will be also less sensitive to mechanical misalignment of the filter. To have a rough comparison, for GECL $\left(\frac{d\lambda}{d\theta}\right) \sim 1.4$ nm/mrad instead for FECL $\left(\frac{d\lambda}{d\theta}\right) \sim 23$ pm/mrad [56]. For all these reasons we decided to replace almost all the lasers of the experiment with home made FECL.

3.1.2 Reference laser

To cool and manipulate ^{87}Rb atoms particularly suited is the $\nu_{2\to3}$ transition. Thus an active frequency stabilization on it is the best choice to produce a reference optical frequency for the experiment. At this scope, we decided to implement the Modulation Transfer Spectroscopy (MTS)

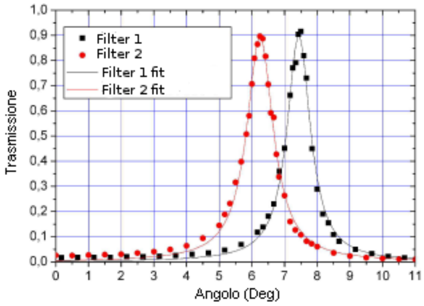

Figure 3.2: Transmission curves of two filter within the same set as a function of the angle of incidence at 780 nm [44].

technique as a frequency lock method [67]. Such method has several advantage: firstly the zero-crossing point of the modulation transfer error signal is accurately centered on the corresponding atomic transition; secondly, the locking point is almost immune to power fluctuations of the laser.

The output light from a FECL (diode laser model ADL-78901TX, Laser Components, output power P_{op} =100 mW CW, operative current $I_{op} \sim$ 140 mA) is sent to an AOM that increases its frequency by +184.2 MHz. Afterwards the beam is split into two parts called *pump beam* and a *probe beam*: the probe beam goes straight into a heated (∼ 35°C) and magnetically shielded rubidium cell and detected with a fast photodiode. The pump beam passes through an Electro Optical Modulator (EOM) that creates sidebands at 5 MHz (modulation index ∼ 0.1) and finally superposed to the probe path in the rubidium cell in counter-propagating configuration. The modulation is transferred onto the probe beam by four-wave mixing. The signal from the fast photodiode is electronically demodulated with the 5 MHz signal driving the EOM. A dispersive signal across the rubidium subDoppler lines is obtained. A double loop control for low and high frequencies locks the laser frequency to the atomic resonance. The low frequency loop covers a bandwidth up to 1 kHz acting on the piezo while high frequency noise (up to 120 kHz) is corrected acting on the laser current. The laser is locked on the sub-Doppler line corresponding to $\nu_{2\to3}$, but the actual output frequency is $\nu_{REF} = (\nu_{2\to3} - 184.2 \text{ MHz})$, because of the AOM between laser source and rubidium cell. Before and after the AOM part of the light is picked-up for frequency locking the other lasers.

3.1.3 Detection laser

A diode laser (Sharp GH0781JA2C) providing 60 mW at 110 mA is optically injected with the off resonant reference light (ν_{REF}). The side port of an optical isolator is used for the injection. A double pass into an AOM is needed for increasing the laser frequency by +183.6 MHz, i.e. $\nu_{DET} = (\nu_{2\to3} - 800 \text{ kHz})$. The light beam is coupled into two different optical fibers going towards the apparatus.

3.1.4 Cooling and Repumping laser

The appropriate laser radiation to realize an efficient cooling process as been demonstrated [68] to be -3Γ detuned[1] from the $\nu_{2\to3}$.[1] A ^{87}Rb atom in the $F = 2$ ground state that absorbs this radiation has a high probability of ending up in the excited state$F' = 3$, then it spontaneously decays back in the $F = 2$ state because of dipole selection rules. But there is a non zero probability (about 0.1%) that it goes in the $F' = 2$ state. From this excited state it can either decay into the $F = 1$ or into the $F = 2$ ground states. Since stimulated absorption and spontaneous emission cycling rate is of the order of Γ, all the atoms would be rapidly lost in the $F = 1$ channel if no repumping occurs. Thus a repumping radiation, slightly detuned from $\nu_{1\to2}$ transition is used for this purpose.

In order to produce the cooling light, a FECL (diode laser model ADL-78901TX, P_{op} =100 mW CW, $I_{op} \sim 140$ mA) and a tapered amplifier (TA) (EYP-TPL-0780-01000, P_{op} =1 W CW, $I_{op} \sim 2.5$ A) are used. The FECL output beam is divided in two parts: a large amount ($\sim$ 20mW) injects the TA while a small part ($\sim 2-3$mW) is overlapped with resonant ($\nu_{2\to3}$) reference light and their beat note signal is collected on a fast photodiode (Hamamatsu G 4176-03). The beat note, together with an RF signal (184.2 MHz), is sent to a phase frequency detector (PDF) that provides an error signal. This signal is used to perform a phase-frequency lock acting on piezo and current (loop bandwidth 1 MHz). The resulting frequency is again $\nu_{2\to3} - 184.2$ MHz. The TA provides an output of 800 mW ($I = 1.7$ A) that is split into two parts traveling along independent optical paths. Each path consists of a double pass through an AOM and a fiber in-coupling. The two AOMs are independently driven by two RF signal ($\sim$80 MHz), in order to tune the light around $\nu_{2\to3}$.

The repumping light is generated by two diode lasers (Sharp GH0781JA2C, P_{op} =120 mW CW, $I_{op} \sim 160$ mA) arranged in a master-slave configuration. Part of the master laser is overlapped with the reference light and collected on a fast photodiode. The beat note so obtained is down converted with the third harmonic of a programmable synthesizer (ADF4360-1 stabilized VCO) set to 2216.6 MHz and then frequency locked to a 40 MHz signal through a PFD and the usual feedback channels (piezo + current, loop bandwidth 300 kHz). The master laser actual frequency is ($\nu_{1\to2} - 62.4$ MHz). Part of this light is used to inject the slave laser and the rest is shifted by -172.2 MHz in a double-pass AOM. Resulting light has a frequency close to the $\nu_{0\to1}$ transition. The output beam of the slave laser is directly sent to an AOM increasing its frequency by $+68.0$ MHz, obtaining an optical frequency of ($\nu_{1\to2} + 5.6$ MHz).

3.1.5 Raman laser system

The Raman beams are generated by two home-made MOPA systems with an output power of about 1 W each (see figure 3.3) [46]. Two FECL are phase-locked with an offset frequency of about 6.8 GHz generated by a low phase noise microwave synthesizer (Anritsu MG3692A). In addition, one of the two lasers (master laser) is frequency-locked with an offset of about 2 GHz to the $F = 2 \to F' = 3$ transition, by detecting the beat note with a frequency stabilized laser (the MAGIA reference laser). The loop is closed acting only on the laser piezo, achieving a loop bandwidth of few kHz. Each laser beam injects an independent tapered amplifier (TA). The apparatus previously employed in the experiment was based on two grating tuned diode lasers in Littrow configuration, whose output beams were spatially overlapped to inject a single TA. The new system has several advantages. Indeed, FECL have lower intrinsic frequency noise than Littrow grating stabilized lasers, improving

---

[1] [1]Γ is the atomic natural linewidth and is $2\pi \cdot 6.065(9)$ MHz for ^{87}Rb as reported in appendix A.

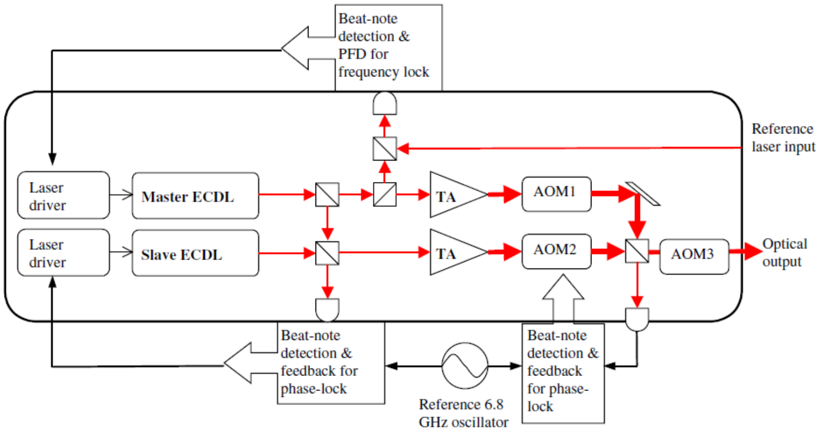

Figure 3.3: Scheme of the Raman laser system.

considerably the locking time and stability. In addition, using two independent TAs instead of a single one allows independent manipulation and control of the two Raman beams. Such a scheme also provides higher optical power for the Raman beams. The higher Rabi frequency allows shorter $\pi/2$ and π pulses, which should eventually lead to more atoms in the interferometer and higher contrast, i.e. a higher SNR. In our setup, the available power for Raman beams is about 260 mW. Our Raman laser system features a double-stage optical phase-locked loop (OPLL). The primary OPLL detects the beat note between the two FECL beams before injecting the TAs, in order to minimize the signal propagation delay, i.e. to maximize the loop bandwidth. The beat note is mixed with the 6.8 GHz reference frequency and the down converted signal is compared with a reference frequency generated by a direct digital synthesis (DDS) generator in a fast digital phase-frequency detector (Motorola MC100EP140). The DDS frequency is swept around 40 MHz with a phase-continuous linear frequency ramp to compensate for the change in Doppler effect during the interferometric sequence. The resulting error signal is filtered and used to drive two actuators on one of the FECL (slave Raman laser), the voltage of the piezo holding the output coupler and the injection current of the laser diode. The loop bandwidth on the injection current is about 4 MHz. In figure 3.4 the Master/Slave laser beat note is shown.

The output beams from the TAs are passed through two AOMs for independent power control and are finally recombined in a polarizing beam splitter. A third, single-pass AOM is used for pulse control just before coupling the Raman beams into an optical fiber for delivery to the atom interferometer. We also apply an auxiliary, low-bandwidth loop in order to compensate for the phase noise introduced through the differential path of the two Raman laser beams before they are recombined in the optical fiber; to such purpose, we detect the beat note between the Raman laser beams at the polarizing beam splitter before AOM3 (see figure 3.3); in order to reduce any beam-motion induced error in the Raman phase, we inject the beat note light into an intermediate optical fiber before sending it to the photodetector; we mix the beat note with the 6.8 GHz reference frequency and we use another fast digital phase-frequency detector to compare the down converted signal with the same 40 MHz reference frequency employed in the primary loop. The resulting error signal is properly filtered and used to control a voltage-controlled crystal oscillator (VCXO) driving

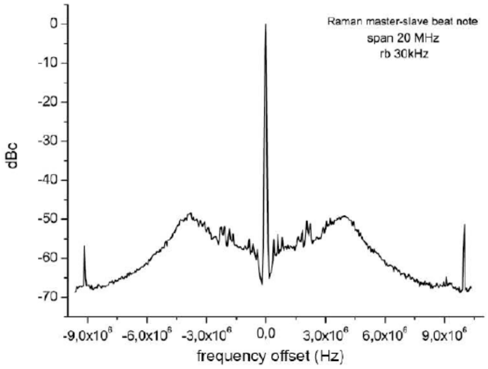

Figure 3.4: Beat note between Raman lasers.

the frequency of the AOM after the TA of the slave Raman beam. The resulting loop bandwidth is about 150 kHz. Moreover, analyzing the beat signal, we also noted that the ASE (amplified spontaneous emission) background from the TAs is below the resolution of our spectrometer (~80 dB). For that reason and for the further rejection due to differential nature of the experiment, we decided to not use any Rb filter cell on the Raman beam in order to save optical power.

Figure 3.5 shows the phase noise spectral density measured in different conditions: after the primary loop, after the optical fiber with the secondary loop open and after the optical fiber with the secondary loop closed. The excess noise with respect to the primary loop is mainly due to the phase noise of AOM1 (see figure 3.3). The resulting phase noise spectral density is below $4\,\mu\mathrm{rad}/\sqrt{\mathrm{Hz}}$ at frequencies above 10 Hz.

3.2 Vacuum system

Laser cooling and manipulation of Rb atoms can be realized only in a UHV environment ($\sim 10^{-9}-10^{-10}$ Torr), in order to minimize collisions with thermal background gases. Furthermore the materials employed in the apparatus must be amagnetic and having high resistivity, in order to avoid induced magnetic fields. For this reasons the MAGIA vacuum system has been carefully designed to achieve these performances [44]. Figure 3.6 illustrates schematically the entire apparatus. It consists of a lower trap chamber, a long vertical tube and a central chamber for detection.

3.2.1 Trap chamber

The cell for magneto-optical trap (MOT) was made of Titanium Alloy ($\mathrm{TiAl_6V_4}$) which has peculiar properties that make it particularly suitable: it is particularly light (4430 kg/m^3), hard, non magnetic and it has a high resistivity (168 $\mu\Omega$cm). This last physical property is useful to quickly damp undesired eddy currents induced by varying electromagnetic fields. Moreover, its thermal expansion coefficient matches very well with that of the BK7 glass used for optical windows. The chamber was machined starting from a 15 cm cube by cutting all the edges orthogonally to the diagonals. In this way we can obtain 14 faces nearly equidistant from the center of the cube. Or-

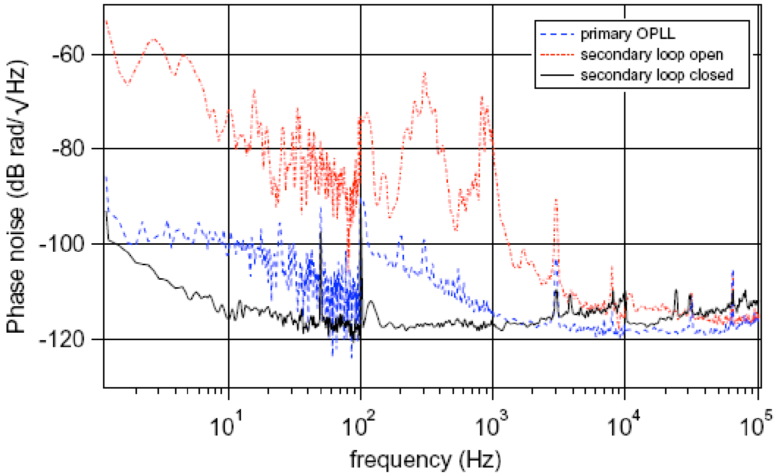

Figure 3.5: Phase noise spectrum of the beat signal between the two Raman laser beams measured in different conditions: after the primary loop (blue dashed curve); after the optical fiber with the secondary loop open (red dash-dotted curve); after the optical fiber with the secondary loop closed (black solid curve).

thogonally to the six square faces was made a circular hole with a diameter of 50 mm, while on the remaining eight triangular faces, a hole smaller than 35 mm in diameter. This procedure allows to have 14 optical access to the center of the cube where the MOT is created. The trapping beams are in the usual 1-1-1 configuration. For fine adjustment of the launching direction this chamber was not rigidly fixed to the rest of the apparatus, but connected with a flexible bellow. Once it is positioned in the desired orientation the cube can be fixed to the optical table independently from the rest of the vacuum system.

3.2.2 Interferometer tube

As previously stressed atom interferometer is very sensitive to magnetic fields. For this purpose a vertical tube made of the non magnetic, high resistivity material $TiAl_6V_4$ was realized. The tube is 1 m long and has an external diameter of only 4 cm (internal: 3.5 cm) to permit a close positioning of the source masses. These dimensions were chosen also to be able to send through the apparatus Raman beams with a waist of 10 mm, thus with wavefronts flat enough to neglect the effect of their curvature on the region occupied by the atomic ensemble, and simultaneously with reduced scattering from the side walls. A coil is wrapped around the tube to apply a magnetic field along the vertical axis that defines a quantization axis for the atoms. Finally 10 shorter coils are wrapped one above the other around the long one in order to be able to produce localized magnetic fields. A double-layer μmetal shield placed around the tube and its coils is employed to attenuate external magnetic fields. The shield is composed by two coaxial 0.76 mm thick cylinders of 1028 mm length and diameters of 74 and 95 mm respectively extending along the entire tube. In the central region the axial fields are attenuated by 69 dB and radial ones by 76 dB [44]. Fields of about 50 G saturate

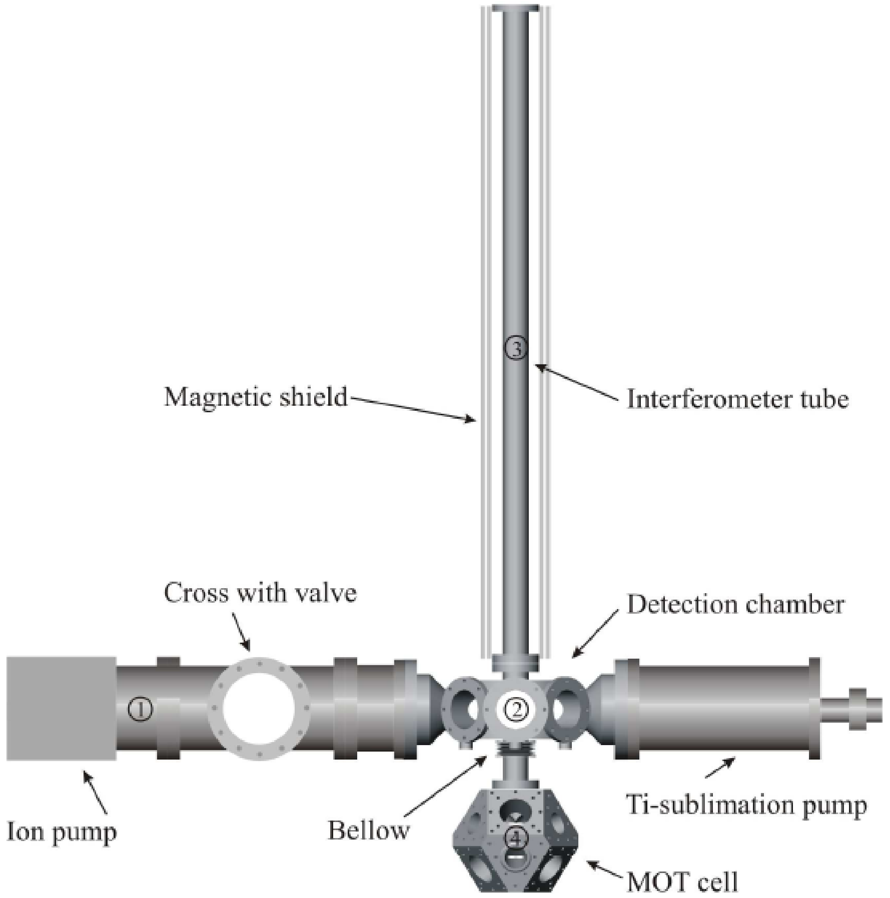

Figure 3.6: The MAGIA apparatus. The experiment is performed in the central part where the atoms are cooled (MOT cell), manipulated and detected (Detection chamber) and opposed to interferometer pulses (Interferometer tube). Vacuum pumps are attached on the left and right of the detection chamber. The height of the whole apparatus is about 1.5 m [43].

the μmetal shield.

3.2.3 Detection chamber

The detection chamber was placed immediately over the MOT chamber and rigidly connected to the interferometer tube. It is made of non-magnetic stainless steel 316LN. It provides 6 AR coated windows of 60 mm diameter for optical access and is connected by two CF100 flanges to a titanium sublimation pump and an ion pump. The detection chamber is used for state preparation and state-sensitive detection.

3.2.4 Pumping system

To keep the entire system under vacuum we use a 75 l/s ion pump (Varian VacIon 75 Plus Star Cell, driver MidiVac) connected by large CF100 tubes to the detection chamber. It is placed far from the experiment (55 cm) to allow the strong magnetic fields to decay below 0.5 Gauss. Also a titanium sublimation pump (THERMIONICS SB-1020 with driver Varian 9290023) is installed for effective pumping of gases like H_2 and N_2. The combination with an ion pump is important for the non-gettarable gases like Ar or CH_4.

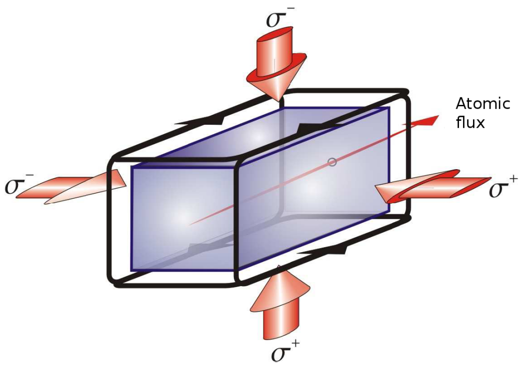

Figure 3.7: Scheme of a 2D-MOT. Atoms in an elongated vacuum cell with a high rubidium background pressure are transversally cooled by 4 laser beams, indicated by arrows. A thin collimated beam of atoms will escape the 2D-MOT on both sides, on one side onto the window and on the back side through a small hole towards the UHV region. The 2D magnetic quadrupole field is provided by 4 coils outside the cell [44].

3.2.5 2D-MOT

In atomic interferometry experiments, it is highly desirable to reach a condition of low background pressure and a fast MOT loading at the same time. Using standard atoms sources, like Rb dispensers, there is an obvious trade-off between these two features. Indeed, a high Rb vapor density is important for a fast MOT loading, but it also degrades the vacuum, inducing higher atom losses during the ballistic flight and more background fluorescence at detection. To achieve fast loading

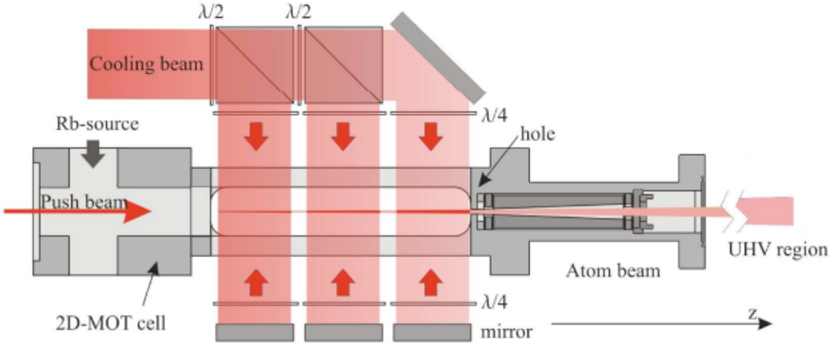

Figure 3.8: Scheme of the 2D-MOT system implemented on the MAGIA experiment [44].

rates while preserving a very low background pressure in the MAGIA vacuum system, a high flux atomic source based on a 2D-MOT has been implemented [47, 48]. Figure 3.7 shows a scheme of principle of the device. The operation is based substantially on the same criteria of 3D-MOT, limiting the cooling on the transverse directions in order to obtain a flux of atoms.

2D-MOT setup

The vacuum system (see figure 3.8) is composed of a piece of titanium closed on four lateral sides by rectangular windows and on one backside by a circular window. On the other end is placed a 1.5 mm diameter hole that allows the slow atoms flux to escape from the chamber. The circular window (25 mm diameter) allows to inject the pushing laser along the trap axis. This beam will accelerate the atoms towards the hole, particularly those with negative or small longitudinal velocity components, in order to increase the atomic flux. The four rectangular windows (90×25 mm^2) are used to send the trapping light on each of two axes perpendicular to the direction of the outgoing atomic beam. Cooling beams are split into three paths by a system of two 24.5 mm polarizing beam splitter + $\lambda/2$ wave plate + mirror. On the other side three mirrors provide to back reflect each beam, and six $\lambda/4$ wave plate provide for the circular polarization.

The vacuum is maintained by an ion pump having a 2 L / s pumping speed. The rubidium vapor is released from a reservoir connected to the back of the trap through a valve that permits, if necessary, to isolate the source of rubidium. The magnetic field of the trap is generated by two sets of coils with rectangular dimensions (15×5 cm^2) and 100 windings placed in front of the lateral windows. The coils are connected in series and create a magnetic field gradient of 20 G/cm at the center of the trap.

The laser system used to operate the 2D-MOT is based on a home-made TA with an output power of about 500 mW ((EYP-TPL-0780-0500, P_{op} =0.5 W CW, $I_{op} \sim 1.5$ A). The master is an extended cavity diode laser using an interference filter for wavelength selection. Two double-pass AOMs allow independent frequency and power tuning of the cooling and pushing beams

2D-MOT characterization and optimization

The measurements performed after the integration of the 2D-MOT on the main apparatus were finalized to confirm the advantages for the gradiometer in terms of loading rate and background pressure reduction. In order to obtain the best performance also a careful optimization of all the parameters was done.

An estimate of the background pressure and loading rate can be derived by fitting the 3D-MOT fluorescence signal during the loading phase according the *Antoine Equation*:

$$N(t) = \frac{R}{\Gamma_c}(1 - \exp(-t\Gamma_c)) \tag{3.2}$$

where R is the loading rate, Γ_c is the collisional loss rate and t the loading time. From Γ_c is possible to determine the background pressure. The accuracy of this measurement is strongly limited by the lack of knowledge of the gas composition in the 3D-MOT chamber. However, it is reasonable to suppose that Rb is largely the most present. To have a comparison with the previous MAGIA setup we took two set of measurements: one using the old Rb dispenser and other three using the 2D-MOT at different 2D-MOT Rb oven temperatures (see figure 3.9a).

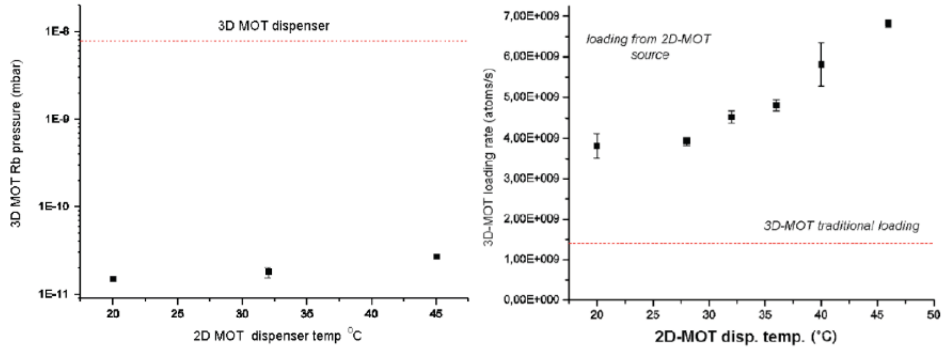

Figure 3.9: (a) Background Rb density in the UHV chamber versus temperature of Rb oven in the 2D-MOT system; (b) Loading rate from 2D-MOT versus temperature of Rb oven.

The Rb density is reduced by more than two orders of magnitude and is almost independent from the background pressure in the 2D-MOT chamber. Figure 3.9(b) shows typical values of the MOT loading rate versus the temperature of the Rb oven in the 2D-MOT system. When compared to the Rb dispenser previously employed the MOT loading rate can be increased by up to a factor 5. In order to achieve this high flux condition several optimizations were made, principally regarding alignment and accurate frequency and power tuning of the most sensitive beams (pushing beam in particular). In figure 3.10 is shown the behavior of the atomic flux with respect to the cooling frequency and total power. A similar operation was made also for the pushing beam (see figure 3.11).

Optimal atomic flux from the 2D-MOT source is found when the optical frequencies of cooling and pushing beams are red detuned from the $F = 2 \rightarrow F' = 3$ transition by 1.3Γ and 2.2Γ, respectively. Regarding the power dependencies we found 1 mW for the pushing beam while for

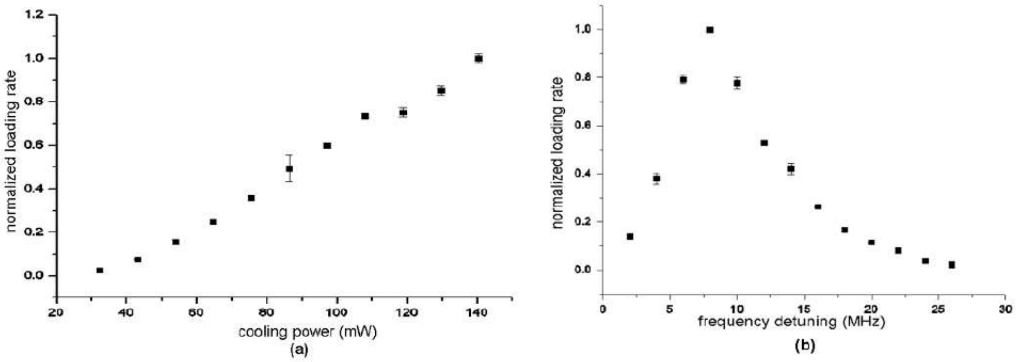

Figure 3.10: 3D-MOT loading rate as a function of 2D-MOT cooling total power (a) and as a function of cooling beam frequency detuning from resonance (b).

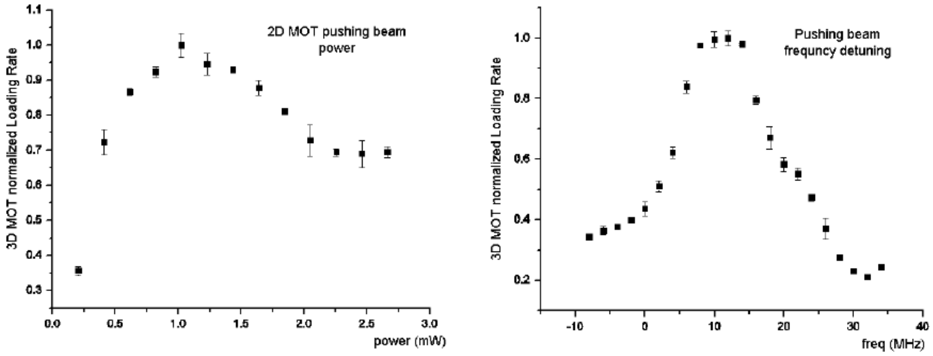

(a) (b)

Figure 3.11: 3D-MOT loading rate as a function of 2D-MOT pushing total power (a) and as a function of pushing beam frequency detuning from resonance (b).

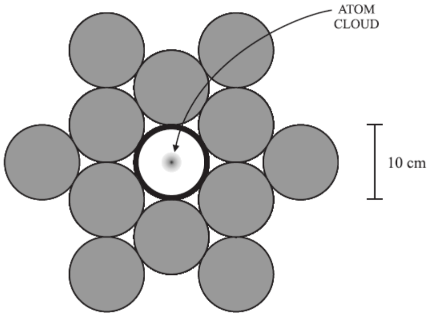

Figure 3.12: Geometrical arrangement top view of one set of 12 cylinders. The central ring is the vacuum tube in which the atoms vertically move.

the cooling we are still far from the saturation. Therefore, if needed, we can further increase the loading rate rising up cooling power. Currently we achieved a maximum loading of $\sim 2 \times 10^{10}$ atoms/s, corresponding to a capture efficiency of 40% [56].

3.3 Source mass and support

One of the parameters that mostly affect the accuracy of the G measurement is the knowledge of the relative positions between atoms and mass sources. Also the choice of appropriate materials and the best geometric configuration are key points of the experiment. In this section, after a brief introduction of the apparatus and a summary of past measurements (for more details see [52]), we will discuss about the recent characterizations of the source masses and improvements on the knowledge of their geometrical arrangement. Regarding the required accuracy level, a comprehensive analysis can be found in section 4.6.2.

3.3.1 Introduction to the apparatus and past measurements

Geometrical arrangement

As source masses we use 24 tungsten cylinders with a nominal diameter of 100 mm and a height of 150 mm. They are divided into two sets of 12 cylinders and are symmetrically arranged on two holders around the interferometer tube, as shown in figure 3.12.

The adopted symmetry prevents induced horizontal acceleration while along the axis produces a maximum vertical acceleration of $\sim 1.6 \times 10^{-9}$ m/s^2. Furthermore, having many small masses allows greater flexibility in positioning as well as in the control of the inhomogeneity. The main disadvantage lies in the need to know at micrometer level the position and shape of each cylinder.

Materials and realization

Well defined source masses with a high density are needed in an experiment that aims to measure the gravitational constant G. Among all eligible materials, the sintered tungsten (Inermet IT180)

material	Inermet IT180
composition	W 95.3% Ni 3.2% Cu 1.5%
radius height	50 mm 150 mm
nominal density	18000 kg/m^3
elasticity modulus	360 Gpa
rigidity modulus	140 Gpa
hardness	298 HV 10
resistivity	12×10^{-8} Ωm
thermal conductivity @ $\rho = 18000$ kg/m^3	110 Wm^{-1} K^{-1}
linear thermal expansion @ 20°C	5.2×10^{-6} K^{-1}
volume magnetic susceptibility	66×10^{-5}

Table 3.1: Physical properties and dimensions of Inermet IT180 cylinders used for the final G measurement.

is capable of combining experimental and cost requirements. In table 3.1 some salient physical properties are listed.

Cylinders were realized by melting (1500 °C) a hydrostatically pressed mixture of tungsten grains (10-50 μm) with small percentages of copper and nickel. After this process blocks were cooled down to room temperature while nickel and copper solidify bonding tungsten grains. Each block was machined in order to obtain the desired cylindrical shape. Afterwards several analysis (microscope and ultrasonic tests) were performed to evaluate the material homogeneity. As a result the presence of 100 μm holes was found. In order to reduce drastically dimension and number of these holes, cylinders were subjected to a further treatment called *hot isostatic pressing* (HIP). HIP is a manufacturing process used to reduce the porosity of metals and increase the density of many ceramic materials. The HIP process subjects a component to both elevated temperature and isostatic gas pressure in a high pressure containment vessel. After this operation the density is increased by 1%.

Support and elevator

In our experiment the source masses must be supported and translated vertically with high accuracy. The mass holder and elevator was designed strong enough to hold all the cylinders without observable bending or deformations and with independent positioning control for the two sets of masses. In figure 3.13 a picture of the mass holder is shown.

The movable parts are two large disk-shaped platforms with a hole in the center large enough to fit the interferometer tube and the magnetic shields. Density and shape of platforms can be found in [43]. The knowledge of this parameters are relevant since they contribute to a small part of the interferometric signal although in a less critical way than the source masses. Each platform is held and moved by two 480 mm long precision screws that have a diameter of 15 mm and a pitch of 10 mm. The movement of each screw is controlled by a step motor with an angular resolution of 1.8° followed by 30:1 gear in order to be able to reach a 1.7 μm of resolution in vertical displacement. Each platform is monitored by an optical encoder fixed on the rigid structure while the pointer is

Figure 3.13: Picture of the mass holder and elevator. Two of the four legs are visible on the bottom; above them the reference horizontal plate and the four columns connected on the top by a circular plate. The two moving platforms are holding two sets of cylinders.

connected to the platform. The reading accuracy and reproducibility is 1 μm.

Destructive density test

The knowledge of the homogeneity degree is fundamental for a correct evaluation of the source masses influence in the G measurement. For this purpose a destructive test on a single cylinder was performed, assuming that all the other cylinders have a similar density distribution. The cylinder was cut into 15 parallelepiped shaped blocks with a squared basis (25.2×25.2) mm^2 and 43.9 mm high and then volume and weight of each block was measured. A relative density variation of 6.6×10^{-4}, considering the standard deviation, and 2.6×10^{-3}, considering the maximum density difference was found. Moreover, a clear density reduction is observed when moving towards the center both in the radial and in the axial direction. These informations are essential to evaluate an upper limit of the systematic shift on the G measurement due to the density inhomogeneity.

3.3.2 New characterization measurements

Shape and position of each cylinder must be determined with micrometric accuracy. Consequently all the cylinders were further machined and polished in order to regularize the shape as much as possible. Additionally, a conical hole was placed in the center of each cylinder base to easily perform position evaluation using small steel spheres. Therefore new shape and weight measurements were required.

Surface studies

We investigated the shape of each cylinder with a contact 3D scanner (Brown & Sharpe Scirocco-dea) able to perform position measurements with 1 μm accuracy. This instrument is based on a translation system in three dimensions and a calibrated spherical ruby tip linked to a force sensor. When the tip touches a surface, the force sensor is activated and the three coordinates (x,y,z) are recorded. Collecting a sufficient number of points is possible to reconstruct simple geometric forms. We took points on both top faces to determine height and perpendicularity of each cylinder, on the lateral surface to determine radius and tilt, on the conical hole to determine its center. This was done measuring the hole circular base 0.2 mm below the top surface and evaluating the relative coordinates (x,y) between circle and cylinder center. Moreover, we labeled each cylinder with a number to be easily recognizable. Results are reported in table 3.2.

Orthogonality and tilt are always within 300 μrad. Maximum and total offset of the conical hole are about 25 μm 6 μm respectively. Height is slightly variable (values difference up to 37 μm) while diameter is more uniform (12 μm of maximum variability). Average values are (150.107±0.007) mm height and (99.895±0.003) mm diameter.

Precision weighing

To perform accurate mass measurements we decided to compare each tungsten cylinder with a sample mass (21500 g) characterized at the milligram level. We used a precision balance with a 1 mg resolution (courtesy of INRIM). To achieve this accuracy level several precautions were taken. We canceled instrument drifts weighing several times the sample mass and the unknown masses and taking the average value of the mass difference. We monitored environmental parameters such as temperature (±0.1 °C), relative humidity (±1%) and pressure (±1 mbar) to evaluate air buoyancy corrections. Results are reported in table 3.3 together with the calculated densities.

Average values for mass and density are 21489±3 g and 18.263±0.002 g/cm^3. By comparison with [43], the additional machining has made cylinder dimensions more uniform, leading to a better knowledge of the volume. As a consequence, the standard deviation on density has decreased by a factor three.

Position measurements by laser tracker

After finishing the measurements on individual cylinders we placed them back on the two holding platforms, trying to get the most regular arrangement with the help of a caliper. Afterward, taking conical holes as measuring points, the 3D position of each cylinder was evaluated using a laser tracker with a resolution of 1.26 μm. Regarding the reference frame, z axis was taken parallel to the gravity within 10 μrad while support platform edges were chosen as x, y axes. Data analysis shows that in each holding platform both the inner and outer cylinders are laying along concentric circles within 10 μm. Therefore we can use circles centers as a tool to describe the collective behavior of the source masses in each of the two configurations (F and C, see figure 1.2). Since Raman lasers are our ultimate reference system, we placed an iris aligned according to the Raman beams center and its position was also measured. All the results are shown in table below and plotted in figure 3.14.

	x (mm)	y (mm)	z (mm)
Lower platform, Close	410.796	449.979	357.667
Lower platform, Far	410.794	450.009	244.499
Upper platform, Close	410.127	449.737	527.729
Upper platform, Far	410.116	449.724	687.768
Reference iris	410,134	449,916	1056,355

Cylinder number	Height (mm)	Diameter (mm)	Hole offset (x,y) face 1 (μm)	Hole offset (x,y) face 2 (μm)	Orthogonality face 1	Orthogonality face 2	Tilt
1	150.116(1)	99.894(1)	(13,1)	(2,1)	0.99999995	1.00000000	0.99999998
2	150.114(3)	99.898(1)	(5,1)	(7,1)	1.00000000	1.00000000	1.00000000
3	150.116(1)	99.898(1)	(1,2)	(4,1)	1.00000000	1.00000000	1.00000000
4	150.109(3)	99.897(1)	(5,1)	(13,2)	1.00000000	1.00000000	1.00000000
5	150.106(1)	99.895(1)	(8,1)	(5,1)	0.99999999	1.00000000	1.00000000
6	150.102(3)	99.894(1)	(25,1)	(6,2)	1.00000000	1.00000000	1.00000000
7	150.107(3)	99.900(1)	(3,1)	(3,1)	1.00000000	1.00000000	1.00000000
8	150.109(1)	99.889(1)	(6,2)	(2,2)	1.00000000	1.00000000	0.99999999
10	150.110(1)	99.895(1)	(3,1)	(17,2)	1.00000000	1.00000000	0.99999999
11	150.111(1)	99.896(1)	(4,2)	(6,1)	0.99999999	0.99999995	0.99999997
12	150.110(1)	99.893(1)	(2,2)	(4,3)	1.00000000	1.00000000	1.00000000
13	150.111(3)	99.894(1)	(4,2)	(12,1)	1.00000000	1.00000000	1.00000000
14	150.107(1)	99.888(1)	(6,2)	(4,1)	0.99999999	1.00000000	0.99999999
15	150.104(3)	99.900(1)	(7,1)	(1,1)	1.00000000	1.00000000	1.00000000
16	150.079(3)	99.898(1)	(4,1)	(3,2)	1.00000000	1.00000000	1.00000000
17	150.109(3)	99.899(1)	(17,1)	(8,1)	1.00000000	1.00000000	1.00000000
18	150.109(1)	99.894(1)	(9,2)	(9,2)	1.00000000	0.99999999	0.99999998
19	150.110(1)	99.895(1)	(5,1)	(3,1)	1.00000000	1.00000000	1.00000000
20	150.097(3)	99.895(1)	(2,2)	(6,1)	1.00000000	1.00000000	1.00000000
21	150.106(1)	99.892(1)	(5,1)	(2,1)	1.00000000	1.00000000	1.00000000
22	150.111(1)	99.892(1)	(1,1)	(6,1)	1.00000000	1.00000000	0.99999999
23	150.106(3)	99.899(1)	(20,3)	(9,1)	1.00000000	1.00000000	1.00000000
24	150.107(3)	99.900(1)	(3,1)	(5,1)	1.00000000	1.00000000	1.00000000
25	150.105(3)	99.899(1)	(8,2)	(2,2)	1.00000000	1.00000000	1.00000000
26	150.112(1)	99.897(1)	(8,2)	(5,1)	0.99999998	1.00000000	0.99999998

Table 3.2: Data relative to the 25 Inermet cylinders employed in the experiment. Orthogonality values (face 1 and 2) and tilt are obtained respectively by scalar product of base and lateral tilt versor with the vertical. Cylinder #26 is used as backup.

Cylinder	Mass (g)	Density ($\mathrm{g/cm^3}$)	Cylinder	Mass (g)	Density ($\mathrm{kg/m^3}$)
1	21489.242(9)	18.2652(5)	15	21488.560(9)	18.2640(7)
2	21487.390(8)	18.2623(7)	16	21486.496(8)	18.2661(7)
3	21489.341(9)	18.2639(5)	17	21485.497(8)	18.2610(7)
4	21488.659(8)	18.2644(7)	18	21483.065(8)	18.2611(5)
5	21486.622 (8)	18.2650(5)	19	21484.461(8)	18.2615(5)
6	21479.993(8)	18.2591(7)	20	21481.455(8)	18.2607(7)
7	21485.213(8)	18.2607(7)	21	21487.795(10)	18.2659(5)
8	21480.708(9)	18.2607(5)	22	21486.364(9)	18.2641(5)
10	21483.320(8)	18.2605(5)	23	21487.273(8)	18.2632(7)
11	21483.877(8)	18.2608(5)	24	21488.460(9)	18.2636(7)
12	21486.148(8)	18.2639(5)	25	21489.228(8)	18.2646(7)
13	21489.851(8)	18.2664(7)	26	21485.723(8)	18.2618(5)
14	21484.936(8)	18.2649(5)			

Table 3.3: Masses and calculated densities of 25 tungsten cylinders.

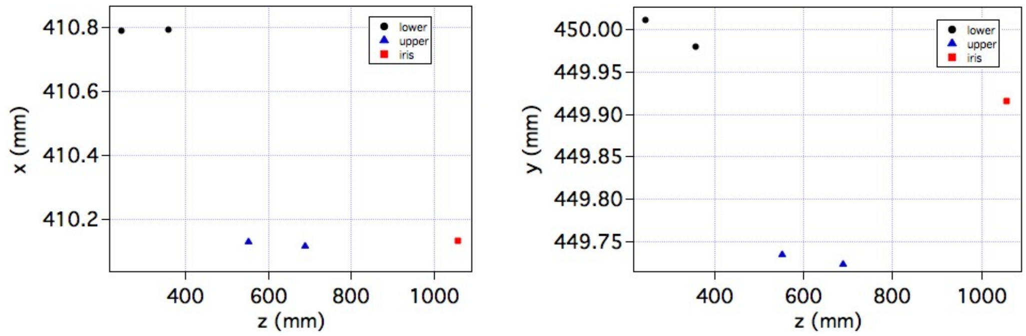

Figure 3.14: Left: x-z plot of source masses center in C and F configuration and reference iris; Right: y-z plot of source masses center in C and F configuration and reference iris.

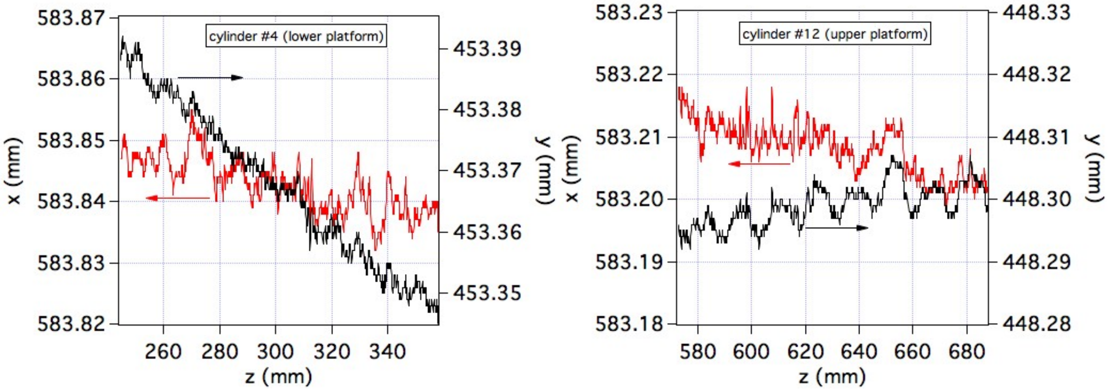

Figure 3.15: Left: positions of the cylinder #4 during the movement of the lower platform; Right: positions of the cylinder #12 during the movement of the upper platform

It is fairly evident that the centers of lower and upper sets are not laying on the same vertical axis, with an offset of about 0.70 mm along x and 0.25 mm along y while Raman beams seem to be closer to the upper masses. Induced systematic shift on G has to be carefully evaluated.

Dynamic tests were also performed on both holding platforms following the movement of cylinder #4 in the lower one and cylinder #12 in the upper one. Results are reported in figure 3.15

Plots show different behaviors of the holding platforms. In particular we can observe how the lower one moves by more than 40 μm along y when the upper moves by less than 10 μm in the opposite direction, i.e. the elevator motors are not perfectly parallel. In fact this effect cannot be due to support platform tilt and/or deformations, since in this case we would expect the same x, y shift for both platforms.

Chapter 4

Experimental procedure

In this chapter we are going to provide a full description of the experimental sequence chosen to realize gravity measurements using cold atoms. Single elements of the experiment will be described in detail, starting from the three-dimensional MOT, mentioning the velocity selection and state preparation and finishing with the detection section. We will place particular emphasis on recent improvements to increase the gradiometer sensitivity. At the end of the chapter a brief description of the signal extraction procedure will be also given.

4.1 Atomic fountain

For the gradiometer realization it is essential to achieve a condition in which two clouds of cold atoms ($\sim$2 μK) are placed at relative distance of $\sim$30 cm during their path into the interferometric region. It is also relevant that both samples have a high atom number (10^8- 10^9) in order to obtain a good signal to noise ratio. In the following, we will present the various tools used to obtain this not trivial condition.

4.1.1 3D-MOT

Atoms coming from our high flux source (2D-MOT) must be properly collected and cooled. One of the most popular methods for doing this is the 3D magneto-optical trap (3D-MOT) [49, 70]. Now let us give a brief explanation of the trapping and cooling principles underlying the functioning of these devices. Consider a 1D system in which a ^{87}Rb atom is moving with a certain velocity v along two counter-propagating laser beams slightly red detuned from the transition. Due to the Doppler effect the atom has a higher probability of absorbing photons from the beam towards which it is moving. After absorption the photon momentum is transferred to the atom, then it spontaneously re-emits the photon in a random direction and consequently recoils. After several iteration of this process the net effect is a viscous force. Now let us suppose to have opposite circular polarizations (σ^+/σ^-) on each beam respectively and add a magnetic field gradient along the direction we are considering. Taking into account the ^{87}Rb Zeeman level structure it is possible to demonstrate that under this condition a confining potential having the central point where the magnetic field is zero is created. Extending this principle in the three orthogonal spatial directions the 3D-MOT is obtained as shown in figure 4.1.

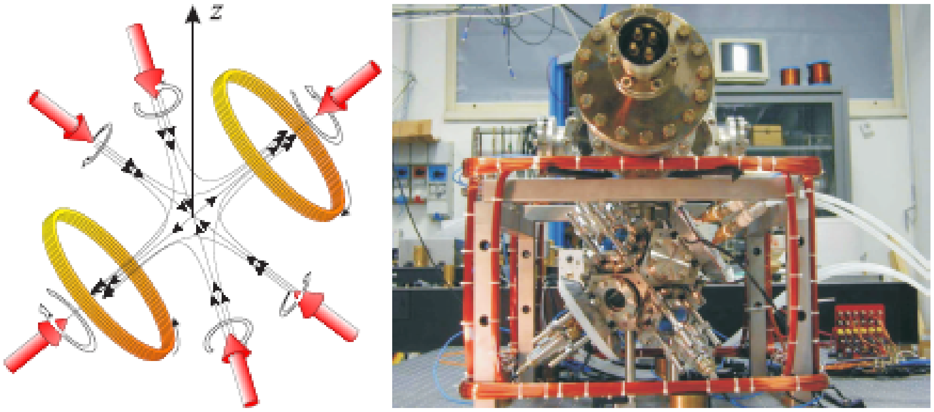

Figure 4.1: Left: schematic drawing of the 3D-MOT in (1-1-1) configuration. Red and white arrows indicate the six light beams and their polarization respectively. The two coils producing the quadrupole field are shown together with some corresponding magnetic field lines (black arrows). Right: Photo of the realized MOT.

Our 3D-MOT is composed of 3 pairs of counter-propagating beams orthogonally arranged and symmetrically tilted from the vertical direction (1-1-1 configuration, see figure 4.1) in order to leave free the optical access for the Raman beams in the z direction and to ensure proper application of radiation force for the launch. Frequency can be independently controlled for the three upper beams and for the three lower ones. Other relevant parameters are beam waist (w_s =11 mm) and beam intensity I = 25 mW ($\sim$15 I_S). During the trapping phase they are all detuned by -3Γ from $\nu_{2\to3}$.

The quadrupole magnetic field is produced by a pair of coaxial coils with opposite currents (anti-Helmotz configuration) and the zero field point is placed at the center of the beam crossing region. The 50 turns coils have a mean radius of 7 cm and are separated by 16 cm (see figure 4.1). With a current of 25 A they produce an axial magnetic field gradient of 8.3 G/cm. The magnetic gradient value along the radial plane crossing the center is one half of the axial one.

4.1.2 Launch

After collecting the desired amount of atoms (typically 5×10^8), it is necessary to proceed with additional cooling and to launch it upwards to the desired height. The launching mechanism is based on moving optical molasses [50].

As described above in case of 6 beams at the same frequency atoms are cooled and trapped, i.e. are slowed down to a zero mean velocity with respect to the laboratory reference frame. Now let suppose to apply a relative detuning between the three upwards and the three downwards propagating beams. In this case atoms are still cooled, but the mean velocity will be different from zero. In fact the equilibrium of mechanical forces (radiation pressure) is reached only when in the atoms reference system all beams have the same frequency. This condition can be achieved when the atoms mean velocity is such as to compensate the introduced frequency shift by Doppler effect.

In our apparatus this is realized shifting the upwards propagating beams by $+\delta$ and the down-

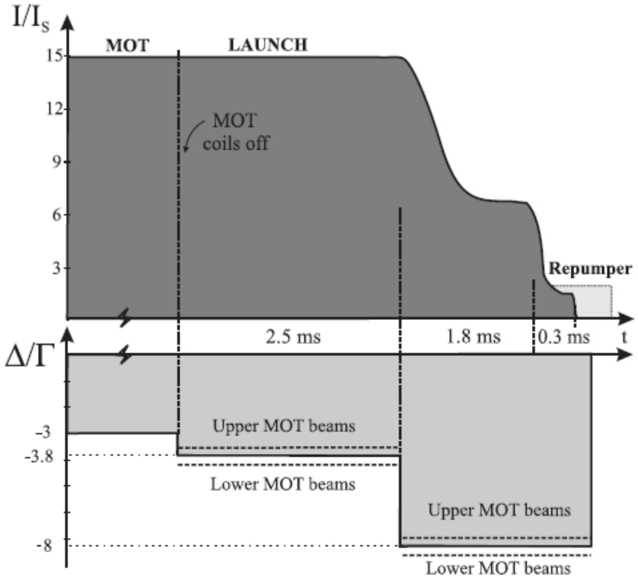

Figure 4.2: Intensity and frequency evolution of cooling beams during the launch phase. Dashed lines describe the different frequencies for the downwards and upwards propagating beams. The time axis is not to scale [43].

wards propagating ones by $-\delta$. Since the wave vector $\mathbf{k}$ of each beam forms with the vertical an angle ξ ($\cos\xi = 1/\sqrt{3}$), the atomic cloud can be launched with an initial vertical velocity v_z given by

$$v_z = \frac{\delta}{k\cos(\xi)} \tag{4.1}$$

corresponding roughly to a v_z of 1.35 m/s for each MHz of detuning δ.

In figure 4.2 the sequence used in the experiment to launch cold atoms in the fountain is shown. The launch starts when the quadrupole magnetic field is rapidly (200 μs) switched off. At the same time the beams detuning Δ is increased to -3.8Γ and the differential detuning δ is added. In this way atoms are subjected to a vertical acceleration and cooled thanks to the subdoppler cooling mechanism [50]. After 2.5 ms the detuning is further increased to -8Γ and the beams intensity I is decreased, first to a single beam intensity of $6.6 I_S$ for 1.8 ms, then to $2 I_S$. In order to avoid too abrupt changes of intensity and let the atoms follow adiabatically the change, this transition has been smoothen using an RC filter with $\tau = 500$ μs acting on the control signal of the RF amplitude sent to the cooling AOMs (see section 3.1.4). Using these precautions we are confident that the final temperature will scale roughly with I/Δ. At the end the cooling laser is completely turned off and the atomic sample is illuminated only by the repumping light for another 3 ms, in order to pump all the atoms in the $|F = 2\rangle$ state. An experimental efficiency to prepare atoms in the $F = 2$ state of more than 99.9% was observed. The final temperature of the cloud is 2 μK.

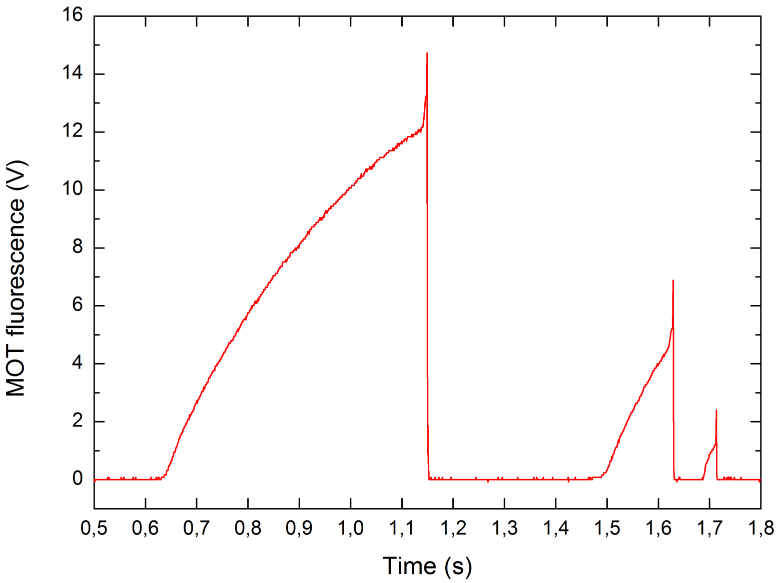

Figure 4.3: 3D-MOT fluorescence signal during a juggling sequence.

4.1.3 Juggling

For a gradiometer it is necessary to obtain two atomic clouds having the same falling speed and a vertical separation of 30∼40 cm. As a consequence the second cloud must be launched within a very short time (∼100 ms) after the first one. Even with the introduction of the 2D-MOT module the effective loading time (40 ms) is not enough to achieve a satisfactory atom number. For this reason we chose to increase the experiment cycle rate by a factor ~ 2 using the juggling technique [35, 86] in order to reach a good atom number in both the clouds. This technique works as follows: a cloud of atoms is loaded and launched upwards; during its flight a second cloud is loaded; when the first cloud is falling towards the trapping region, the second cloud is launched and the falling one quickly and efficiently recaptured. In figure 4.3 the fluorescence signal detected in the trap chamber during a juggling sequence is shown.

A cloud of $\sim 10^9$ atoms is loaded in 0.5 s and launched up to 31 cm for a total flight time of ~ 0.5 s. About 350 ms later the MOT is turned on again to perform the loading of the second cloud. Such long time is needed to reduce the heating of the first cloud induced by the scattered light during the loading of the second one. Once the first cloud is approaching the trapping region the new cloud is launched up to 91 cm. After 50 ms a fraction of the first cloud is recaptured, cooled and relaunched up to 60 cm within few ms. At this point the sequence is complete and in the interferometric tube we have two atomic samples ready for the velocity selection and state preparation.

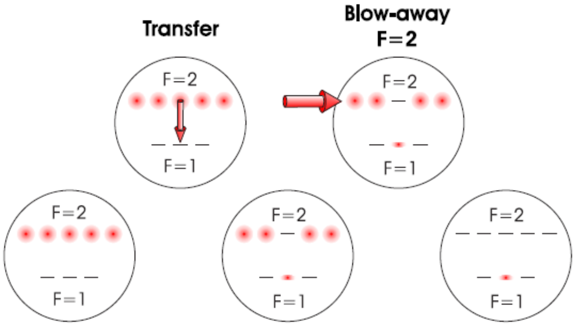

Figure 4.4: Scheme of the state preparation sequence previously used in the experiment. Zeeman sublevels of both hyperfine ^{87}Rb states are shown. The horizontal and vertical spatial distribution are also graphically represented.

4.2 State preparation

At the end of the launch procedure atoms are distributed in different velocity classes and internal states. In particular different velocities imply spatial spread, thus different Doppler effect and different gravitational interaction force with surrounding masses. On the other hand atoms in different Zeeman sublevels interact in different ways with a magnetic field. To avoid these issues it is mandatory to put atoms in the less sensitive magnetic sublevel (in our case $|F, m_F\rangle = |1, 0\rangle$) and then select a certain velocity class. Recently the state preparation procedure has been improved in order to solve some problems related to the signal shape.

4.2.1 Single pulse velocity selection

Figure 4.4 shows the state preparation sequence previously implemented in the experiment.

Almost all the atoms in the thermal cloud are pumped in the F = 2 state. The small atoms amount in F = 1 is negligible and no additional treatment is required. A velocity selective Raman π pulse (τ =48 μs, square shaped) is then vertically applied. The laser beams frequency difference is resonant with the transition $|F = 2, m_F = 0\rangle \rightarrow |F = 1, m_F = 0\rangle$ and therefore a selected velocity class is transferred into the$|F = 1, m_F = 0\rangle$. Such operation is possible only in presence of a vertical magnetic field that properly splits the magnetic sublevels. In our case, it is provided by a long coil wrapped around the interferometer tube (see section 3.2.2). The vertical velocity spread is limited by the Raman pulse duration and according to our parameter corresponds to a temperature of 80 nK. Along the horizontal directions the velocity distribution remains the thermal one. The remaining atoms in the $|F = 2, m_F = 0\rangle$ state are blown away by means of a 5 ms pulse (slightly divergent, circularly polarized) tuned to $\nu_{2\rightarrow3}$. In figure 4.5 a typical state selective fluorescence signal of an atomic sample crossing the detection region is reported (black line), together with our best fitting models (red and blue lines). From the fit residuals it is evident how the presence of a wide background makes critical the signal evaluation. Moreover it is very difficult to recognize which fraction of the atoms will be involved in the interferometer sequence and this can be source of systematic errors.

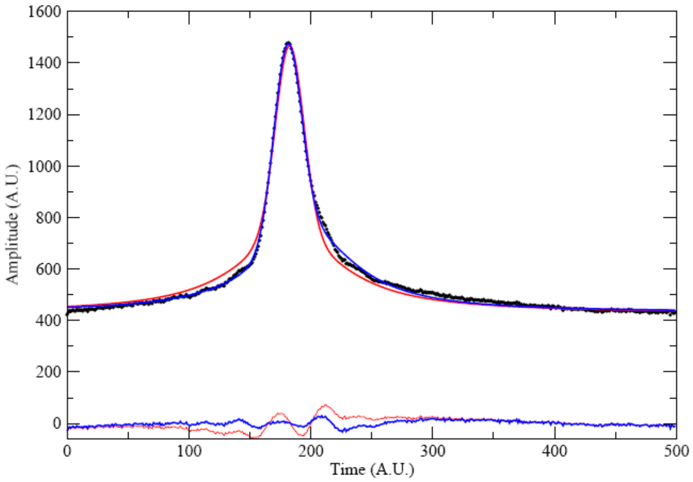

Figure 4.5: Typical fluorescence signal after a single pulse velocity selection (black curve). Two Gaussian + Lorentzian (G(x) + F(x)) fits are depicted: G(x) and L(x) having the same center (red curve) and leaving centers distance as a free fit parameter (blue curve) . On the bottom fit residuals are also reported.

Such background can be explained in term of off-resonance scattering originating from the thermal cloud. Indeed, a certain fraction of the interrogated atoms (inversely proportional to the Raman detuning), instead to perform the two-photon stimulated Raman transition, can absorb a photon and re-emit it spontaneously. As a consequence these atoms, being not velocity selected, will constitute a thermal background on the detected signal.

One method to fix this problem is a Zeeman substate preselection using a microwave pulse [3]. Nevertheless the geometric constrains of the experiment preclude the possibility to perform it simultaneously and with the same efficiency on both clouds. Consequently, a new solution has been implemented.

4.2.2 Triple pulse velocity selection

Figure 4.6 shows the new state preparation sequence of the experiment. The first steps are in common with old sequence. Therefore we will start from the single pulse velocity selection final state.

After 5 ms from the F = 2 blow away pulse, a second π pulse is then applied on the atoms previously selected in order to transfer the highest percentage in F = 2 state. Almost all the atoms forming the thermal background are left in F = 1 state. After 5 ms a 10 ms light pulse, resonant with the transition $F = 1 \rightarrow F' = 0$, is sent along the interferometer tube to blow away F = 1 atoms. The efficiency of this process is strongly limited ($\sim 70\%$) by pumping into dark states in F = 1. However, optimizing the degrees of freedom available (polarization and beam direction), an almost total suppression of the thermal pedestal has been achieved on both clouds. Finally the sequence is concluded bringing back the atomic sample in F = 1 (now background free) by a third

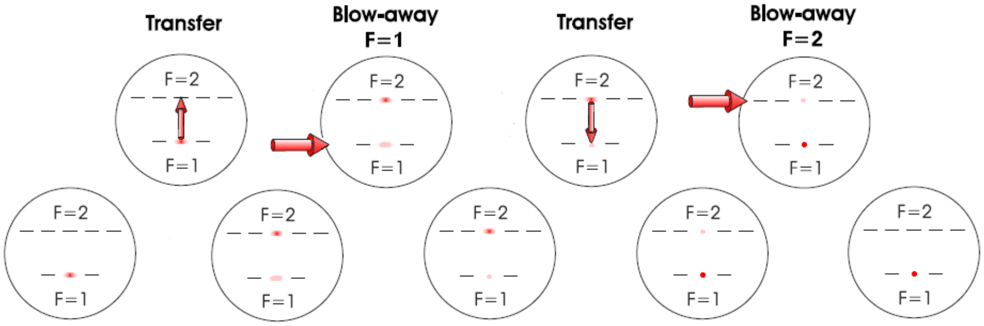

Figure 4.6: Schematic representation of the triple pulse velocity selection sequence. The initial state coincides with the final one of the previous sequence.

Raman pulse and then efficiently cleaning the F = 2 channel with a further F = 2 blow-away pulse. All these operations are performed within 20 ms. In figure 4.7 the resulting fluorescence signal is reported together with the best fitting function. All the Raman pulses are square shaped and doppler compensated in frequency.

Now the thermal pedestal in the F = 1 peaks has completely disappeared and the residuals do not show any structure. Moreover the same fitting model is also effective for F = 2 peaks, symmetrizing in this way the two channels fitting procedure. The drawback for this shape achievement lies in a 40% atoms loss due to the two additional Raman π pulses. However, this is compensated by a larger contrast of interference fringes. As a result, the sensitivity of gravity gradient measurement is improved with respect to the use of single pulse velocity selection (see section 5.1.3).

4.3 Atom interferometer

After the state preparation, both atomic samples are ready for the interferometer sequence. Three Raman pulses ($\frac{\pi}{2}$, π, $\frac{\pi}{2}$) temporally separeted by a time T are sent on both the clouds for a simultaneous interrogation. We make use of the lin⊥lin beam-configuration (see section 2.1.2) using a $\lambda/4$ plate + retro-reflecting mirror placed on the top of the interferometric tube. The horizontality of the retro-reflecting mirror has been adjusted within 100 μrad using a tiltmeter (Applied Geomechanics 7551129). Due to the presence of the vertical bias field parallel to $\mathbf{k_{eff}}$, only transitions with $\Delta m_F = 0$ are possible because the combinations of the ClebschGordan coefficients and doppler effect let other possibilities vanish. As a consequence, only $|F = 2, m_F = 0\rangle$ and $|F = 1, m_F = 0\rangle$ states contribute to the signal.

As described in section 3.1.5 the Raman beam frequency difference is swept with a phase-continuous linear frequency ramp for Doppler shift compensation. Depending on the ramp sign only one beams pair is in resonance with the atomic frequency in its reference frame. The resonance condition of both pairs occurs only when atoms are at rest, i.e. at the apogee of the ballistic flight. Applying a Raman pulse in such situation, half of the atoms would exchange the wrong momentum and their contribution to the signal would be lost. On the other hand placing the central π pulse at the turning point implies a perfect symmetry between the interferometer parts, eliminating spatial effects like magnetic field gradients. To solve this issue we did a compromise between this two

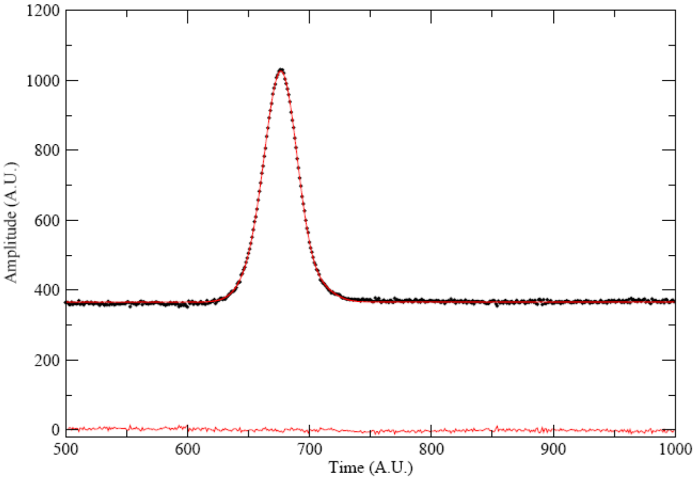

Figure 4.7: Typical fluorescence signal after a triple pulse velocity selection (black curve) together with a Gaussian×4° order polynomial (G(x)×P(x)) fitting function (red curve). P(x) is used to model the finite response speed of the detection photodiode. On the bottom fit's residuals are also reported.

requirements, sending the π pulse close as much as possible to the inversion point but far enough so that atoms have a velocity component sufficient to neglect absorption from the off-resonant pair of Raman beams. So far we use $(t_\pi - t_{apogee}) = 5$ ms corresponding to a vertical velocity of 49 mm/s. Considering typical free evolution time value (T = 160 ms) the uncompensated path is 16 mm on a total of about 125 mm.

The phase shift introduced by the gravity (ϕ_0), in absence of others effects, is constant, therefore a controlled phase shift ϕ_L is introduced between the π pulse and the last $\pi/2$ pulse in order to scan the interferometric fringes when it is necessary. Experimentally this can be done by stepping the phase of our 6.8 GHz synthesizer used for Raman phase-frequency lock (see section 3.1.5). Figure 4.8 shows an interferometer fringe at T = 10 ms on a single cloud, obtained varying ϕ_L in 5° steps.

4.4 Detection

The acceleration impressed on the atoms as well as any other dephasing effect can be obtained by measuring the relative population between the two hyperfine states $|F=1\rangle$ and $|F=2\rangle$. For that purpose on their way back from the interferometer region, the atoms pass through the detection chamber where they will be properly revealed. The detection is realized by fluorescence excitation using three light sheets as shown in figure 4.9.

The atoms first pass a 15 mm broad and 4 mm high circularly polarized beam, having an intensity of $3.3 I_S$ and in resonance with the transition $\nu_{2\to3}$ to probe the $|F=2\rangle$ state population. The upper part of this beam (first 2 mm in height) is retro-reflected while the lower part is blocked in order to blow away the probed atoms. The emitted fluorescence is collected on a photodiode by a f = 50 mm, 2" diameter lens placed at a distance of 130 mm from the center image ($\Omega/4\pi \simeq 10^{-2}$). Only

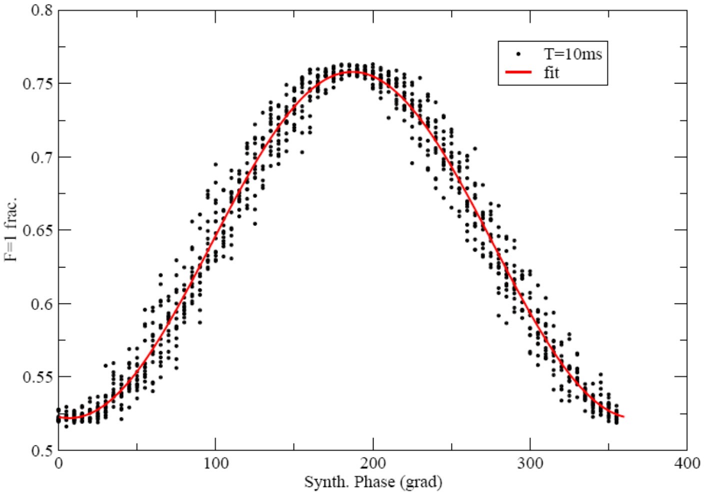

Figure 4.8: Interferometer fringes at T = 10 ms. F = 1 state normalized population is plotted against the external phase ϕ_L introduced by the synthesizer. Sinusoidal fit (solid line) is also shown.

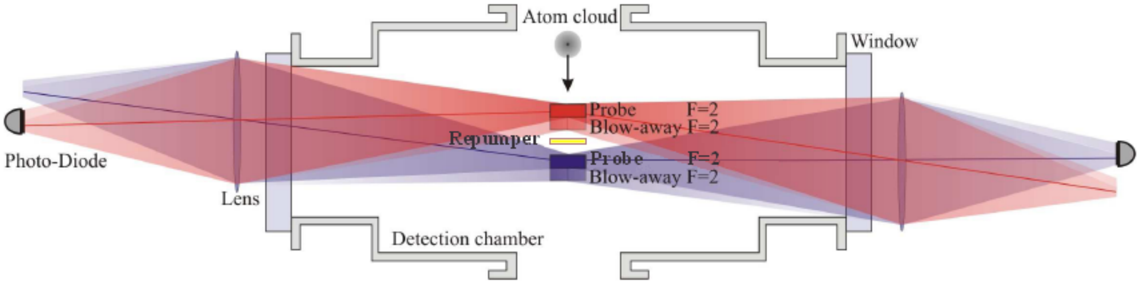

Figure 4.9: Scheme of the detection system adopted in the experiment.

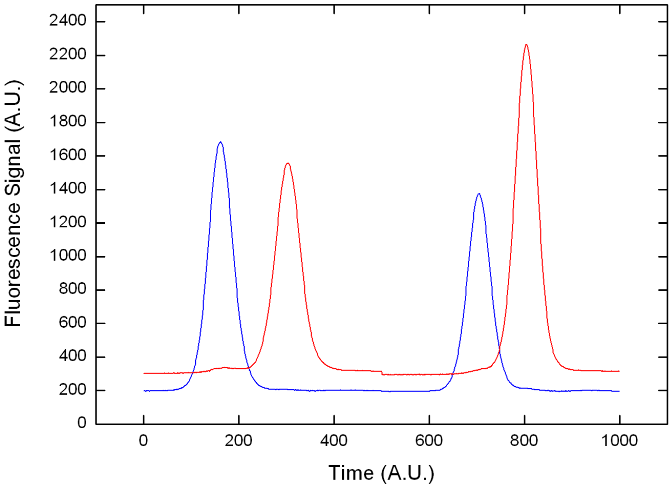

Figure 4.10: Fluorescence signal of the atom clouds passing the detection region. Red and blue traces are related to different detection channels ($F = 1$ and $F = 2$ respectively). The first two peaks correspond to the lower cloud population. Then the same for the upper cloud. Crosstalk peaks between channels are also visible.

the atoms in $|F = 1\rangle$ will continue to the next light sheet which has the same width but narrower in height (1 mm). Here a low intensity (200 μW/cm^2) beam is tuned on the $\nu_{1\to 2}$ transition to pump efficiently the atoms to $|F = 2\rangle$ state. Finally the atoms encounter the third light sheet identical to the first, in order to achieve the maximum symmetry between channels. Also the fluorescence light is collected using an analogous scheme on a second photodiode. A horizontal magnetic field along the detection beams is provided with external coils to well define the quantization axis. The geometry is chose to gradually change the field from vertical (in the interferometer region) to horizontal direction, in order to allow the atoms to adiabatically follow such transition.

We use two Hamamatsu S7510 photodiodes (active area 11×6 mm) for detection, protected by 780 nm interference filters from the background light. A 1 GΩ transimpedance amplifier with an OPA627 converts the photodiode current into a voltage. The bandwidth is of the order of few kHz. To optimize the noise level we implemented a new scheme for the photodiode amplifier described in [58]. We reached a ultimate current noise level of 7 fA/$\sqrt{\text{Hz}}$ limited by the Johnson noise of the 1 GΩ resistor and the photodiode dark current.

In figure 4.10 an example of the atomic fluorescence signal is reported.

The peak area (A) can be linked to the number of atom (N) in a given state. Let us suppose to have an atom lying in a standing wave with a total intensity I and detuning Δ. The photon scattering rate is

$$R_{sc} = \frac{\Gamma}{2}\left(\frac{I/I_S}{1 + 4\triangle^2/\Gamma^2 + I/I_S}\right) \tag{4.2}$$

Taking into account the photon energy ($h\nu_{2\rightarrow 3}$), the total atom crossing time through the beam (τ), the total photodiode responsivity (η_{tot}) and the light collecting solid angle (Ω), we obtain the following relation between A and N:

$$A = N\frac{\Omega}{4\pi}R_{sc}\tau\eta_{tot}h\nu_{2\rightarrow 3} \tag{4.3}$$

According to our experimental parameter, typical fluorescence spectra show a number of atoms equal to a few parts in 10^5. This is translated into a quantum projection noise δN_q of $\sqrt{N} \simeq \sqrt{10^5} = 300-400$. Considering that the rms noise of our photodiode amplifier previously calculated corresponds to $\delta N_{ph} \sim 140 < \delta N_q$, we expect not to be limited by detection technical noise.

4.5 Signal analysis

The acquired fluorescence spectra (see figure 4.10) contain two peak pairs describing the hyperfine state populations of the two conjugate interferometers. As a first step we need to evaluate the peaks areas in order to calculate the relative state population. We chose to fit the signal using a G(x)×P(x) model, where G(x) is a Gaussian and P(x) is a 4° order polynomial, plus a background linear slope. P(x) is suitable for modeling the asymmetry induced by the finite photodiode bandwidth. The resulting peak area (A_F^z) is proportional to the number of atoms in the corresponding state (F = 1, 2) and cloud (z = up,dw), as shown in equation 4.3. So for each cloud the normalized populations are:

$$\begin{aligned} \eta_1^{up} &= \frac{A_1^{up}}{A_1^{up}+A_2^{up}} \qquad \eta_2^{up} = \frac{A_2^{up}}{A_1^{up}+A_2^{up}} \\ \eta_1^{dw} &= \frac{A_1^{dw}}{A_1^{dw}+A_2^{dw}} \qquad \eta_2^{dw} = \frac{A_2^{dw}}{A_1^{dw}+A_2^{dw}} \end{aligned} \tag{4.4}$$

In presence of an external phase scan, fringes can be obtained plotting η_F^z as a function of the applied phase during each launch sequence.

As a first attempt to measure the gravity gradient one may think to evaluate the phase shift difference by directly fitting with a sinusoid the fringes corresponding to the upper and lower interferometer. This operation is possible only if the phase noise is not too high. Our retro-reflecting mirror is not seismically isolated and therefore increasing the interferometer time T the fringes are rapidly washed out by noise as widely explained in section 2.2.3. In figure 4.11 a fringe at T = 30 ms is reported. It is evident how the seismic noise greatly reduces the sensitivity of the measurement and makes difficult the sinusoidal fit.

To take advantage of long interference time (T = 160 ms) another approach is required.

4.5.1 Elliptical Fit

During the interferometer sequence two spatially separated atomic clouds in free fall are simultaneously interrogated by the same Raman beams. As a consequence the mirror vibrations affect likewise the upper and the lower interferometer making them highly correlated. A complete noise

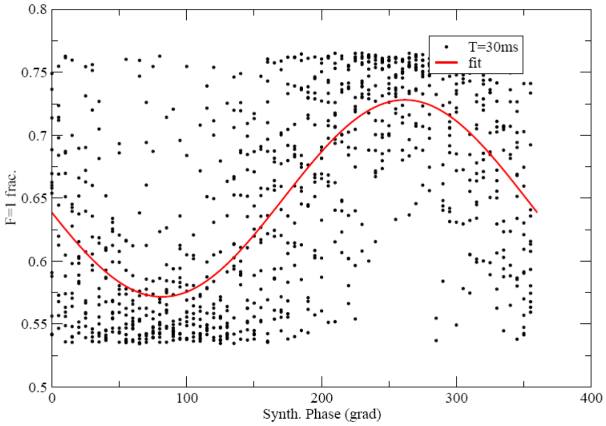

Figure 4.11: Interferometer fringes at T=30 ms. Sinusoidal fit (solid line) is also shown.

rejection can be achieved plotting the upper fringe versus the lower one. Lissajoux curves are obtained and the phase difference can be extracted by fitting the point distribution with an ellipse [36]. In fact the two fringes can be described with independent amplitudes (A and B) and vertical offsets (C and D) and with a relative phase difference Φ that is the parameter of our interest:

$$\begin{cases} x = & A\sin(\phi_x) + C \\ y = & B\sin(\phi_x + \Phi) + D \end{cases} \tag{4.5}$$

It can be demonstrated that this expression is the parametric form of an ellipse. To extract the differential phase of the gradiometer Φ (with of course the other 4 parameters) we use a least squares fitting algorithm on the experimental data. More details can be found in [43]. However this procedure is not immune to systematic errors and further analysis are required.

Noise induced bias

Ellipses can be affected by three different kinds of noise: amplitude noise (which affects A and B parameters), offset noise (which affects C and D) and phase noise (which affects directly Φ). Past comparisons [43] show that the amplitude noise was by far the dominant one in the experiment. Currently, after the recent improvements, further investigation could be necessary. The noise-produced effects on the estimated value for Φ have been evaluated performing different simulation in which the noise level and the ellipse angle were varied. We found a bias depending on both the noise and the ellipse angle itself; in particular, it is minimum for $\Phi \simeq \pi/2$. Thus it is convenient to add an external well controlled relative shift, in order to have a differential phase close to that value. An easy way to do that is to apply a localized uniform magnetic field pulse during the second part of the interferometer, only on one of the two atomic samples. As described in section 2.2.6, during the pulse the atomic energy levels are shifted by the second order Zeeman effect in different ways for the two clouds, adding an additional phase shift. Experimentally this can be realized sending a current pulse to some of the 10 short coils wrapped around the interferometer tube (see section 3.2.2), typically the three spatially closest to the interferometer to be shifted. In this way a shift proportional to the difference between the squares of the fields in the two interferometric regions $(B_{up}^2 - B_{dw}^2)$ is produced. More information regarding the magnetic field distribution in the interferometric region can be found in [43].

More sophisticated algorithms have been proposed to retrieve Φ with Bayesian estimators [51]. A Bayesian estimator has the advantage of being unbiased; however, it requires an *a priori* knowledge of the noise type.

Detection unbalance

Although particular effort has been put in making the detection section as symmetric as possible, efficiency differences between channels will be always present. Therefore a careful study of induced systematic effects on Φ is required.

In the ideal case an ellipse point (x,y) is determined by $x = n_1/(n_1 + n_2)$ where n_1 and n_2 are the numbers of atoms in the $|F = 1\rangle$ and $|F = 2\rangle$ states respectively in the first cloud. A similar expression holds for y where n_1 and n_2 are the number of atoms in the second cloud. Keeping in mind that $n_1 + n_2 = N$, it is possible to write the following expression:

$$x = \frac{N\cos^2 t}{(N\cos^2 t + N\sin^2 t)} = \cos^2 t \tag{4.6}$$

with t an auxiliary parameter so that $n_1 = N\cos^2 t$. In presence of a perfectly balanced detection we have $A_\lambda = \eta_\lambda n_\lambda$, $\lambda = (1, 2)$ with $\eta_1 = \eta_2$. Differently $(\eta_1 \neq \eta_2)$ the previous expression becomes:

$$x = \frac{\eta_1 N\cos^2 t}{(\eta_1 N\cos^2 t + \eta_2 N\sin^2 t)} = \frac{\cos^2 t}{1 + \epsilon\sin^2 t} \tag{4.7}$$

where $\epsilon = (\eta_2 - \eta_1)/\eta_1$ is the relative unbalance parameter. Expanding for $\epsilon \ll 1$ we obtain

$$x \simeq \cos^2 t(1 - \epsilon\sin^2 t) = \frac{1 + \cos 2t}{2} - \frac{\epsilon}{2}\sin^2 2t \tag{4.8}$$

Is possible to demonstrate that the latter term deforms the ellipse into an egg-shaped curve.

To evaluate the effect of the asymmetry in the determination of the angle Φ we used the followed procedure:

- ϵ has been varied from -0.3 to 0.3 in 0.05 steps.
- For each ϵ we generated 1000 ellipses of 24 points with $\Phi = 1.2$ rad, contrast 0.3 and additive Gaussian noise on x and y with σ =0.005. See figure 4.12.
- The 1000 ellipses have been fitted with our least squares fitting algorithm and the mean and standard deviation of the fitted angles have been determined. Then the exact Φ has been subtracted to evaluate the fit bias.
- The same analysis has been repeated for negligible noise σ =0.0001.

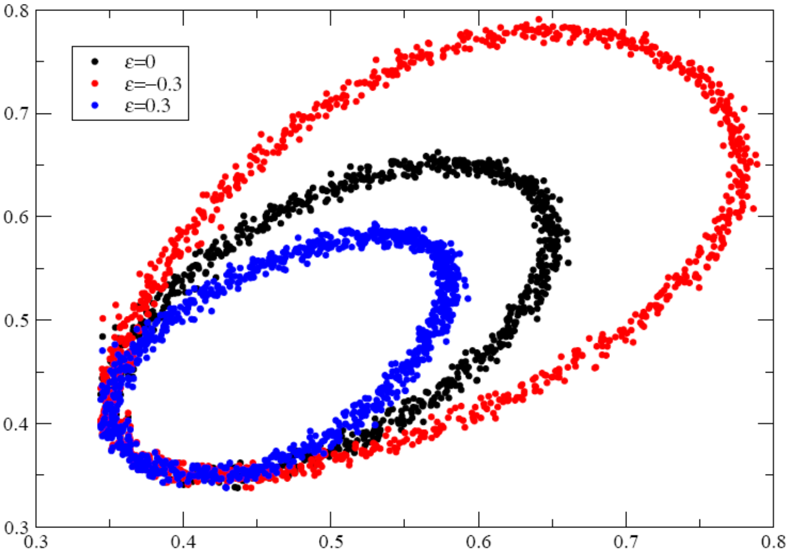

Figure 4.12: Three ellipses with $\epsilon = -0.3$, 0, 0.3 respectively, and additive Gaussian noise with σ =0.005.

Results are presented in figure 4.13.

Both data sets have been fitted with a 7th degree polynomial. Despite the different noise level the behavior is quite similar. In particular the systematic shift shows a minimum around $\epsilon = 0$. For very small ϵ a parabolic minimum is expected, so we also performed a new simulation in the range -0.05< ϵ <0.05 with a step of 0.01 in low noise condition. Fitting with $y = ax^2$ we found $a \simeq 0.1$ so, a systematic error below 100 μrad requires $|\epsilon| < 0.03$.

From this analysis we can conclude that an accurate measure of the detection efficiency (3% level) is needed. Alternatively we can analyze our experimental data by varying ϵ until Φ shows a minimum. With this method we can potentially determine the experimental detection efficiency mismatch and the unbiased angle value at once.

4.6 Experiment simulation

The main goal of the experiment is the measurement of G by atom interferometry. However what is really measured is the difference between the gradiometer phases Φ in the two source mass configurations (see figure 4.14). If all other experimental variables remain unchanged, such value is dependent only on the relative position between the atoms and the source masses. This connection can be quantitatively determined by a complete Montecarlo simulation of the experiment, leaving G as the only free parameter. Indeed, acting on it, is possible to tune the simulation output value until a match with the measured angle difference is obtained.

In this section various aspects relating the implemented computational solutions are reported. We will show also how the simulation can be a powerful tool to evaluate several systematic effects.

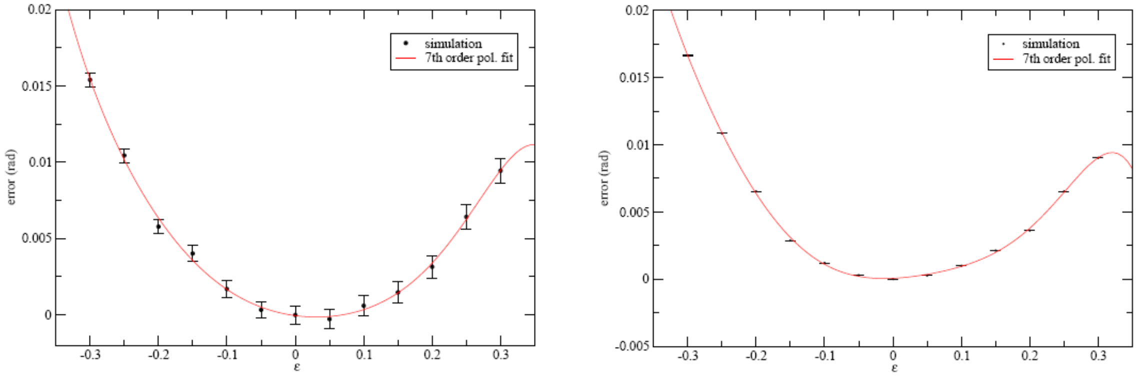

Figure 4.13: Left: results of the simulations for σ =0.005 together with a 7th degree polynomial fit (red line). Right: the same for σ =0.0001

4.6.1 Source mass modeling and phase shift calculation

Only the masses that are moved, i.e. cylinders and holding platforms, contribute to the final differential signal. We will now determine the gravitational potential induced by a cylinder and by a torus. Results will be used then to evaluate the phase difference accumulated by the two atomic ensembles in the two masses configurations. For a comprehensive discussion see [43].

Cylindrical shape

Let us consider a homogeneous cylinder of density ρ, radius R and height H, placed in the origin of a spherical coordinate system $O_{r\theta\phi}$. Now we want to calculate the gravitational potential generated in a generic point (r, θ, ϕ) outside the cylinder. From a computational point of view one of the most convenient method is the expansion in multipoles. In general the mass distribution contained within a sphere of radius R produces a gravitational potential outside the sphere that can be written as

$$U(r,\theta,\phi) = \sum_{l=0}^{\infty} \sum_{m=-l}^{l} \frac{4\pi}{2l+1} q_{lm} \frac{Y_{lm}(\theta,\phi)}{r^{l+1}} \tag{4.9}$$

with

$$q_{lm} = G \int_V Y^*_{lm}(\theta',\phi')(r')^l \rho(\mathbf{x}')d\mathbf{x}' \tag{4.10}$$

where $Y_{lm}(\theta, \phi)$ are the spherical harmonics. The axial symmetry allows only $m = 0$ terms and the symmetry for reflections on the horizontal plane passing through the center of mass makes the odd l terms vanish. Thus the last two equations simplify:

$$U(r,\theta) = \sum_{l=0}^{\infty} \frac{q_{2l,0} P_{2l}(\cos\theta)}{r^{2l+1}} \tag{4.11}$$

$$q_{2l,0} = G \int_V P_{2l}(\cos\theta)(r')^{2l}\rho(\mathbf{x}')d\mathbf{x}' \tag{4.12}$$

where $P_{2l}(\cos\theta)$ are the Legendre polynomials. Finally, specializing to our case (homogeneous cylindric mass distribution with mass M, height H and radius R), we obtain

$$U(r,\theta) = -\frac{GM}{R}\sum_{l=0}^{\infty}\beta^{2l+1}Q_l(\alpha^2)P_{2l}(\cos\theta) \tag{4.13}$$

where α and β are the dimensionless coefficients expressed by

$$\alpha = \frac{H}{2R} \text{ and } \beta = \frac{R}{r} \tag{4.14}$$

and $Q_l(\alpha^2)$ are polynomials expressed by

$$Q_l(\alpha^2) = \int_{-1}^{1}\int_0^1 P_{2l}(\cos\theta')(v'^2 + (\alpha u')^2)^l v' dv' du' \tag{4.15}$$

with

$$u' = \frac{2z}{H}\; v' = \frac{r'}{R} \text{ and } \cos\theta' = \frac{\alpha u'}{\sqrt{v'^2 + (\alpha u')^2}} \tag{4.16}$$

The series 4.13 converges the faster the smaller are α and β. Our closest cylinders lie at distance $r = 2R$ from the atoms, therefore β is fixed to 0.5, while α is 1.5. As a consequence, a relative error below 10^{-5} corresponds to an expansion up to $2l = 40$. A trick to reduce the expansion terms and save computational time is to divide each cylinder in two halves. In this way α becomes 0.75 and a truncation of the series at $2l = 10$ is sufficient to compute the potential with at least 6 digits accuracy.

Toroidal shape

The platforms holding the masses can be decomposed into several tori with rectangular section. They must be taken into account in the vertical acceleration determination. To this purpose let us consider a torus with internal radius R_{int}, external one R_{ext} and height H, lying on the xy plane symmetrically around the z axis. The symmetry of the system suggests to use cylindrical coordinates. The multipole expansion is not suitable in this case because our probe masses (atoms) are within the sphere that contains the source mass distribution. Therefore we will solve the problem in a more direct way. A point-like mass in (r, z) experiences the potential

$$U(r,z) = \int_0^H \int_{R_{Int}}^{R_{Ext}} \int_0^{2\pi} \frac{G\rho r' d\phi dr' dz'}{\sqrt{(z'-z)^2 + (r')^2 + r^2 - 2rr'\cos\phi'}} \tag{4.17}$$

Choosing the expansion parameter (that is expected to be much smaller than 1)

$$\eta = \frac{r}{R_{int}} \tag{4.18}$$

and introducing the following dimensionless variables

$$u' = \frac{r'}{R_{int}} \text{ and } \upsilon' = \frac{z'}{R_{int}} \tag{4.19}$$

and the parameters

$$\alpha = \frac{R_{ext}}{R_{int}} \text{ and } \beta = \frac{H}{R_{int}} \tag{4.20}$$

we get

$$U(\eta, \upsilon) = G\rho R_{int}^2 \int_0^\beta \int_1^\alpha \int_0^{2\pi} \frac{u' d\phi' du' d\upsilon'}{\sqrt{(\upsilon' - \upsilon)^2 + (u')^2 + \eta^2 - 2\eta u' \cos\phi'}} \tag{4.21}$$

The integrand can be expanded in series up to the second order in η, leading after integration in $d\phi'$and du to

$$U(\eta, \upsilon) = G\rho R_{int}^2 \int_0^\beta I(\eta, \upsilon') d\upsilon' \tag{4.22}$$

with

$$I(\eta, \upsilon) = 2\pi \left(\sqrt{\alpha^2 + (\upsilon' - \upsilon)^2} - \sqrt{1 + (\upsilon' - \upsilon)^2} \right) + \frac{\pi\eta^2}{2} \left(\frac{1}{|1 + (\upsilon' - \upsilon)^2|^{3/2}} - \frac{\alpha^2}{|\alpha^2 + (\upsilon' - \upsilon)^2|^{3/2}} \right) \tag{4.23}$$

This integral can be analytically solved. The potential and the acceleration components along the symmetry axis can be easily determined by choosing $\eta = 0$.

Determination of the interferometer phase

Also for the phase shift evaluation a perturbative technique has been employed. We chose to follow the Bordè approach (see section 2.2.5), since it is particularly simple to implement in a simulation code and thus suitable for our purpose.

We start from an unperturbed system with only uniform gravity g, considering, for sake of simplicity, an unidimensional motion along the symmetry axis z. The potential ($\hat{V}(z) = mgz$) determines the unperturbed atomic trajectory $\tilde{z}(t)$. We aim to calculate the new trajectory $z(t) = \tilde{z}(t) + \delta z$ induced by a perturbative potential $U(z)$, containing the source masses and the Earth gravity gradient contributions. If the total energy of the system is

$$E = \frac{1}{2} m\upsilon(z)^2 + V(z) + U(z) \tag{4.24}$$

we have

$$\frac{1}{\upsilon(z)} = \frac{1}{\sqrt{\frac{2}{m}\left[E - V(z) - U(z)\right]}} \tag{4.25}$$

An integration in dz yields to an expression for $t(z)$

$$t(z) = \int_{z_0}^{z} \frac{dz'}{\upsilon(z')} = \int_{z_0}^{\tilde{z}+\delta z} \frac{dz'}{\sqrt{\frac{2}{m}\left[E - V(z') - U(z')\right]}} = \mathcal{F}(\tilde{z} + \delta z) \tag{4.26}$$

We expect $\delta z \ll \tilde{z}$, so we can expand the former equation to have

$$t = \mathcal{F}(\tilde{z}) + \delta z \mathcal{F}'(\tilde{z}) = \mathcal{F}(\tilde{z}) + \delta z \frac{1}{\upsilon(\tilde{z})} \tag{4.27}$$

and thus

$$\delta z = \upsilon(\tilde{z}) \left[t - \mathcal{F}(\tilde{z})\right] \tag{4.28}$$

This expression can be written only in terms of t and therefore numerically calculated. This procedure is particularly convenient since we are not interested in estimating two large quantities themselves (t and $\mathcal{F}(\tilde{z})$) but only in their difference, reducing in this way numerical stability problems.

The accumulated phase shift ϕ_G in one interferometer due to $U(z)$ is then simply estimated by

$$\phi_G = k_{eff} \left[\delta z(2T) - 2\delta z(T)\right] \tag{4.29}$$

The validity of the simulation has been checked by comparison with the analytical solution in case of the gravity gradient only (see equation 2.83). The calculated phase shift is consistent with the expected one within 10^{-6} rad.

4.6.2 Systematic effects

The simulation can be also utilized both to define the best experimental configuration in order to minimize systematic shifts and to evaluate residual effects due to our not perfect knowledge of the system geometry. In the following we will analyze these aspects distinguishing between atoms position and source masses contributions.

Atomic sample

Atoms and source masses vertical positions are crucial parameters in our measurement. Since it is technically much easier with our apparatus to monitor with great accuracy the source masses position (see section 3.4.2) with respect to the cloud trajectory, it is reasonable to choose a configuration that minimize the cloud position sensitivity. The adopted procedure is described below.

For sake of clarity, figure 4.14 shows the experiment geometry together with the parameters that we are going to determine.

- In C configuration the two sets of masses are put as close as possible (H_C^{up} and $H_C^{dw}$are setted). This is the way to create the minimum differential vertical acceleration.
- Using these input parameters the experiment is simulated for different values of the vertical atomic positions z_0^{dw} and z_0^{up} at the beginning of the interferometer sequence. The values Z_0^{dw} and Z_0^{up} for which the differential phase shift Φ_C has a stationary point are chosen.

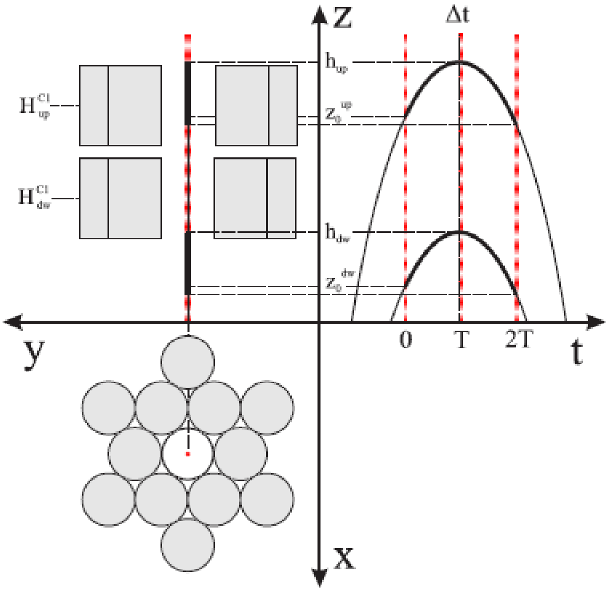

Figure 4.14: Scheme of the experiment setup in C . Atoms and masses are shown from a top view (x-y plane), from a side view (y-z view) and in the time domain (z-t graph). H_C^{up} and H_C^{dw} are the heights of the lower and upper cylinders center of mass, whereas h^{dw} and h^{up} are the ballistic turning points for the two atomic samples. z_0^{dw} and z_0^{up} label the atomic vertical position when the first interferometer pulse occurs. The asymmetry of the interferometer in the time domain, introduced by the delay Δt between the inversion time and the time of the central π pulse, is also shown [43].

- Finally we determine the F masses configuration (H_F^{up} and H_F^{dw}) so that the phase gradient with respect to the atomic initial positions vanishes:

$$\left\{\begin{array}{ll} \frac{\partial}{\partial z^{dw}}\Phi(z^{dw}, z^{up}, H_F^{up}, H_F^{dw})\big|_{z^{dw}=z_0^{dw}, z^{up}=z_0^{up}} & = 0 \\ \frac{\partial}{\partial z^{up}}\Phi(z^{dw}, z^{up}, H_F^{up}, H_F^{dw})\big|_{z^{dw}=z_0^{dw}, z^{up}=z_0^{up}} & = 0 \end{array}\right. \tag{4.30}$$

Figure 4.15 shows the vertical acceleration profiles corresponding to a certain parameter set selected in this fashion.

As a result a 0.5 mm error in z_0 leads to a relative error on G of 1.2×10^{-5}.

It is worth noting that the trajectories of the upper and lower interferometers lie around two flat regions, i.e. where the Earth gravity gradient is compensated by our source masses. This can only be obtained with high density source masses.

Regarding the horizontal atoms positioning, figure 4.16 shows the doubly differential phase simulated value $\triangle\Phi = \Phi_C - \Phi_F$ as a function of the transverse displacement of the two clouds from the source masses symmetry axis. Simulated data exhibit a parabolic trend $\triangle\Phi = ax^2$ with $a = 29$ μrad/mm^2 yielding for a ±1 mm deviation an error of 29 μrad corresponding to a relative error on

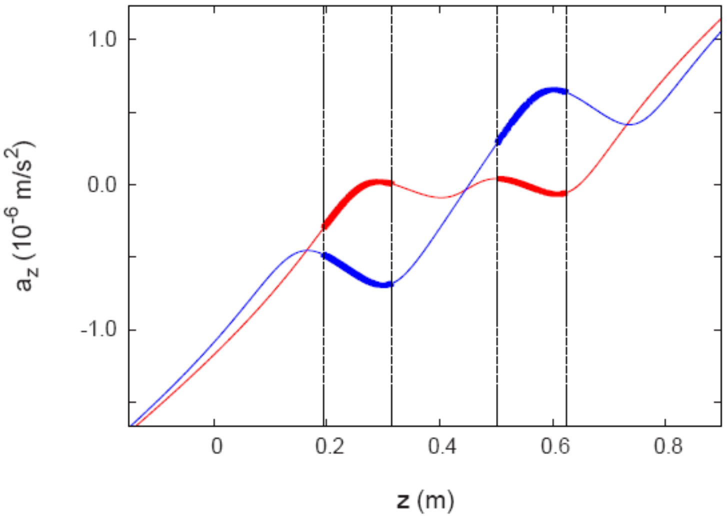

Figure 4.15: Simulated vertical acceleration profile in C (red) and F (blue) configuration. The interferometer regions are indicated by thick lines. The acceleration a_z is due only to the source masses and earth gravity gradient contributions [43].

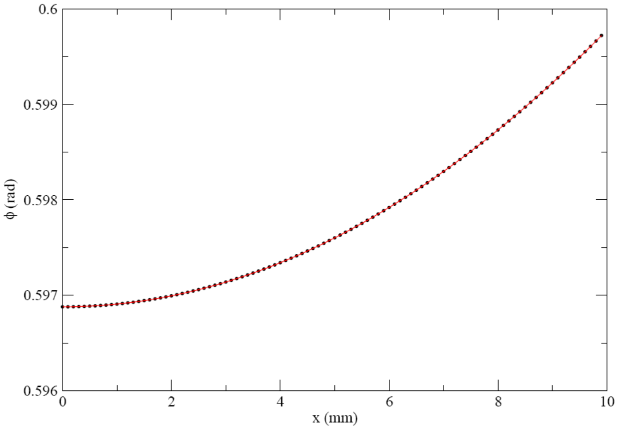

Figure 4.16: Results of a numerical simulation of the phase of atom interferometry doubly differential measurement for a single atom. The solid line is a parabolic fit to the points from simulation. On the x-axis the distance from the source masses symmetry axis is reported.

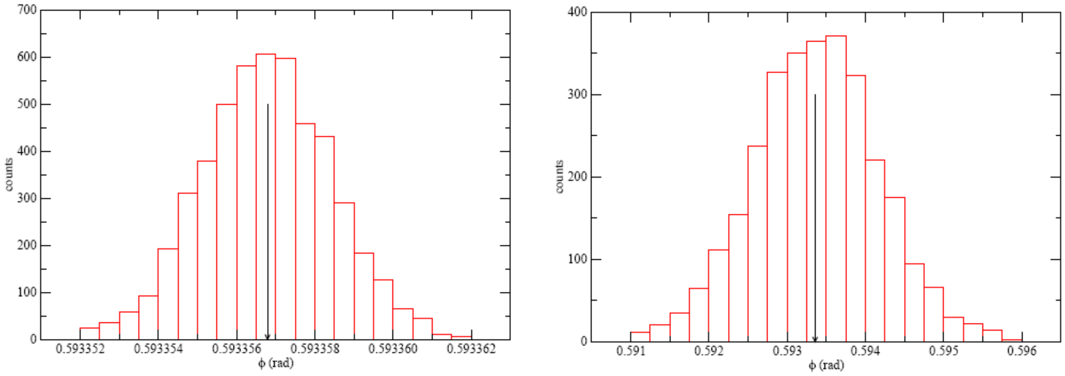

Figure 4.17: Left: histogram for $\Delta\Phi$ spread due to mass uncertainty $\triangle m = 0.5$ g. The black arrow marks the theoretical value. Right: histogram for $\Delta\Phi$ spread due to position uncertainty 2ρ =1 mm. The black arrow marks the theoretical value.

G equal to 5×10^{-5}.

These results are for a point-like interferometer and are useful only for first order evaluations. In fact, transversely, our samples are still thermal clouds with a finite size. Therefore for a complete evaluation of systematics we need to run the simulation in Monte Carlo mode.

Source mass

As described in section 3.4.1, tungsten cylinders shape, weight, density and arrangement has been carefully characterized. Next step is to estimate how positioning (~10 μm) and in weighting (~10 mg) errors can contribute to systematic shifts. To this purpose the experiment has been simulated several times according to following procedure:

- the finite mass resolution scale has been modeled by adding to each cylinder a uniformly distributed random number within a given interval $\triangle m$. For each configuration realized in such way, phase difference for a full doubly–differential measurement has been evaluated. The resulting $\triangle\Phi$ histogram for $\triangle m = 0.5$ g is reported in figure 4.17.

- the effect of finite resolution in positioning the cylinders has been model in a similar manner: a finite resolution of 2ρ in measuring the x and y cylinders coordinates is modeled with a radial uniform distribution of radius ρ, i.e. the position can be anywhere, with uniform distribution, in a circle of radius ρ mm around the nominal position. The simulation has been performed for 2ρ =1 mm (see figure 4.17), 100 μm and 10 μm.

The resulting histograms have a reasonably Gaussian shape and negligible systematic shift from the theoretical value. Looking at the results we can state that mass weight is never a problem: for $\triangle m = 0.5$ g we have $\sigma_{\triangle\Phi} = 1.6$ μrad corresponding to a relative error on G of 2.7×10^{-6} and considering our uncertainty ($\triangle m = 0.010$g) we can totally neglect the mass contribution. Instead, more critical is the positioning issue: a resolution of 50 μm is required to approach the 10^{-4} limit. At our uncertainty level ($\rho = 10\mu$m) the relative error drops to about 5×10^{-5}.

Finally, also the effect of cylinders density inhomogeneity has to be taken into account. As described in section 3.4.1, our cylinders (radius R, height H) are actually not homogeneous, showing a radial as well as an axial density gradient. Therefore we can define a density function $\rho(r,z)$ in cylindrical coordinates as follow:

$$\rho(r,z) = \rho_0(1+\gamma_z 2z/H + \delta_z 2\left|z\right|/H)(1+\gamma_r r/R) \simeq \rho_0(1+\gamma_z 2z/H + \delta_z 2\left|z\right|/H + \gamma_r r/R) \quad (4.31)$$

where ρ_0 is the density at the center of the cylinder, γ_z and γ_r are respectively the axial and the radial gradient and δ_z is an even term to model axial gradient asymmetry. To calculate the order of magnitude of these terms we approximate $U(r,\theta)$ (equation 4.11) with the monopole l term and the inhomogeneous corrections with the lowest nonzero l term. Moreover the effect of the potential on Φ is maximum at the trajectory inversion points which are corresponding roughly to $P_\pm = (2R, \pm H/2)$ in the cylinder coordinate system. By performing the calculations in these points with $\gamma_z = 0.5\times10^{-3}$, $\gamma_r = 2\times10^{-3}$ and $\delta_z = 2\times10^{-3}$ we have:

$$\left.\frac{U_1(P_\pm)}{U_0(P_\pm)}\right|_{\gamma_r=0,\delta_z=0} \simeq 2.5\times10^{-5}, \;\left.\frac{U_2(P_\pm)}{U_0(P_\pm)}\right|_{\gamma_z=0,\delta_z=0} \simeq 1\times10^{-6}, \;\left.\frac{U_2(P_\pm)}{U_0(P_\pm)}\right|_{\gamma_r=0,\gamma_z=0} \simeq 0.6\times10^{-6} \quad (4.32)$$

Clearly the main contribution is given by the dipole term (U_1) while we can neglect the quadrupole ones (U_2). The effect on the G measurement is easily deduced noting that $U_1(P_-) = -U_1(P_+)$ and that in a doubly-differential measurement the shift is proportional to $[U_1(P_-)-U_1(P_+)]-[U_1(P_+)-U_1(P_-)] = -4U_1(P_+)$. So we can conclude that $\Delta G/G \simeq 4(U_1(P_\pm)/U_0(P_\pm)) \simeq 10^{-4}$. This takes place in the unlucky condition in which all the mass dipoles are pointing in the same direction. Instead, they are randomly arranged with a probability $p = 0.5$ to be "up" or "down" oriented, so we can treat this problem in terms of binomial distribution. Consequently the previous systematic shift scale to $\sim 2\times10^{-5}G$.

Chapter 5

Measurements

This chapter is dedicated to the presentation of the measurements performed in the last years on the MAGIA experiment. In the first section we will provide a detailed discussion regarding precision, sensitivity and accuracy of the instrument, paying particular attention to the systematic effects concerning the G measurement. In the second section we will describe how a gradiometer can be use to determine the gravity acceleration and gravity gradient simultaneously, showing also experimental results. Finally, in the last section, our last G measurement attempt is reported together with the error budget.

5.1 Gradiometer characterization

5.1.1 Clouds trajectories

In the following we will give a careful characterization of the atomic density distribution in our fountain. We will separately describe the measurement of vertical and horizontal degrees of freedom.

Measurement of the vertical coordinates

For the knowledge of vertical positions and velocities we employed time of flight (TOF) measurements. We determined the instant t_a at which the velocity selected atoms reach the trajectory apogee, i.e. when $v_z = 0$. Such condition can be easily identified using a Raman π transition: if atoms are at rest roughly half of them, performing the transition, will acquire a momentum recoil of $+2\hbar k_{\mathrm{eff}}$ while the remaining fraction $-2\hbar k_{\mathrm{eff}}$. As a consequence the detected signal shows two distinguishable and symmetrical peaks and thus we can also measure the detection time $t_d^{\pm}$ of such peak doublet. Knowing the vertical position z_0 of the detection light sheet we can derive the apogee vertical coordinate z as follow:

$$z - z_0 = \frac{1}{2} g \left(t_d^{\pm} - t_a\right)^2 + v_0^{\pm} \left(t_d^{\pm} - t_a\right) \tag{5.1}$$

where $v_0^{\pm} = \pm 2\hbar k_{\mathrm{eff}}/m_{Rb}$ represents the initial velocity of the sample. This can be done independently on both clouds. This procedure is simple and particularly convenient: only selected atoms are involved, avoiding in this way to probe the thermal cloud; furthermore, even if Raman transitions are employed, measurements are immune from light shift: in fact, this affects only the frequency of the Raman transition, leaving the condition $v_z = 0$ unaltered. An accuracy of ±0.1 mm in vertical position has been reached, which leads to a relative systematic error on G of 2×10^{-6}, if atoms are properly placed on the stationary points of the gravitational potential.

Measurement of the horizontal coordinates

We measured the position of MOT and launch tilt angles of the two clouds in the atomic fountain. To correctly evaluate systematic effect on G, all these measurements have to be done with respect to the symmetry axis defined by the source masses and the gravity. At this purpose we carefully aligned the Raman beams along such axis and then we used it as a tool to probe the atomic samples. We aim at a verticality level better than 100 μRad.

Optical alignment of the reference frame We measured the parallelism of the optical windows on the Raman beams path by observing the reflection of a laser beam from the two surfaces of each window; in this way we checked that the parallelism of windows is better than 50 μrad, in agreement with the manufacturer's specifications. This means that the residual wedge of the windows is completely negligible for our purposes.

Afterwards we adjusted the horizontality of the retro-reflecting Raman mirror using as a reference a liquid surface (glycerol), properly optimized in order to have a horizontality level of ±10 μrad. We placed the liquid surface on the top of the interferometer tube and then we sent a probe beam through the liquid interface toward the Raman mirror. Therefore, adjusting the Raman mirror, we made parallel the two corresponding reflected beams. The beams parallelism has been verified along a distance of $\sim$ 30 m with a resolution of 3 mm. Raman mirror tilt is monitored by a tiltmeter (Applied Geomechanics 7551129) applied to its rear surface, in order to mantain the horizontality.

As a final step, using an iris, we selected the central part of the Raman beams ($d = 3$ mm) and we forced the resulting light spot to go through the reference iris (see section 3.3.2) placed at the top of the interferometer tube. Maximizing the retro-reflected power passing through the first iris, a correct Raman beams geometry is ensured, i.e. a good Raman beams overlap and positioning along the source masses symmetry axis. We estimate a verticality within 100 μrad.

Clouds coordinates during the flight We measured the horizontal positions of atomic clouds at different heights during their ballistic flight. A portion of radius $r \simeq 2$ mm of the downward-propagating Raman beam was selected with a diaphragm mounted on a 2D motorized translation stage. We addressed the atoms with three Raman π pulses in rapid sequence (see section 4.2.2 for more details), and then we detected the number of atoms in the $|F = 1\rangle$ state. We probed the horizontal distribution of atomic density in both clouds simultaneously by changing the diaphragm position.

The number of detected atoms is proportional to the atomic density in the column selected by the diaphragm and to the Raman transition probability. We deduced the distribution of transition probability from the intensity profile of Raman beams and from the direct measurement of transition probability versus Raman power. Supposing to scan a 2D Gaussian-shaped atomic distribution $G_a(x, y)$ along a certain horizontal plane, the number of address atoms N_{at} can be written as

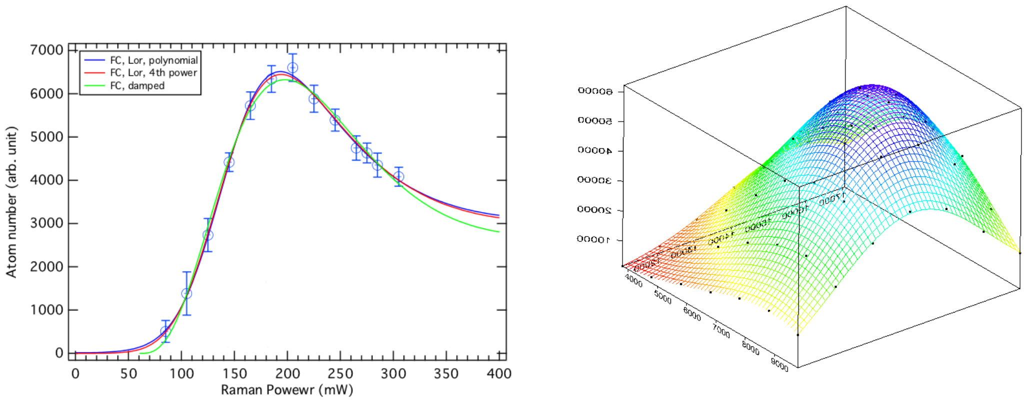

Figure 5.1: Left: Measured transition probability of a triple sequence of Raman pulses versus the optical power of Raman beams; solid lines represent the least-squares fit with different models discussed in the text. Right: Measured distribution of an atomic cloud at the velocity selection and reconstructed density profile.

$$N_{at}(x) = \int_{x-r}^{x+r} \int_{y-r}^{y+r} G_a(x', y') P(I(x', y'))^3 dx' dy' \tag{5.2}$$

where $P(I)^3$ is the triple pulse transition probability function to determine. Placing the diaphragm on the Raman beam waist we can approximate $I(x)$ as a constant function I_m. Therefore the previous expression yields to

$$N_{at} \propto P(I_m)^3 \tag{5.3}$$

In figure 5.1, left part, the measured transition probability is reported in function of Raman total power. Also sinusoidal fitting models with exponential (green line) and Lorentzian damp (red and blue line) are included, in order to individuate the curve that best follows the experimental points. In the right part, an example of measured atomic distribution together with a 2D-fit realized through the convoluted function (5.2) is also shown. Performing this kind of measurement along a reticular pattern (square 7×7 mm, lattice period 1 mm), we can provide a complete 2D picture of both the samples. The time required for a single scan is approximately an hour.

In figure 5.2 positions of the upper and lower cloud barycenters at five different times T (T =0, 50, 100, 150 and 200 ms) after velocity selection are reported. We took each point in both source masses configurations in order to investigate possible effects related to the mass movement. In figure 5.3 the corresponding time evolution of the clouds radius $\sigma(t)$ along the transverse plane is also shown. Considering a simple free expansion model, such as

$$\sigma(t)^2 = D^2 + \frac{k_B \Theta}{m} t^2 \tag{5.4}$$

where D is the initial cloud size, it is possible to evaluate the transverse temperatures Θ_x and Θ_y of the velocity selected samples.

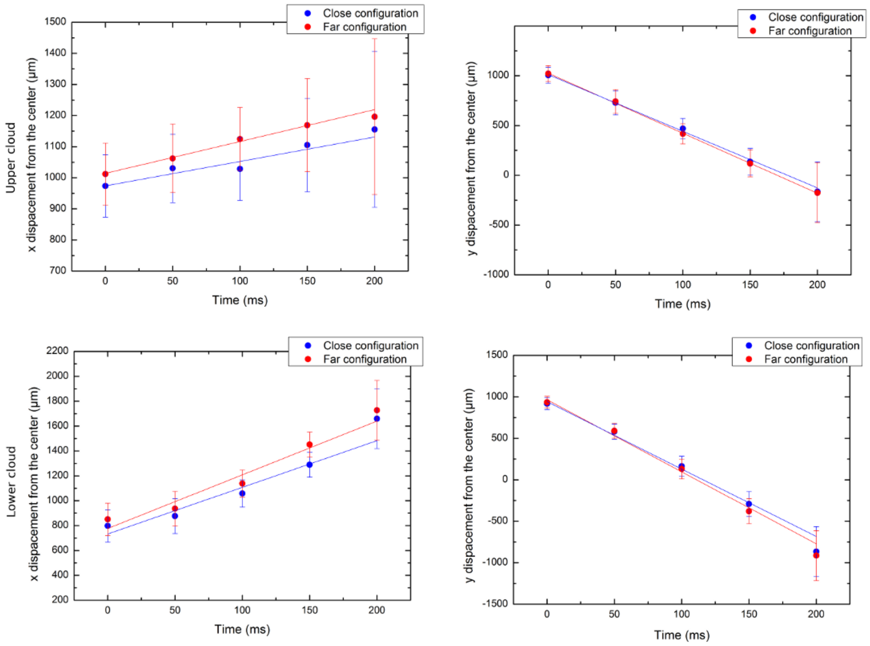

Figure 5.2: Horizontal coordinates of the barycenter of the two clouds at four different times of flight in C (red traces) and F (blue traces) source masses configurations.

Looking at the results we can draw the following conclusions:

- Even having a good resolution in position ($\sim 100\mu$m), our method is not sensitive enough to measure accurately small changes (< 0.5 mm/s) in the transverse velocity.
- The transverse temperatures are not equal and consequently the samples expansion is not spherically symmetric. Moreover, the temperature values are always equal or less than 1 μK, i.e. much lower than the expected value.
- Our method is less effective at large T, i.e. when the atomic cloud begins to be larger than Raman beam waist.

Because of Coriolis force, a transverse velocity change of 0.2 mm/s produces a systematic shift up to 8.6 mrad on Φ, which can seriously limit our accuracy. Regarding the positioning issue, a cloud of radius $\sigma = 5$ mm and offset 5.0 ± 0.1 mm yields an angular correction on $\triangle\Phi$ due to source masses potential of 1.450 ± 0.030 mrad, corresponding to a relative error on G of $\sim 6 \times 10^{-5}$. Cloud centering can help to further reduce the uncertainty on this contribution. However, in order to properly correct long term drifts, we will need to probe our samples at least once a day. To this purpose a better understanding of the MOT behavior may be very useful to figure out what kind of drifts affect the launch. Indeed, in the case of a simple launch direction variation, MOT position can be treated as a fix point and a single cloud measurement will be enough for a complete description, reducing the measurement time of a factor two. Furthermore this can be done in the first part of the interferometer, when cloud size is smaller.

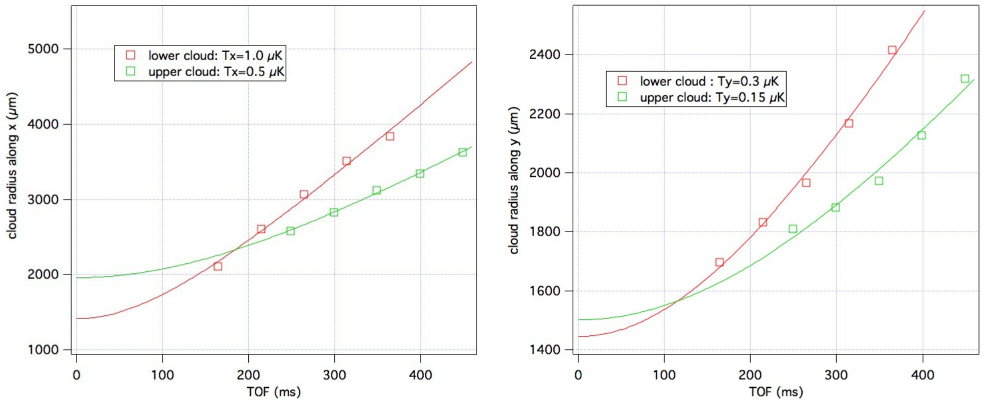

Figure 5.3: Clouds expansion during the interferometer time. Red points are referred to the lower cloud, green points to the upper one. The corresponding solid lines are the least-square fits obtained using the free expansion model (see equation 5.4). The origin of the time is determined by the launch instant.

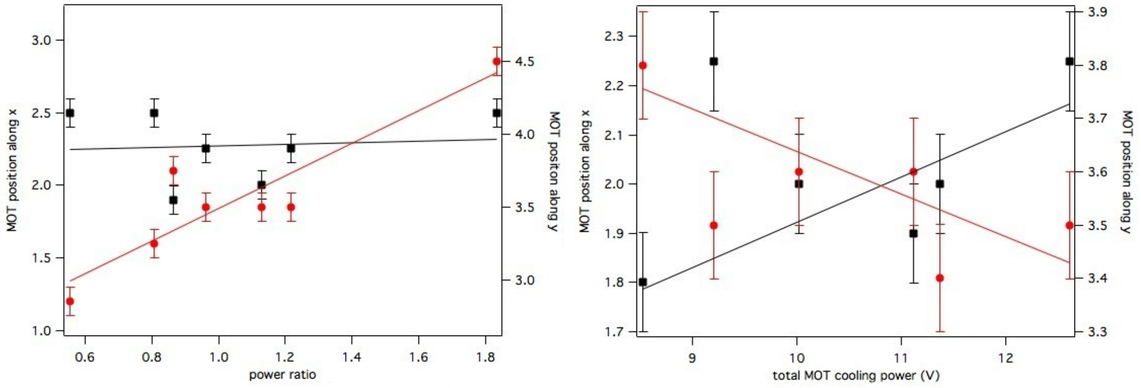

Figure 5.4: MOT position vs. total cooling power (left graph) and upper and lower MOT beams power ratio (right graph). x coordinates are reported in black, y coordinates in red. Linear fits are also shown.

Atomic coordinates of the MOT center In order to probe the atomic density distribution in the MOT we tuned the frequency of one Raman laser to the $F = 2 \rightarrow F' = 3$ transition. Using a diaphragm we selected a thin portion (radius 0.5 mm) of the resonant upwards-propagating beam. The diaphragm is mounted on a 2D translation stage in order to accurately control the beam horizontal position with respect to our reference. When the light hits the MOT, atoms are pushed away from the trap region and thus the fluorescence light decreases. In particular the MOT center is identified by the minimum fluorescence condition, i.e. when the MOT actually vanishes. Following this procedure we measured the MOT position with respect to some relevant parameters such as total cooling power, up-down beams power ratio, B field compensation coils and MOT coils current. Some results are shown in figure 5.4. Coil currents can easily be controlled with high accuracy and their contribution is negligible. Instead, cooling power can vary by few percent within a day. However typical long term fluctuations (5%) both in total power and power ratio produce position drifts below 0.1 mm, which represent also the sensitivity limit of our method. To be conservative we can state that our MOT center is stable within $\pm 100\mu$m on a time scale of few days.

5.1.2 Influence of the most relevant experimental parameters

Noise sources which equally affect the upper and lower atom interferometer (i.e. vibrations, tidal effects, phase noise of Raman lasers, etc.) are rejected as common mode in the gravity gradient measurement. In this section we will investigate those experimental parameters which affect the two atom interferometers differently; such parameters can in principle limit the sensitivity and long term stability of gravity gradient measurements. However, many sources of noise and systematic error are efficiently canceled in the doubly differential measurement for G. In particular, the only effects which can affect the G measurement are those which either depend on the position of source masses, or change on a time scale shorter than the cycling time T_{mod} of masses positions. We separately investigated the effect of various parameters. We recorded the ellipse phase angle in the two configurations of source masses, Φ_C and Φ_F, for different values of each parameter; for each of them, we calculated the total ellipse angle $\bar{\Phi} = (\Phi_C + \Phi_F)/2$ and the difference of ellipse $\triangle\Phi = \Phi_C - \Phi_F$ angle between the two different masses positions. From $\bar{\Phi}$ we can deduce requirements on the long term stability of the parameter for gradient measurements, as well as on the stability on time scales shorter than T_{mod} for G measurements; from $\triangle\Phi$ we can deduce requirements on the long term stability for G measurements.

Intensity fluctuations of cooling laser

The total intensity and intensity ratio of the six MOT laser beams affect the number of atoms as well as the temperature and launching direction in the atomic fountain. In principle, such effects may influence the upper and lower interferometers differently. As described in section 4.1.1 and 3.1.4 the six MOT beams are produced as two independent sets from a single MOPA. The MOPA output is split in two parts, the “up” and “down” beams, which are separately controlled in frequency and amplitude with two AOMs on an optical bench. Each of these beams is then coupled into a polarization maintaining (PM) optical fiber and sent to a commercial $1 \rightarrow 3$ splitter to produce a triplet of beams, which are delivered through PM fibers to collimators attached to the MOT chamber. In our setup, intensity fluctuations of MOT laser beams are dominated by changes in the AOM and fiber coupling efficiency of the “up” and “down" beams in the optical bench, while fluctuations generated in the $1 \rightarrow 3$ splitters are negligible. This is shown in figure 5.5, where the typical intensity fluctuations of the “up” and “down” beams at the input of the $1 \rightarrow 3$ splitters are

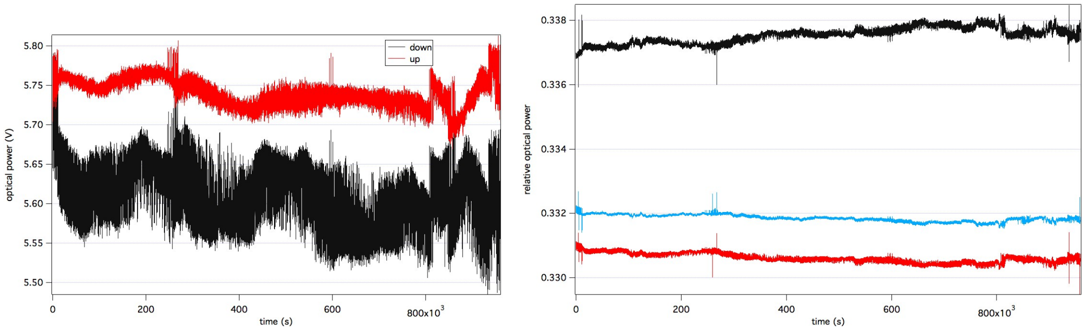

Figure 5.5: Time plot of MOT laser intensities; the left plot shows the readings of two photodiodes at the input of the 1 → 3 splitters over about eleven days; the right plot shows the relative readings of three photodiodes monitoring the output of MOT collimators within the triplet generated from the "down" beam over the same time interval.

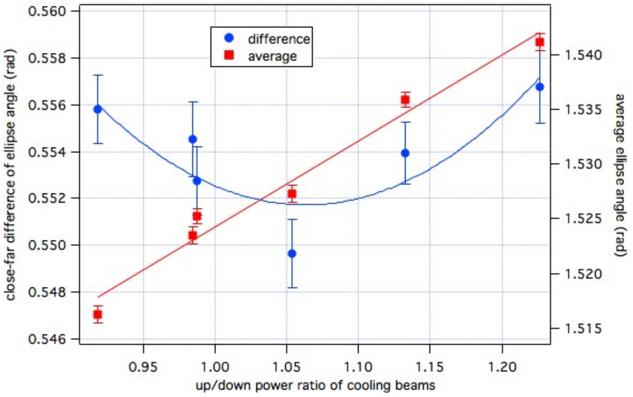

Figure 5.6: Total and differential ellipse angle for the two configuration of source masses, versus the intensity ratio between up and down cooling laser beams.

compared with the relative intensity fluctuations at the output of the MOT collimators, within the triplet generated from the "down" beam. The RMS fluctuations of intensity ratio between "up" and "down" beams are larger than the relative intensity fluctuations within each triplet by one order of magnitude.

For this reason, we can restrict the analysis to the effect of intensity fluctuations at the input of the 1 → 3 splitters. We measured the ellipse phase angle for different values of the intensity ratio of "up" and "down" beams, by keeping the total intensity constant. The results are shown in figure 5.6. The total angle Φ is very sensitive to the intensity ratio, while there is no clear evidence of any variation of the difference angle $\triangle\Phi$.

From a linear fit we find that changing the up/down intensity ration by 1% induces a shift of 0.8 ± 0.06 mrad on Φ. A parabolic fit of the $\triangle\Phi$ data provides an estimate of $\sim 20\,\mu\text{rad}/\%^2$ to the small quadratic dependence. By recording the time of flight (TOF) of atomic clouds from launch to the detection region, we observe that changes in the up/down intensity ratio induce a vertical shift of the MOT position with a coefficient of about 0.1 mm/%. However, this effect cannot explain the measured shift on $\bar{\Phi}$; in fact, we investigated the vertical gravity gradient and the magnetic gradient in the interferometer tube (see below for more details): the calculated $\bar{\Phi}$ shift from both gradients is smaller than the measured ∼8 mrad/mm linear coefficient by one order of magnitude. We conclude that the effect of the up/down intensity ratio on $\bar{\Phi}$ is mainly determined from changes in the temperature of atomic clouds. When changing instead the total intensity of MOT beams at constant intensity ratio, we find an upper limit of ~ 20 μrad/% for the linear coefficient of both $\bar{\Phi}$ and $\triangle\Phi$.

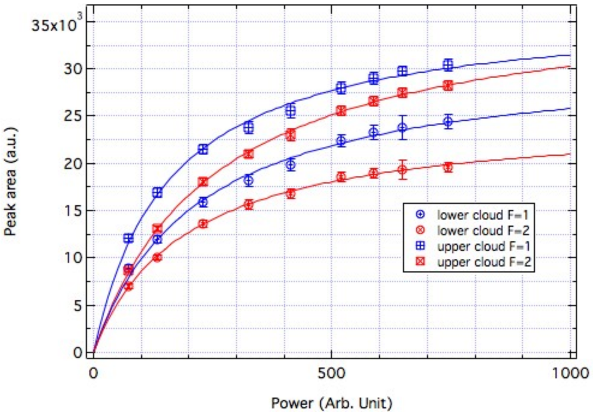

Figure 5.7: Signal amplitude in the four fluorescence detection channels versus intensity of probe laser beam.

Detection

The optical intensities of probe and repumper beams affect the photon scattering rate of the atoms, and thus the signal at the two detection channels. Any unbalance between the efficiencies of the two detection channels may result in principle in a shift of the ellipse phase angle. In the following we discuss possible sources of detection unbalance, and the magnitude of the effect on the gravity gradient measurement.

Relative efficiency of detection channels An efficiency unbalance between the two detection channels may arise from either differences of size and power of probe beams, or from limited repumping efficiency of $F = 1$ atoms, or from geometrical differences between the two optical systems for fluorescence collection. In principle, it is possible to compensate for any detection unbalance originated from geometrical differences by properly adjusting the intensity ratio of probe beams. However, if the probe beams have unequal intensities, the saturation parameter is different for the two detection channels; as a result, even common mode intensity fluctuations will be convert into changes of detection efficiency ratio ϵ. We verified that, when the intensities of the two probe beams are carefully equalized, the ϵ parameter determined from ellipse distortion has a value around -0.3 (see section 4.5.1 for more details); if we change the intensity ratio to adjust $\epsilon \simeq 0$, the long term fluctuations of ellipse phase angle, as determined from the Allan variance, are enhanced.

We directly measured the saturation intensities in the two detection regions by recording the

Cloud	Channel	I_s (A.U.)
upper	F=1	157±10
upper	F=2	256±9
lower	F=1	217±19
lower	F=2	192±8

Table 5.1: Effective saturation intensity for the two clouds in the two detection channels.

signals after velocity selection plus a single π pulse for different intensities of the probe laser. In figure 5.7 the four curves represent the peak area of the two detection channels for the two clouds, versus the intensity of probe beams. The intensity ratio of probe beams was kept constant along the measurement, and the two intensities of the two detection channels were carefully equalized. Moreover, the repumper intensity was kept fixed during this measurement. We fitted the observed signals to the curve

$$I(x) = k\frac{x/I_s}{1 + x/I_s}$$

where the fit parameter k depends on the number of atoms and on the detection efficiency, while I_S gives the saturation intensity. The resulting values for I_S are given in table 5.1. The difference between F = 1 and F = 2 channels may depend on unequal intensities or beam shapes; moreover, the difference of I_S in F = 2 for the two clouds is 64±12, which is not consistent with zero. A possible explanation for such discrepancy may be in the different size of the two atomic clouds, which would experience a different total detuning in the presence of magnetic gradients in the detection region, as well as a different total detection efficiency due to the geometry of the optical system for fluorescence collection.

Intensity fluctuations of probe laser beams In our setup, the intensity ratio of probe beams is passively stabilized to 0.1% with an high extinction polarizer placed before a second beam splitter polarized used for obtaining the two detection light sheets. As a result, probe intensity fluctuations are essentially common mode between the two channels. However, as shown in the previous paragraph the ellipse phase angle can still depend on the total power of probe beams, as well as on the power of the repumping beam. We recorded the ellipse phase angle, in the two configurations of source masses, for different values of the total probe laser intensity I_p. The results are shown in figure 5.8 (left).

The slope of the $\bar{\Phi}(I_p)$ curve decreases when I_p is above the saturation intensity. Close to our typical experimental conditions, $\partial\bar{\Phi}/\partial I_p$ = -0.15±0.04 mrad/%. For the sensitivity of the difference angle $\triangle\Phi$ on I_p we derive a limit of ~90 μrad/%. We also measured the effect of intensity changes in the repumper beam. The results are shown in figure 5.8 (right). Changes in the optical intensity of repumper modify the detection efficiency in the $F = 1$ channel; around our typical experimental conditions, the phase angle $\bar{\Phi}(I_p)$ decreases with repumper power with a slope of -0.10±0.02 mrad/%. The sensitivity of the differential phase angle $\triangle\Phi$ is below 0.1 mrad/%.

Raman lasers

When the detuning of the Raman lasers is fixed, the intensities of Raman beams determine the Rabi frequency, i.e. the probability of the Raman transitions, as well as its spatial distribution due

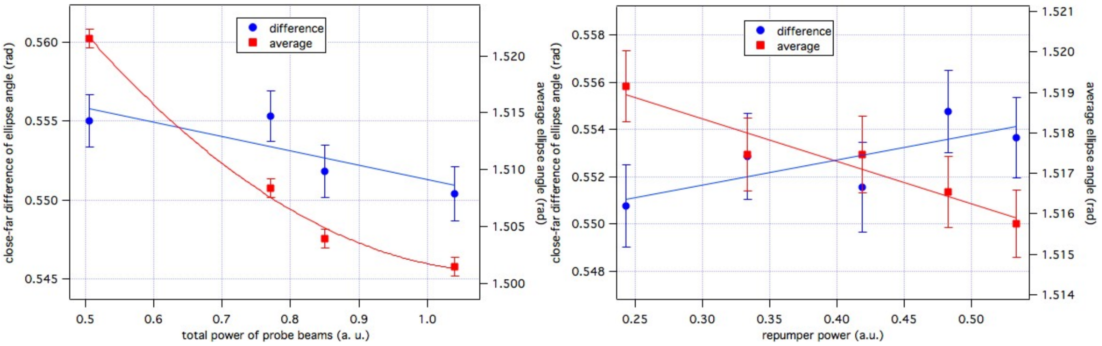

Figure 5.8: Left: total and differential ellipse angle for the two configuration of source masses, versus power of probe laser beams. Right: total and differential ellipse angle for the two configuration of source masses, versus power of repumping light in the probe beam.

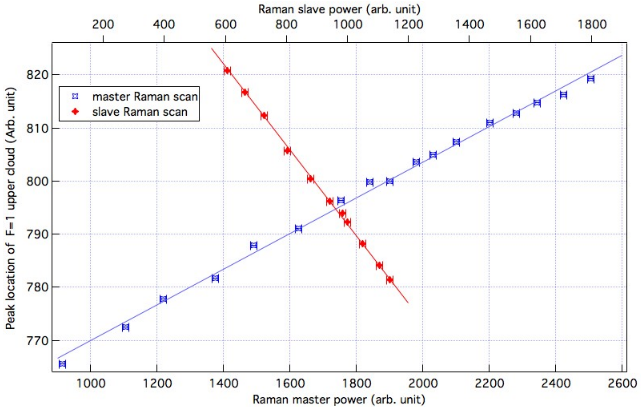

Figure 5.9: Vertical displacement of velocity selected clouds versus power of master and slave Raman beams.

to the intensity dependence of the light shift We set the ratio between the optical power of Master and Slave lasers, P_M and P_S , to the value for which, at the chosen frequency detuning of Raman lasers from the optical resonance, the first-order light-shift is expected to cancel out (see section 2.1.3). We fix the duration of Raman pulses, and adjust the total optical power of Raman beams in order to maximize the efficiency of π pulses. Intensity fluctuations or drifts may change the ellipse contrast; more importantly, they might change the velocity class of selected atoms because of residual light shift.

Effect of light shift In order to precisely cancel the first order light shift, we measured the vertical velocity of the atomic clouds after a single π pulse versus the power of Raman beams. The velocity changes are detected with the time of flight method, i.e. through the arrival time of the atomic clouds in the detection region. At fixed detuning of the Raman lasers, the resonant frequency of the Raman transition can be written as

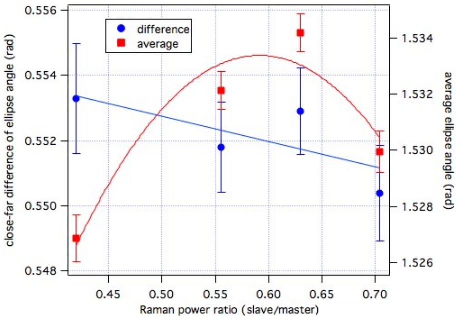

Figure 5.10: total and differential ellipse angle for the two configuration of source masses, versus power ratio of Raman lasers.

$$f(I_M, I_S) = f_0 + \triangle(I_M, I_S) = f_0 + C_M I_M + C_S I_S + o(I^2) \tag{5.5}$$

where f_0 is the unperturbed resonance, and I_M, I_S are the intensities of Master and Slave laser beams, respectively. For a given value of I_M, we measured the position of the upper cloud versus I_S, and vice versa. Figure 5.9 shows the results. We determine the C_M and C_S coefficients by a linear fit to experimental data. By setting the intensity ratio

$$\frac{I_S}{I_M} = -\frac{C_S}{C_M} = 0.45 \pm 0.02 \tag{5.6}$$

we can cancel the first order light shift independently on the total Raman power.

Intensity fluctuations of Raman lasers In order to estimate the effect of Raman laser intensities on the gravity gradient measurement, we recorded the ellipse phase angle for different values of the total Raman power $P_M + P_S$ and of the power ratio P_S/P_M in the two configurations of source masses. The behavior of $\bar{\Phi}$ and $\triangle\Phi$ versus the intensity ratio of Raman laser beams is shown in figure 5.10. The shift of $\bar{\Phi}$ is maximum for a power ratio around 0.59±0.05. From a parabolic fit we determine a curvature of 20±4 μrad/%^{2} around the maximum. From the $\triangle\Phi$ plot we extract a limit of 0.1 mrad/% for the sensitivity of the differential angle on the Raman power ratio.

In a similar way we determine the influence of total Raman power when P_S/P_M =0.45. We measure a sensitivity on $\bar{\Phi}$ of 0.3±0.04 mrad/%, which can be attributed to the combination of residual first-order light shift and second order light shift. The sensitivity on $\triangle\Phi$ is below 0.1 mrad/%.

Alignment fluctuations of Raman beams We align the Raman beams along the vertical direction with sub-mrad precision. However, small fluctuations in the propagation direction of Raman beams would couple with the gravity gradient measurement via the Coriolis effect. All of the mounts for the optical steering of the Raman beams have been chosen to be extremely rigid, and fluctuations in the propagation direction are essentially dominated by the tilt of the retro-reflection mirror which is mounted on the top of the structure holding the source masses. We directly observed the effect of mirror tilt on the ellipse phase angle. The Raman retroflection mirror is mounted on a precision, dual-axis tiltmeter, that measures the inclination θ_x and θ_y along two axes. The y axis is oriented

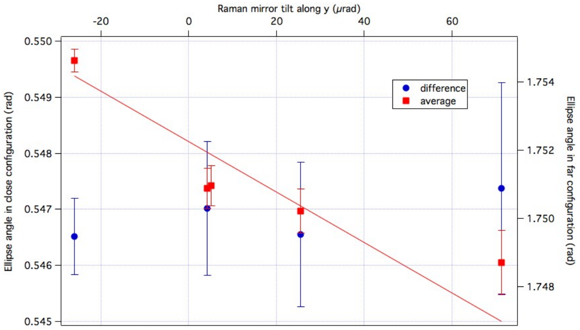

Figure 5.11: total and differential ellipse angle for the two configuration of source masses, versus tilt of the Raman mirror along the y direction. The solid line is a linear fit to the $\bar{\Phi}$ data.

along the West-East direction within a few degrees. We recorded several ellipses for different values of the mirror tilt θ_y , by keeping θ_x constant, and vice versa. The results of total and differential ellipse phase angle versus θ_y are shown in figure 5.11.

From a linear fit to the $\bar{\Phi}$ data we derive a sensitivity of -37±5 mrad/mrad, in good agreement with equation 2.85. In a similar way we measure a sensitivity of -5±2 mrad/mrad for the $\bar{\Phi}$ dependence on θ_x , which is compatible with equation 2.85 assuming an angle of $\sim 8^\circ$ between the x axis and the North-South direction. From the $\triangle\Phi$ data there is no evidence of any direct effect of mirror tilt on the differential phase angle. Never the less, the influence of Coriolis shift on G measurement is not negligible, because of a tiny deformation of the mechanical structure which is induced by source masses. In fact we observe that the vertical translation of source masses induces a tilt of the Raman mirror, so that θ_y changes by $\sim$10 μrad between the two configurations. This results in a bias of $\sim$350 μrad on $\triangle\Phi$, corresponding to a systematic error of 6×10^{-4} on G. This bias can be easily reduced by either correcting $\triangle\Phi$ through the measured mirror tilt, or by actively stabilizing the angle of the mirror.

Effect of magnetic fields

Magnetic fields affect the atom interferometry measurement mainly in two ways: through the impact on atomic trajectories and through the Zeeman shift of energy levels along the atom interferometry sequence. We use several coils to separately create well controlled bias fields in the MOT region and in the fountain tube. In our experiment, the interferometer tube is surrounded by two concentric cylindrical μ-metal layers, that attenuate external magnetic fields by more than 60 dB in the region where the atom interferometry sequence takes place. The MOT and detection chambers, on the contrary, are not shielded.

MOT compensation coils The launching direction of the atoms in the fountain is sensitive to the magnetic field in the MOT region. In fact we perform a fine tuning of the fountain alignment by acting on the current of three pairs of Helmholtz coils, which are oriented along three orthogonal axes to create a uniform bias field at the position of the MOT. In order to investigate the sensitivity of the gravity gradient measurements on the magnetic fields in the MOT region, we recorded several ellipses for different values of the current in the compensation coils. As an example, figure 5.12

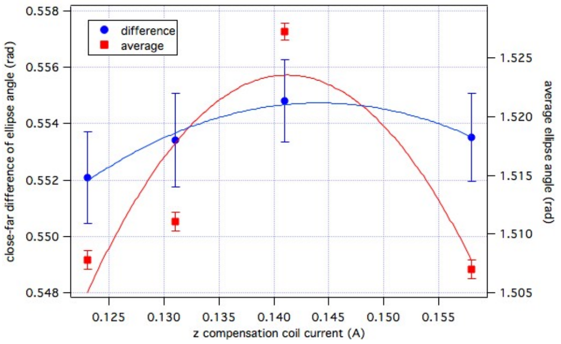

Figure 5.12: Total and differential ellipse angle for the two configuration of source masses, versus current in vertical compensation coils.

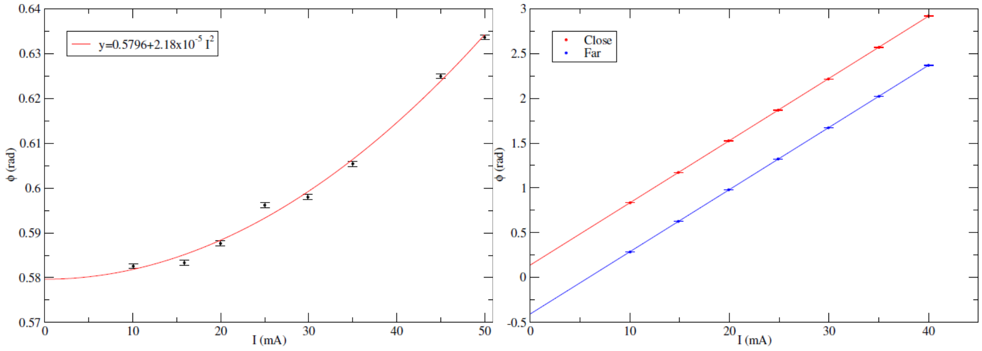

Figure 5.13: Left: ellipse phase angle versus current in vertical bias solenoid, without magnetic pulse from the short coil; Right: Ellipse phase angle for the two configurations of source masses versus current in vertical bias solenoid, with applied magnetic pulse from the short coil.

shows the plot of $\bar{\Phi}$ and $\triangle\Phi$ for the two configurations of source masses, versus the current in the vertical compensation coils. The $\bar{\Phi}$ data clearly show the presence of a maximum around 140 mA, with a curvature of 56±3 μrad/mA^2 . At our typical operating conditions (i.e. around 130 mA) the linear sensitivity is ~1 mrad/mA. Since the vertical compensation coils produce a field of 0.22 mT/A, this converts into a sensitivity of ~4.5 mrad/μT. Again we find no evidence of any effect on the differential ellipse angle.

Bias field in the interferometer tube A 1 m long solenoid inside the μ-metal tube creates a uniform magnetic field $B \simeq 35$ μT to define the quantization axis during the interferometric sequence. Although the interferometer sequence is applied to atoms in the $mF = 0$ non magnetic state, any magnetic gradient B' will induce a phase shift through the second order Zeeman effect, as described in section 2.2.4. We investigated the presence of magnetic gradients by recording the ellipse phase angle versus the current i_s in the solenoid. The results are shown in figure 5.13 (left).

The data are reasonably consistent with a parabola with the vertex at $i_s = 0$ and curvature 22±2 μrad/mA^2, corresponding to ~0.22 μrad/μT^2 . This means that the bias coil does not

Parameter α	$\bar{\Phi}(\alpha)$ slope/curvature	$\langle\delta\alpha\rangle_{RMS}$
Probe power	-0.15±0.04 mrad/%	1%
Repumper power	-0.1±0.02 mrad/%	1%
Raman power ratio	20±4 μrad/%^{2}	2%
Raman total power	0.2±0.05 mrad/%	2%
MOT total power	$<$ 20 μrad/%	2%
MOT power ratio	0.8±0.06 mrad/%	2%
vert. MOT comp. coil	56±3 μrad/mA^2	20 μA
bias solenoid (no pulse)	22±2 μrad/mA^2	20 μA
bias solenoid (with pulse)	69.4±1 mrad/mA	20 μA
Raman mirror E-W tilt	37±5 mrad/mrad	10 μrad
Total RMS noise		~3.5 mrad

Table 5.2: Sensitivity of $\bar{\Phi}$ to most relevant parameters.

generate a perfectly uniform field. The effect is however quite small, and is compatible with the total magnetic gradient between the locations of the two clouds arising from the finite size of the solenoid, for which $\Phi \propto B'^2 \propto i_s^2$ (see equation 2.90, third term). On the other hand, there is no detectable stray magnetic field in the tube: indeed, in such case, we have that $\Phi \propto B' \propto i_s$ (see equation 2.90, second term, considering $\triangle B_{Up-Dw}$ independent from i_s). An upper limit is obtained by fitting the data with a parabola with a linear term. The vertex is at $i_s = 2$ μA which corresponds to 3 nT. In our typical working conditions, i.e. 20 mA, the sensitivity is below 0.9 mrad/mA. For the measurement of gravity gradient, it is necessary to extrapolate the angle at $i_s = 0$.

For the G measurement, a 20 cm long coils creates a magnetic pulse of duration τ_B and magnitude B_1, around the apogee of the lower atomic cloud, during the second half of the interferometry sequence; the corresponding extra phase shift is used to make the eccentricity of ellipses low enough and symmetric in the two configurations of source masses. The magnetic gradient induced by the short coil strongly enhances the sensitivity of ellipse phase angle to solenoid bias current. This fact can be used to detect possible effects of source masses on the static magnetic field in the interferometer tube. This idea is illustrated in figure 5.13 (right), where the ellipse phase angle for the two configurations of source masses is plotted versus i_s. The two plots show a linear dependence, in agreement with the second term of equation 2.90. The slope $\partial\Phi/\partial i_s$ =69.4±0.1 mrad/mA is the same, within the experimental uncertainty of 0.2%, for the two configurations of source masses, i.e. we found no evidence of any influence of source masses.

Summary of relevant parameters

Tables 5.2 and 5.3 summarize the results of our characterization measurements about the influence of most relevant parameters on total and differential ellipse phase angle, respectively. The last column gives the typical RMS fluctuations of the parameters on the time scale of few hours. The impact on long term stability of the gradient and G measurement is discussed in the next section.

Parameter α	$\triangle\Phi(\alpha)$ slope/curvature	$\langle\delta\alpha\rangle_{RMS}$
Probe power	< 0.09 mrad/%	1%
Repumper power	< 0.01 mrad/%	1%
Raman power ratio	< 0.1 mrad/%	2%
Raman total power	< 0.1 mrad/%	2%
MOT total power	< 20 μrad/%	2%
MOT power ratio	20 ± 10 μrad/%^{2}	2%
vert. MOT comp. coil	< 1 mrad/mA	20 μA
Raman mirror E-W tilt	$<$ 5mrad/mrad	10 μrad
bias solenoid (with pulse)	< 140 μrad/mA	20 μA
Total RMS noise		< 0.3 mrad

Table 5.3: Sensitivity of $\triangle\Phi$ to most relevant parameters.

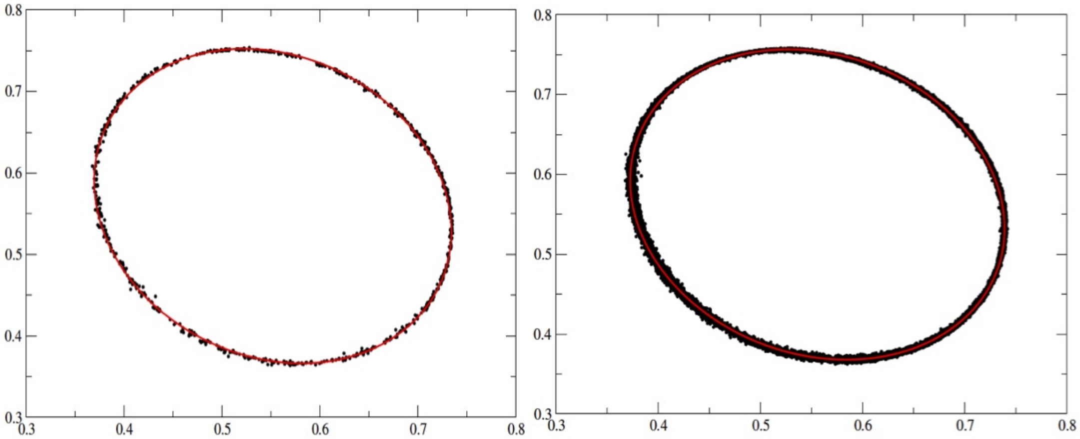

Figure 5.14: Two experimental ellipses obtained with 720 (left) and 19922 (right) points; solid lines are least squares fit to the data.

5.1.3 Sensitivity limits

Figure 5.14 shows two typical ellipses for 720 and ~20000 experimental points. As pointed out in section 4.5.1, we employ a least squares fitting algorithm to extract the differential phase Φ of the gradiometer, using A, B, C, D and Φ itself as free parameters (see equation 4.5). In principle, both the sensitivity and long term stability of the gravity gradient measurement can be limited by noise in the x and y signals, as well as by fluctuations and/or drifts in the contrast and center of the ellipses, and by sources of instability of the Φ value itself. As shown in [34] it is possible to obtain a reliable value for Φ with an ellipse containing a few tens of points. We typically use 72 points per ellipse, corresponding to a measurement time t_{ell} ~136 s. Thus the slow changes in the A, B, C and D parameters occurre on a time scale longer than t_{ell} , as visible in figure 5.14, are efficiently rejected. The short term sensitivity will be mainly determined by detection noise, and possibly by fast fluctuations of ellipse contrast and position, such as those caused by changes in the detection efficiency or in the Raman laser power; the long term stability is limited by slow distortions and rotations of the ellipse, such as those from Coriolis acceleration or detection efficiency changes.

Short term sensitivity The sensitivity of gravity gradient measurement can be modeled by adding two noise terms δx and δy respectively to the two equations 4.5. Let us assume that changes in ellipse contrast and position faster than t_{ell} are negligible. Let us further assume that the detection efficiency is the same for the two channels, i.e. $\epsilon = 0$. The detection noise can be written as

$$\delta x_{det} = \frac{n_x \delta n_{1x} + n_{1x} \delta n_x}{n_x^2} \tag{5.7}$$

where $n_x = n_{1x} + n_{2x}$, and δn_{1x} (δn_{2x}) is the noise for detection of $|F=1\rangle$ ($|F=2\rangle$) atoms. A fundamental lower limit to δx_{det} is given by the quantum projection noise (QPN) $\delta n_{ij}^2 = n_{ij}$. In our typical experimental conditions ($n_{ij} \sim 6 \times 10^5$ atoms) the noise per shot amounts to $\delta x_{QPN} \sim \delta y_{QPN} \sim 0.0011$. We investigated the QPN limit to the gravity gradient measurements with a numerical simulation: we generated several ellipses described by equation 4.5 with $A \sim B \sim 0.225$, where θ is uniformly distributed in $[0; 2\pi]$ and adding a random zero-mean Gaussian noise term to each line, with standard deviation 0.0012. We calculated the Allan variance for Φ as resulting from least-square fitting of simulated ellipses. The Allan variance $\sigma_\Phi(N)$ drops as the square root of the number N of points, $\sigma_\Phi(N) = 0.015/\sqrt{N}$ rad ; we repeated the simulation for different values of A and B, and verified that $\sigma_\Phi(N)$ scales with the inverse of the contrast.

Figure 5.15 shows the Allan variance of ellipse phase angle in different conditions. Several improvements of the apparatus have allowed to increase the number of atoms and the repetition rate of the experiment, and also to reduce the technical noise at detection and increase the ellipse contrast. We currently achieve a sensitivity of 22 mrad at 1 s, which is close to the calculated QPN limit, and it corresponds to a sensitivity to differential accelerations of 5×10^{-9} g at 1 s, about a factor four better than in [34].

Long term stability The data presented in section 5.1.2 allow to identify the main limits to the stability of Φ measurements, once the typical fluctuations of the parameters are known. We constantly monitor the value of most relevant experimental parameters (i.e. the power of MOT, probe, repumper and Raman laser beams, the current of MOT compensation and bias coils, tilt of Raman mirror) as well as the temperature in different points of the apparatus with a high resolution data logger. From table 5.3 it is apparent that the main contributions will arise from instability of MOT

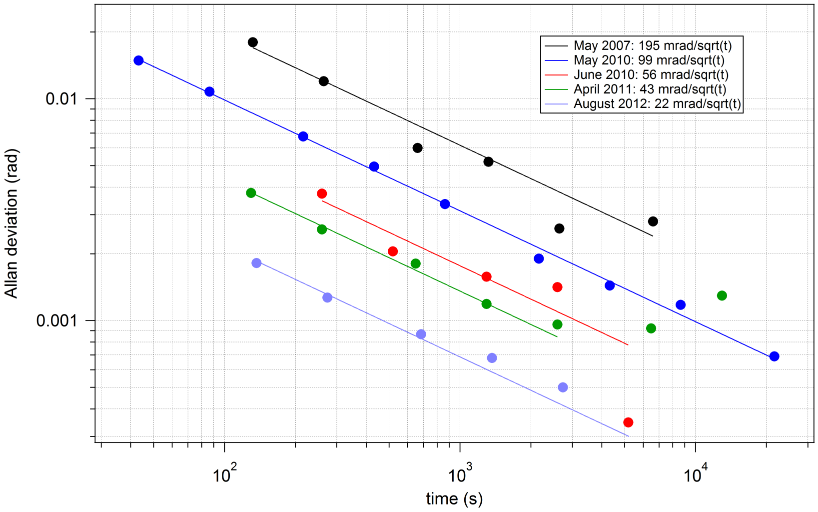

Figure 5.15: Allan deviation of the ellipse phase angle in different configurations of the experiment. Between May 2007 and May 2010, the main improvements were a larger number of atoms and a faster repetition rate, after the implementation of a 2D-MOT and more powerful Raman laser sources; between May and June 2010 we minimized the stray light at detection photodiodes; after June 2010, we improved the contrast with the triple-pulse velocity selection, and we reduced the technical noise on photodiodes with an improved readout electronics. Finally, further improvements in the atom number and the implementation of new techniques such as the Coriolis compensation (see section 5.3.2) led to the current short term noise (August 2012)

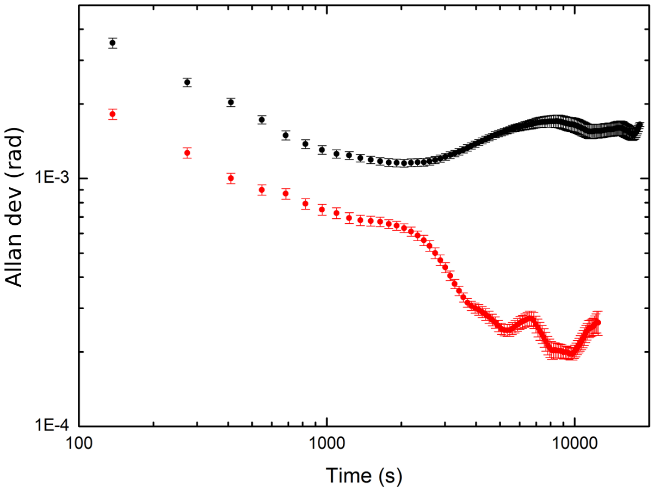

Figure 5.16: Allan deviation of ellipse phase angle; black curve: experimental data without active stabilization of most critical parameters; red curve: experimental data after the stabilization.

laser beams intensity ratio, current in the bias solenoid and MOT compensation coils, and tilt of the Raman mirror. However, noise in the coils current is fairly white, and would not entail the long term stability, while fluctuations in laser powers and mirror tilt exhibit a low frequency flickering.

As a test of the long term stability of our apparatus, we observe the statistical fluctuations of the gradiometer measurements over about 20 hours, keeping the source masses in a fixed position. At the same time we monitor the value of most relevant experimental parameters as well as the temperature in different points of the apparatus. We split the atom interferometer data into groups of 72 consecutive points, and obtain a value for Φ with its estimated error from each group by ellipse fitting. We then evaluate the Allan deviation of Φ; figure 5.16 (black trace) shows a typical Allan plot for a 20 hours long measurement. For integration times τ lower than $\sim$1800 s the Allan deviation scales as the inverse of the square root of τ. For longer times we observe a bump, indicating a slow fluctuation of the Φ value with a period of a few hours. The Φ data are well correlated with the temperature of the laboratory. Laser power and the Raman mirror tilt are also temperature correlated with correlation coefficients ranging from $\sim$0.7$\div$0.9.

Therefore, in order to improve the instrument stability, we chose to actively stabilize the most critical parameters, i.e. the MOT optical power, the probe optical power, acting in both the cases on the AOM RF power, and the Raman mirror tilt, acting on the piezo tip/tilt system (see section 5.3.2).

The impact of such upgrades is shown in figure 5.16 (red trace). The allan deviation decreases up to $\tau \sim 10000$ s reaching an error level of ~ 200 μrad, which is equivalent to a differential acceleration sensitivity of 5×10^{-11} g.

5.2 Measurement of gravity acceleration and gravity gradient

Absolute gravimeters generally require a high degree of isolation from vertical acceleration noise which, as a consequence of the equivalence principle, cannot be distinguished from gravity itself (see section 2.2.3). This is usually achieved with complex seismic isolation systems or can be rejected to some degree by calculating a correction from the reading of a mechanical accelerometer [59]. On the contrary, atom interferometry gravity gradiometers are highly immune from vibrations and seismic noise, which are efficiently rejected as common mode in the differential measurement when simultaneous interferometers are employed. However, in principle the use of a dual interferometer can help against seismic noise for gravity acceleration measurements too. In this section we show that simultaneous interferometers are more robust against seismic noise, in absolute gravity measurements, than single interferometers; as a result, we demonstrate a dual cloud atom interferometer providing at the same time an accurate measurement of gravity acceleration and of the vertical gravity gradient, without need of any seismic isolation or mechanical accelerometer.

5.2.1 Simultaneous interferometers

In a single Raman interferometer, the gravity induced phase ϕ_0 can be obtained by a sinusoidal fit on the interferometer fringe, as shown in figure 4.8. Such fitting function takes the form

$$x = A \sin(\phi_0 + \phi_L) + B \tag{5.8}$$

where x is the normalized level population, ϕ_L is the scanned relative phase of Raman lasers, A and B fringe amplitude and bias respectively. Fringe visibility is spoiled by seismic noise (figure

4.11) and thus a direct least-squares fit of measured points would clearly yield unreliable results in such conditions. When phase noise is large, but amplitude noise is small enough, it is useful to first determine the A and B by fitting the histogram $P(x)$ of measured data with the probability density function of a pure sine [60]

$$P(x) = \frac{1}{A\pi\sqrt{1-\left(\frac{B-x}{A}\right)^2}} \tag{5.9}$$

Then the interferometer phase ϕ_0 can be retrieved by fitting the experimental $\{x^i, \phi_L^i\}$ data to equation 5.8 with only ϕ_0 as a free parameter. Alternatively it is also possible to invert equation 5.8 to retrieve the phase ϕ^i of each individual measured point as

$$\phi^i = \arcsin\frac{x^i - B}{A} \tag{5.10}$$

and to obtain ϕ_0 from the histogram of calculated ϕ^i values. However, such algorithm is not able to solve the π phase ambiguity: points whose phase differs by integer multiples of π are folded in the $[-\frac{\pi}{2}, +\frac{\pi}{2}]$ interval.

In a gradiometer, two vertically separated light-pulse atom interferometers share the same pair of Raman lasers. For this reason, as explained in section 4.5.1, phases ϕ_x and ϕ_y of upper and lower interferometers are highly correlated, i.e. $\phi_y = \phi_x + \Phi$. Then, when the trace of the upper accelerometer is plotted as a function of the lower one experimental points $\{x^i, y^i\}$ distribute along a Lissajous ellipse (equation 4.5). Knowing ellipse parameters A, B, C, D and Φ, is possible to invert equation 4.5 to retrieve the actual phase ϕ^i of each individual measured point as

$$\begin{cases} \phi^i = \operatorname{arccot}\left(\frac{A(y^i-D)}{C(x^i-B)cos\Phi} - \tan\Phi\right) & x-B>0 \\ \phi^i = -\operatorname{arccot}\left(\frac{A(y^i-D)}{C(x^i-B)cos\Phi} - \tan\Phi\right) & x-B<0 \end{cases} \tag{5.11}$$

From the last formula is evident that the distribution of ϕ^i values is folded in the $[-\pi, +\pi]$ interval. As long as the RMS phase noise is not much higher than $\sim 2\pi$, the phase ϕ_0 and its standard error can be determined by direct fitting the ϕ^i counting histogram with a folded Gaussian function. From computational point of view, ellipse parameters and $\{\phi^i\}$ have been determined with a single least squares fit on the measured points. In the presence of large phase noise, the use of the dual interferometer offers two advantages. First, the phase distribution is determined over a range two times larger than with a single interferometer. Secondly, phase and amplitude noise act differently on the ellipse: the first spreads points along the curve profile while the second puts them out. This effect is enhanced when ellipse is well open, i.e. $\Phi \sim \frac{\pi}{2}$. The situation is different for the single fringe in which these two kinds of noise are strongly entangled and basically indistinguishable and, as a consequence, the retrieval fidelity of individual phases ϕ^i is quite poor at the edges of the measurement range; indeed, when the fringe derivative is small (i.e. with $\phi^i \sim \pi/2$), also a tiny amplitude noise can simulate the effect of a huge phase noise. This is not the case of simultaneous interferometers.

The last point is illustrated in figure 5.17 where we compare the reconstructed fringes obtained by the two methods. When setting the phase of the lower interferometer equal to that of the upper interferometer as calculated from equation 5.10, the fringe of lower interferometer is sensibly noisier around $\phi^i = \pm\frac{\pi}{2}$ than when using ellipse fitting.

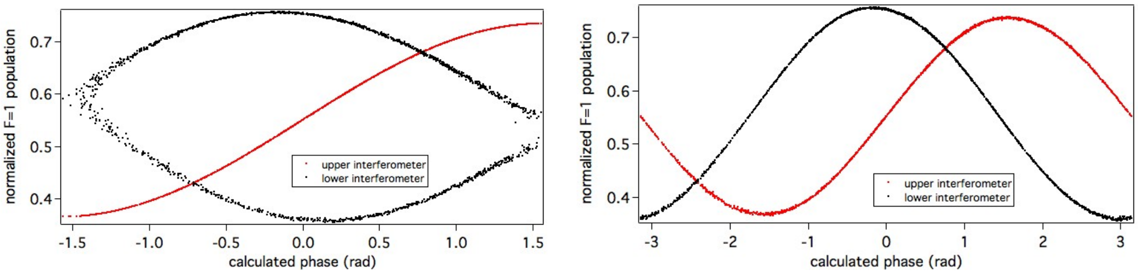

Figure 5.17: Reconstructed fringes for T = 160 ms: the normalized F=1 populations x^i (upper interferometer) and y^i (lower interferometer) are plotted versus the calculated phase ϕ^i using two different method. Left plot: the phase ϕ^i is computed from the upper fringe (red points) using equation 5.10. Afterwards, these values are used to plot the lower fringe (black points). It is evident how the amplitude noise is translated in phase noise around $\pm\frac{\pi}{2}$. Right plot: starting from the same data set, ϕ^i is computed from the upper fringe (red points) using the procedure explained in the text. Again, such values are used to plot the lower fringe (black points). Each fringe contains 1800 experimental points, and each point represents a single measurement.

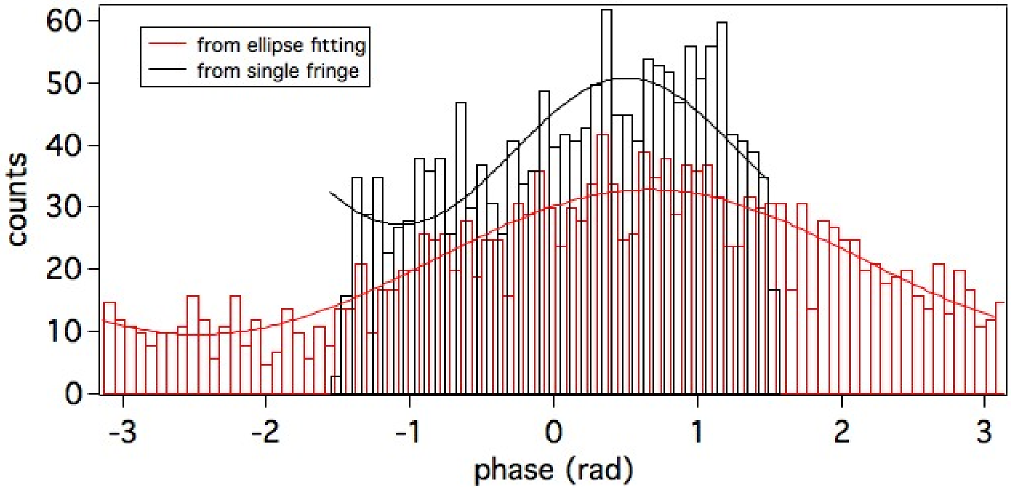

Figure 5.18: Counting histogram of 1800 ϕ^i values with T = 160 ms; ϕ^i values have been calculated through the single fringe equation 5.10 (in black) and using the ellipse procedure (in red); the solid lines represent least-squares fits with folded Gaussians.

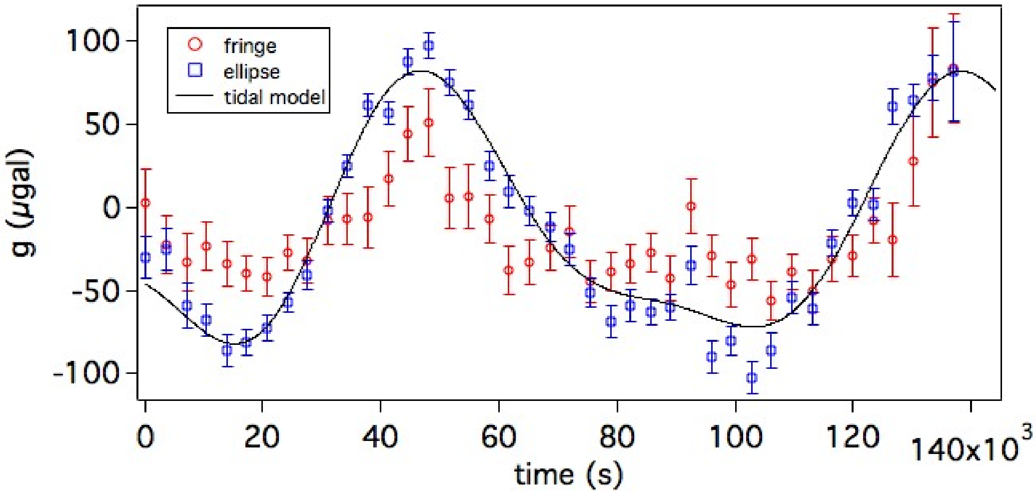

Figure 5.19: Variation of Earth's gravity as a function of the time. The continuous line corresponds to predicted Earth's tides.

5.2.2 Measurement of gravity acceleration and gradient

Figure 5.18 shows the histograms of data obtained from a single fringe and from ellipse fitting, corresponding to the fringes in figure 5.17. From each histogram we derive a value of g and its standard error.

In order to show the ability of this technique to measure the gravity acceleration, we recorded the dual interferometer output continuously for about two days. We calculated g from histograms every 1800 experimental points, i.e. about every hour. The resulting g temporal plot is shown in figure 5.19 compared to the output of a tidal prediction program. In the presence of large, seismically induced phase noise, the dual-cloud algorithm is still able to track the tidal gravity changes, while the performance is visibly worse with a single cloud. When comparing the two methods, the short-term sensitivity is a factor two better with ellipse fitting; however, when fitting the difference from tidal model with a constant, the RMS of residuals amount to ∼13 μgal and ∼36 μgal respectively, i.e. it is three times smaller with simultaneous interferometers than with single fringe. Using three ellipses with slightly different values of the interferometer time T , we derive an absolute value for the gravity acceleration $g = 9.804972 \pm 0.000079\ \mathrm{m/s^2}$, in good agreement with the value of about $9.80492048 \pm 0.00000003\ \mathrm{m/s^2}$ measured with a commercial FG5 gravimeter at the same location [61].

While reliable Gaussian fitting requires histograms with a large number of points, the temporal resolution can be much increased with a Bayesian estimator. Let us assume that the actual phase is normally distributed around the unknown value ϕ_0 with variance σ, and let us neglect the probability to fall outside the range $[-3\pi, +3\pi]$, while experimental points ϕ are folded in the $[-\pi,+\pi]$ interval; in order to determine ϕ_0 and its standard error we employ the Bayesian estimator

$$\hat{\phi}_o = \int\limits_{-\pi}^{+\pi} \frac{1}{\pi}\phi_0\, p(\{\phi^i\} \mid \phi_0)\, d\phi_0 \tag{5.12}$$

where the conditional probability density is given by

$$p(\{\phi^i\} \mid \phi_0) = N \sum_{n=-1}^{1} e^{-\frac{\sum_i (\phi_i - \phi_o - 2n\pi)^2}{2\sigma^2}} \tag{5.13}$$

and N is a normalization constant. With this technique we can obtain a single g value after recording ∼70 experimental points, i.e. after about three minutes. The Allan deviation of the difference between measured and predicted g values rolls off as 7×10^{-6} ms^{-2} / $\sqrt{\mathrm{Hz}}$ up to 90 minutes, reaching a level of about 13 μgal (see figure 5.20). The sensitivity is somehow limited by the repetition rate of the experimental sequence, which cannot be larger than 0.5 Hz due to geometrical constraints in our apparatus which is specifically designed for the G measurement. The sensitivity of differential gravity measurement, as obtained from the Allan deviation of Φ data, is about 9×10^{-8} ms^{-2} / $\sqrt{\mathrm{Hz}}$. From the measurement of Φ and of the clouds separation d, we derive the absolute value of the gravity gradient as $\gamma = \Phi / d k_{\mathrm{eff}} T^2$. We determine the contribution of magnetic field gradient due to the finite solenoid length (see section 5.1.2), which amounts to $(5.0 \pm 0.5) \times 10^{-8} s^{-2}$, by measuring the ellipse phase angle versus the applied bias field in the region of the atom interferometry sequence; after correcting for the gravity gradient produced by source masses, we obtain $\gamma = (3.135 \pm 0.007) \times 10^{-6} s^{-2}$, in fair agreement with the standard free-air value of $\gamma = 3.09 \times 10^{-6} s^{-2}$.

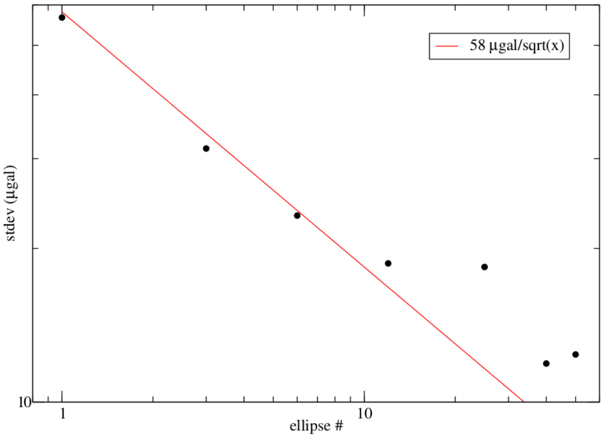

Figure 5.20: Allan deviation of the difference between predicted and measured g values reported in figure 5.19. Each ellipse corresponds to a measuring time of 134 seconds.

5.3 Measurement of G

In the previous sections of this chapter we demonstrated how the atomic trajectory can be accurately measured. We also described the long term behavior of the system, characterizing the responsivity of the instrument versus several parameters. In this final section a description of the experimental procedure for the G measurement is provided, together with a discussion of the systematic error sources.

5.3.1 General approach

One of the main goal of the MAGIA experiment is to achieve a perfect isolation of the effect of the gravitational field generated by source masses on the measured phase angle. The modulation of the source masses vertical position can produce a small alteration of the magnetic and mechanical setup of the experiment and, consequently, changes in the atomic clouds launch direction and magnetic field strength in the interferometer region. Such instabilities can seriously affect the measurement with additional phase shifts that are almost impossible to evaluate with the Monte Carlo simulation.

One of the possible ways to solve these systematic issues is to distinguish between k_{eff}-dependent and k_{eff}-independent effects. The effectiveness of such approach has been already experimentally demonstrated in the case of a single cloud interferometer [81]. In the following we will show how it can be easily implemented also in the MAGIA experiment.

Let us suppose to perform a gradiometer measurement in both the source masses configurations (C and F) using the k_{eff} vector with a certain orientation with respect to the gravity, labeled as "direct". The measured ellipse angles Φ can be written as

$$\begin{aligned} \Phi_C^{dir} &= \triangle_C + \alpha_C + \beta_C \\ \Phi_F^{dir} &= \triangle_F + \alpha_F + \beta_F \end{aligned} \tag{5.14}$$

Here in the $\triangle$ terms the gravity-induced phase shift has been isolated, while α and β terms represent the systematic shifts that are "even" and "odd" in k_{eff} respectively.

According to [81], among the even systematic sources we can mention the one-photon light shift and magnetic field gradients while, among the odd systematic sources, the two-photon light shift, wavefront aberrations and Coriolis acceleration.

We assume now to realize for both the atomic samples the scheme illustrated in figure 5.21, where a k_{eff}-inverted interferometer is perfectly overlapped with the direct one.

In this case the equation 5.14 can be rewritten in the following way:

$$\begin{aligned} \Phi_C^{inv} &= -\triangle_C + \alpha_C - \beta_C \\ \Phi_F^{inv} &= -\triangle_F + \alpha_F - \beta_F \end{aligned} \tag{5.15}$$

where the k_{eff}-even terms did not changed sign. Combining these last expressions we can define two new quantities:

$$\begin{aligned} \triangle\Phi_{tot} = \Phi_C^{dir} - \Phi_F^{dir} - (\Phi_C^{inv} - \Phi_F^{inv}) = 2 * (\triangle_C - \triangle_F) + 2 * (\beta_C - \beta_F) \\ \Xi = \Phi_C^{dir} + \Phi_C^{inv} - (\Phi_F^{dir} + \Phi_F^{inv}) = 2 * (\alpha_C - \alpha_F) \end{aligned} \tag{5.16}$$

We can observe that in $\triangle\Phi_{tot}$ the k_{eff}-even terms variation Ξ has been rejected, leaving only the k_{eff}-odd terms as unique systematic error source.

Experimentally, the vertical superposition can be obtained by properly adjusting the Raman frequency ramp and the timing of the velocity selection. Following the procedure described in

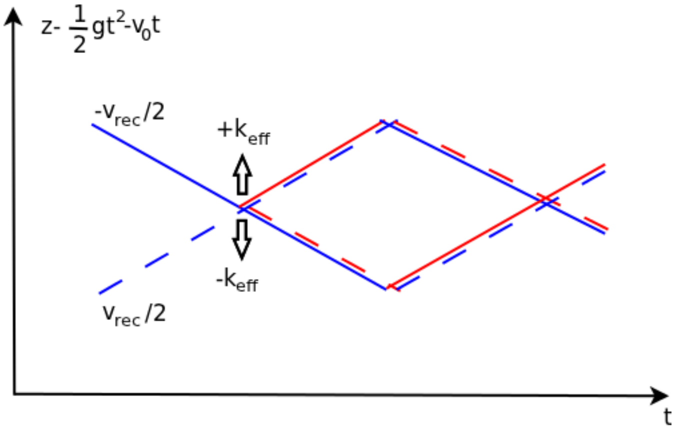

Figure 5.21: Overlapped interferometer scheme. The solid lines describe the direct interferometer ($+k_{\text{eff}}$) while dashed lines the inverted one ($+k_{\text{eff}}$). The F=1 state is indicated in blue, while the F=2 state in red.

section 5.1.1, a vertical displacement of only ~300 μm between direct and inverted interferometers has been measured. The horizontal overlap is ensured by using the same launch sequence.

5.3.2 Coriolis compensation

The Coriolis force caused by Earth's rotation has long been known to cause systematic effects. Small variations of the horizontal velocity can indeed produce phase shifts of several mrad. Recently the use of a tip-tilt Raman mirror system for Large Momentum Transfer (LMT) interferometers [54, 82] has been demonstrated to be one of the most promising technique to perform a first order Coriolis effect compensation. For these reasons, we decided to implement it also in our apparatus.

The principle of operation of the tip-tilt mirror is as follows: the moving standing wave formed by the two contra-propagating Raman beams is aligned vertically in the direction of local gravity. In the ideal situation, the light pulses would all propagate along the same vertical axis. Unfortunately, the rotation of the lab frame due to Earth's rotation during the free fall time produces also the rotation of the Raman beams axis with respect to the original vertical direction. This has two effects: a systematic offset in the measurement because the atoms free fall trajectory and the Raman axis do not coincide throughout the measurement; a loss of fringe contrast and a concomitant loss of precision because the atomic wave packets do not overlap properly. However, in order to counteract Earth's rotation, it is possible to rotate the retro-reflection Raman mirror that provides the counter-propagating Raman beam scheme. The momentum transferred in the mirror and beam splitter operations, as seen from the atom's inertial frame, is now in a constant direction, and is parallel to the direction of gravity at the initial point, despite Earth's rotation.

The impact of Coriolis compensation on the ellipse contrast is shown in figure 5.22. Figure 5.23, left, shows the contrast as a function of the tip-tilt rotation vector $\vec{\Omega}$ directed along the North-South (red trace) and East-West (blue trace) direction. According to [54], we expect a maximum of the ellipse contrast at the Coriolis compensation point, i.e. $\Omega_{ns} = 50.7$ μrad/s and $\Omega_{ew} = 0$ μrad/s. By a parabolic fit of the experimental data we obtained instead $\Omega_{ns} = 48 \pm 5$ μrad/s and $\Omega_{ew} = 10 \pm 1$

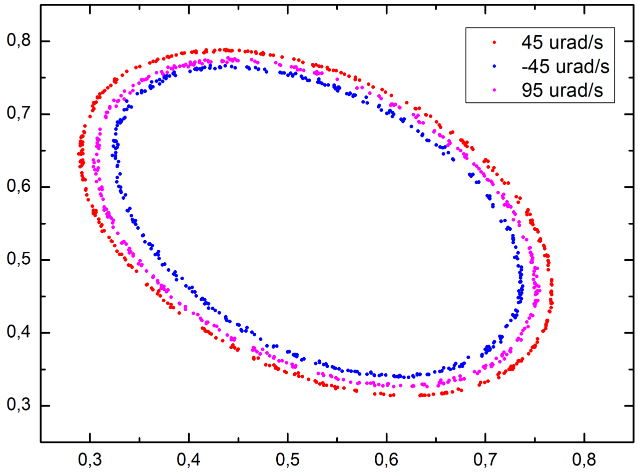

Figure 5.22: Raw data at different tip-tilt mirror rotation rate Ω. Small contrast modulations ($\sim 13\%$ for $\Delta\Omega = 90$ μrad/s) are visible.

μrad/s, in reasonable agreement with the expected values if we consider that our piezo actuators are not hysteresis-compensated and thus some nonlinearity can affect the measurement. Figure 5.23, right, shows the related trend of the ellipse fit errors. It is interesting to notice that around the Coriolis compensation point, a sensitivity improvement of 30% with respect to the fixed mirror condition has been found. This effect can not be attributed to the higher contrast (only 4% more) but to an effective decrement of the ellipse RMS noise.

The tip-tilt mirror system provides also a powerful tool to investigate systematic error sources otherwise difficult to evaluate. According with the equation 2.85, the Coriolis phase shift β_{coriol} for an atom gravity gradiometer, in presence of an additional rotation $\vec{\Omega}$, can be written as

$$\beta_{coriol} = -2k_{\text{eff}}T^2[(\Omega_{ns} + \Omega_{coriol})\triangle v_{ew} + \Omega_{ew}\triangle v_{ns}] \tag{5.17}$$

where $\triangle v_{ew}$ and $\triangle v_{ns}$ are the projections on the North-South and East-West direction of the horizontal velocity difference between upper and lower atomic clouds. Therefore, varying the angular velocity and looking at the quantity $(\Phi_{dir} - \Phi_{inv})/2 = \triangle + \beta$, it will be possible to retrieve the horizontal velocity difference through linear regression. Figure 5.24 illustrates the results of such procedure in the case $\triangle v_{ew}$ for both the source masses configuration, in order to detect possible trajectory changes. Every point corresponds to 720 measurement cycles, inverting k_{eff} every shot.

The following results has been obtained: $\triangle v_{ew}^C = (0.221 \pm 0.009)$ mm/s and $\triangle v_{ew}^F = (0.238 \pm 0.006)$ mm/s. These two values do not differ significantly and thus we can conclude that the source masses modulation does not introduce any significant modification in the launch. However, with $\triangle(\triangle v_{ew}) = 17$ μm/s and supposing a rough Coriolis compensation at 10% level, a conservative estimate of the Coriolis systematic shift should be ~ 70 μrad ($\sim 1.2 \times 10^{-4}G$). Similar results were also found for the normal component. Currently we are installing a new piezo system with strain gauge controller for hysteresis corrections, in order to perform a reliable Coriolis compensation at 1% level.

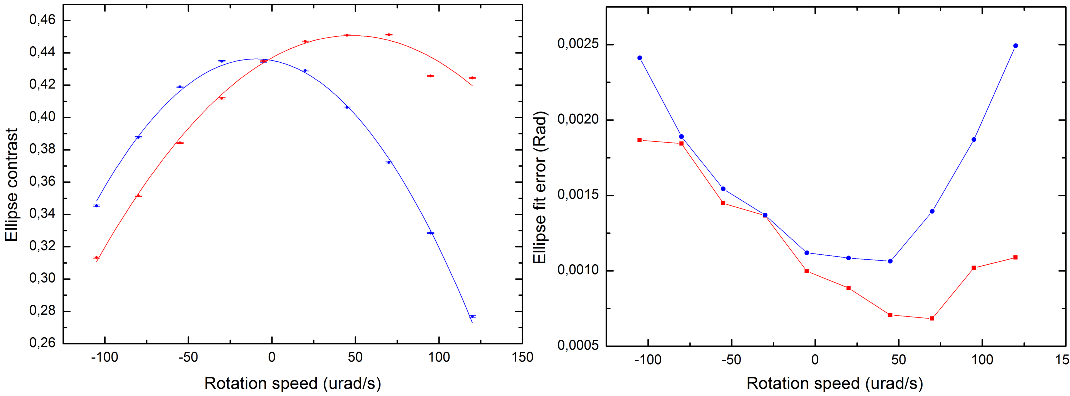

Figure 5.23: Left: contrast versus tip-tilt mirror rotation rate. The red trace has been taken with the rotation vector $\vec{\Omega}$ directed along the North-South direction, the blue trace with $\vec{\Omega}$ along the East-West direction; Right: related ellipse fit errors. Each point corresponds to 360 measurements.

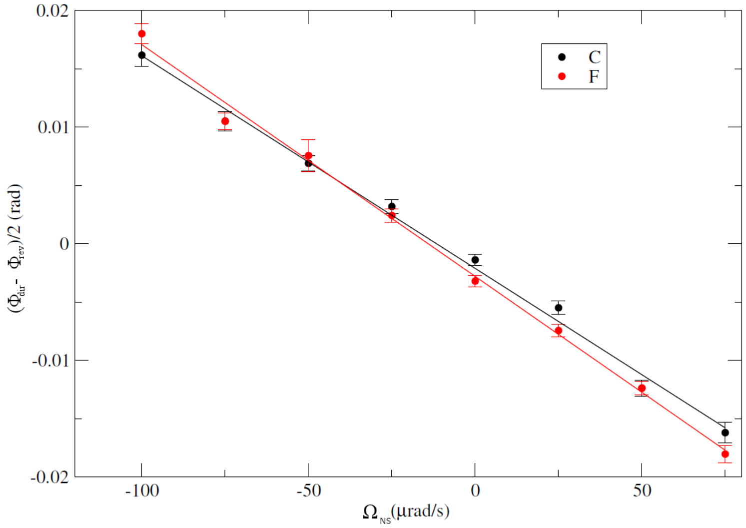

Figure 5.24: k_{eff}-direct and k_{eff}-inverted ellipse angle semi-difference as a function of the mirror rotation rate Ω_{ns}. Red points have been taken in Far source masses configuration, black points in Close configuration. The average values of $(\Phi_{dir} - \Phi_{inv})/2$ have been subtracted in both cases. Linear fits are also shown.

5.3.3 Preliminary measurement

Meanwhile a preliminary G measurement has also been performed.

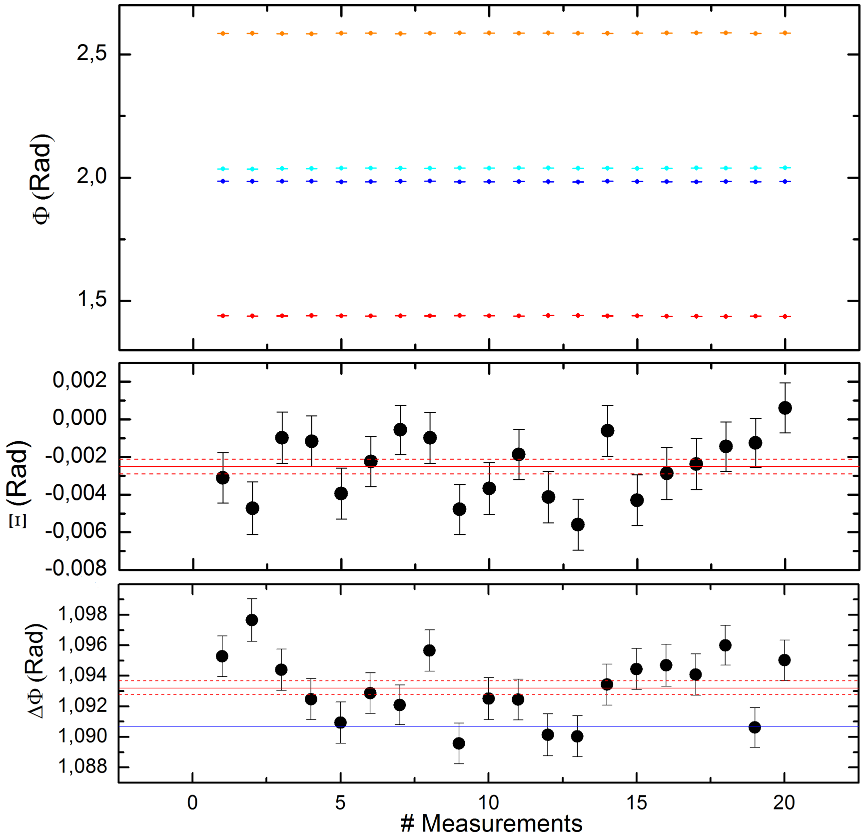

Figure 5.25: Top: Modulation of the differential phase shift measured by the atomic gravity gradiometer when the distribution of the source masses and the k_{eff} direction are alternated. Blue and light blue points have been taken in C configuration with direct and inverted k_{eff} orientation respectively; Red and orange points have been taken in F configuration with direct and inverted k_{eff} orientation respectively. Each point has been obtained by a single elliptical fit on experimental data. Center: Resulting values of the angle Ξ^i; solid red line indicates the mean value with the statistical error (dashed lines); Bottom: Resulting values of the angle $\triangle\Phi^i_{tot}$; solid red line indicates the mean value with the statistical error (dashed lines), purple line represents the simulation result for the single particle.

Figure 5.25 shows a measurement of the differential interferometric phase $\Delta\Phi_{tot}$ over a period of 20 hours. We moved the source masses from the close (C) to the far (F) configuration and vice versa every 30 min alternating the k_{eff} vector at each measurement cycle (~2 s) and collecting 360 experimental points in each k_{eff} orientation. The modulation time has been chosen in order to complete a C-F-C sequence before long-term drifts appear (see section 5.1.3). Each data set has been fitted with a single ellipse in order to retrieve the four quantities $\Phi_C^{dir,i}$, $\Phi_C^{inv,i}$, $\Phi_F^{dir,i}$ and $\Phi_F^{inv,i}$

SOURCE	Uncertainty	$\Delta G/G\,(10^{-4})$	Status
Cylinders radial positioning	10 μm	0.5	Done
Cylinder shape	10 μm	$\ll 1$	Done
Cylinder mass	10 mg	$\ll 1$	Done
Density radial homogeneity	2×10^{-3}	0.01	Done
Density vertical homogeneity	0.5×10^{-3}	0.2	Done
Support platform mass	60 g	0.8	To be improved
Cloud-Masses vertical distance	100 μm	0.02	Done
Cloud-Masses horiz. distance	100 μm	N/A	Partially done
Atomic horiz. distribution	100 μm	N/A	Partially done
Launch direction C/F	6 μrad	1.2	Done
Raman mirror tilt C/F	0.1 μrad	0.3	Done

Table 5.4: Present error budget of the G measurement.

and thus evaluate the two angles $\Delta\Phi^i_{tot}$ and Ξ^i, as defined in section 5.3.1. The optical power of the cooling and probe lasers has been actively stabilized throughout the measurement, as well as the absolute tilt of the Raman mirror after each source masses movement. Moreover, during the interferometric sequence, we acted on the tip-tilt Raman mirror in order to properly perform the Coriolis compensation. At the end of the run we also performed a full trajectory characterization, using the procedure described in section 5.1.1.

The obtained experimental values are $\Delta\Phi^i_{tot} = (1.0932 \pm 0.0005)$ rad, equivalent to a sensitivity on G of 4.6×10^{-4} in 20 hours of integration time, and $\Xi = (-0.0025 \pm 0.0004)$ rad. The latter is a strong indication that $\alpha_C \neq \alpha_F$, namely that the source masses modulation introduces a k_{eff}-even phase shift, presumably of magnetic origin.

By comparison with the simulated value ($\triangle\Phi_s = 1.0907$ rad), obtained using the last CODATA G value and supposing point like clouds moving along the system symmetry axis, the measured value is (2.5 ± 0.5) mrad higher, corresponding to a relative shift on G of 2.3×10^{-3} with respect to the CODATA value. Such discrepancy can be principally ascribed to clouds size effects and finite size of the detection region. Regarding the first point we are currently running a full MonteCarlo simulation of the experiment using the trajectory data as input parameters; regarding the second point, we are preparing a detection region mapping and resizing, in order to exclude from phase shift computation atoms that fall out from it.

Finally in table 5.4 an error budget summary is reported, showing, for each source of systematic error, the current status on the experiment.

Chapter 6

Conclusions and perspectives

The aim of this work was to optimize and carefully characterize a cold atom gradiometer in order to perform precision gravity measurements, paying particular attention to the determination of the gravitational constant G.

During the first year the experimental apparatus was updated, introducing a high flux atomic source (2D-MOT) and a new Raman laser system. Sensitivity and stability of the instrument have been carefully measured [34], in order to evaluate quantitatively the effect of these two modules on the system.

The second year was dedicated mainly to further enhance the short term stability, reducing the detection technical noise and optimizing the state preparation procedure. A complete source masses characterization was also performed: shape and position of each tungsten cylinder was accurately measured with an uncertainty below 10 μm, while mass was determined to better than 10 mg. Systematic shifts on G due to positioning resolution and weighting resolution were evaluated by simulation.

In the third and fourth years many efforts were put on the characterization of the atomic trajectories of the cold fountain, developing a procedure that allows to determine clouds barycenter and width with sub-millimeter accuracy. Influence of the several experimental parameters on the gradiometer phase was also investigated, in order to identify the main sources of instabilities. In parallel, an alternative method to measure simultaneously the absolute gravity acceleration and the gravity gradient was demonstrated [88], reaching a sensitivity on g of 7×10^{-6} ms^{-2} / $\sqrt{\text{Hz}}$ without the aid of any seismic noise rejection system. Such results can have interesting implications both in geophysical applications and in fundamental physics, where advanced schemes for large-area atom interferometry can be seriously limited by seismic and vibration noise [55]. Finally, a preliminary measure of G was performed in order to test sensitivity and accuracy of the instrument. A final sensitivity to the gravity gradient of $\sim 5 \times 10^{-9}\text{g}/\sqrt{\text{Hz}}$ has been reached.

Further studies are needed to improve the actual knowledge of systematics; in particular, a spatial characterization of the detection region is required to precisely define which atoms are detected. Only at this stage a complete simulation of the experiment at 10^{-4} level and a reliable comparison with experimental data will be possible.

Concerning future developments, we can recognize two different paths: realization of transportable devices or taking advantage of the atomic sensors to implement other precise measurements of fundamental physics.

Transportable atom gravimeters show several advantages with respect to classical instrument used in Earth science and Geophysics: indeed, the possibility to perform absolute gravity measurements at high precision level directly *in situ* is looked with great interest. Atom based devices could be suitable also for orientation in navigation and could also be installed on space vehicles to perform precision measurements in microgravity environment [63]. From a technological point of view, building new transportable devices implies a remarkable efforts in the compactification of optical and electronic systems as well as in the development of robust laser locks [66].

The other research line is more related with fundamental physics and precision measurements. In order to further increase atom interferometry sensitivity several large area atom interferometer schemes based on multiphoton transitions were recently demonstrated [8, 55]. Such new solutions open the possibility, in the near future, to realize new general relativity tests [9] and, on the long term, to detect gravitational waves [64, 65]. Recently, a new description of atom interferometry in terms of atoms ticking at the Compton frequency (and thus sensitive to the gravitational potential) led to an intense debate about the possibility to reinterpretate old experiments as sensitive test of gravitational redshift [75, 74]. To solve this open question, a new experimental scheme has been proposed [76]. Following this concept, the MAGIA apparatus can be, in principle, re-adapted to fit the requirements for such kind of experiment. On the other hand, a great interest is also preserved for gravity measurements at short distances: the MAGIA apparatus is particular suitable for an accurate test of the $1/r^2$ law over the distance scale of ~ 1 cm.

Appendix A

Rubidium Data

This appendix will provide information about D_2 transition of ^{87}Rb atom. Figures A.2 and A.3 show a scheme of ^{85}Rb and ^{87}Rb energy levels, with information regarding transition frequencies and Landè factors g_F. In addition, is possible to see also the corresponding Sub-Doppler saturation spectroscopy signals. The spectroscopy setup with counter-propagating pump and probe beams enables so called Cross-Over (CO) transitions: atoms that have a certain velocity along the propagation axis of the beams will experience a Doppler shift of the light. If pump and probe beams are counter-propagating, their frequencies will be Doppler-shifted by the same amount but to opposite directions in the reference system of the atom. If such the laser frequency is centered between two transition frequencies, atoms of the right velocity class may absorb photons of both beams, each on another transition. Our notation is the following: transition $F = A \leftrightarrow F' = B$ is called A-B and crossover transitions in resonance with $F = A \leftrightarrow F' = B$ and $F = A \leftrightarrow F' = C$ are called CO A-BC. Table A.1 contains some general ^{87}Rb physical properties, while in table A.2 more specific information on D_2 are reported. Data have been taken from [53]. Finally, a scheme containing all the probabilities of the $5^2S_{1/2}$-$5^2P_{3/2}$ transitions among different hyperfine magnetic sublevel is also included. (see figure A.1).

Atomic number	Z	37
Number of nucleons	$Z+N$	87
Nuclear spin	I	3/2
Relative natural abundance	$\eta(^{87}Rb)$	27.83(2)%
Nuclear lifetime	τ_n	4.88×10^{10} years
Vapor pressure @ 25°C	P_v	3.0×10^{-7} torr
Atomic mass	m	$1.44316060(11)\times10^{-25}$ Kg
Ground state hyperf. splitting	ν_{ab}	6.834 682 610 90429(9) GHz
D_2 dipole matrix element	$\left\langle J=\frac{1}{2} \middle\| er \middle\| J'=\frac{3}{2}\right\rangle$	$3.584(4)\times10^{-29}$ C m
D_1 dipole matrix element	$\left\langle J=\frac{1}{2} \middle\| er \middle\| J'=\frac{1}{2}\right\rangle$	$2.537(3)\times10^{-29}$ C m

Table A.1: ^{87}Rb physical parameters

Frequency	$\nu_{2\rightarrow 3}$	384.2281152033(77) THz
Transition energy	$h\nu_{2\rightarrow 3}$	1.589049439(58) eV 2.5459376×10^{-19} J
Wavelength (Vacuum)	λ_{vac}	780.241209686(13) nm
Wavelength (Air)	λ	780.03200 nm
Wavevector (Vacuum)	k	8052875.481555 m^{-1}
Lifetime	τ	26.24(4) ns
Natural linewidth (FWHM)	Γ	$2\pi\cdot 6.065(9)$ MHz
Saturation intensity	I_0	1.67 $\mathrm{mW/cm}^2$
Recoil velocity	v_r	5.8845 mm/s
Recoil temperature	T_r	361.96 nK
Recoil frequency	ν_r	3.7710 kHz
Recoil energy	E_r	2.499×10^{-30} J 1.56×10^{-11} eV
Doppler temperature	T_D	146 μK
II order Zeeman shift (m_F =0)	$a_{Z,II}$	575.15 $\mathrm{Hz/G}^2$

Table A.2: Specific rubidium data relative to the D_2 transition of ^{87}Rb.

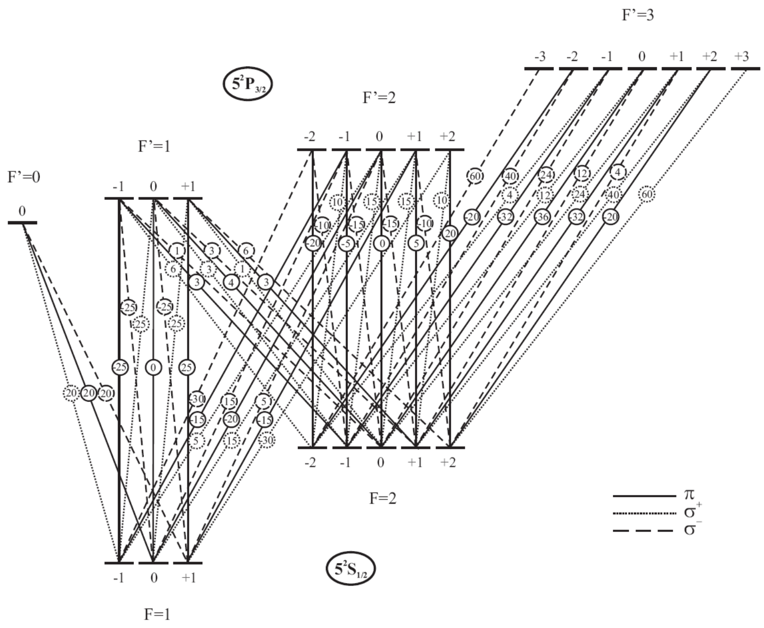

Figure A.1: The two ground state and the four hyperfine levels of $5^2P_{3/2}$ together with all the relative magnetic sublevels are indicated. The number in the circles indicate the transition strength multiplied by 120. ±N stands for a Clebsch Gordan coefficient equal to$\pm\sqrt{\frac{N}{120}}$.

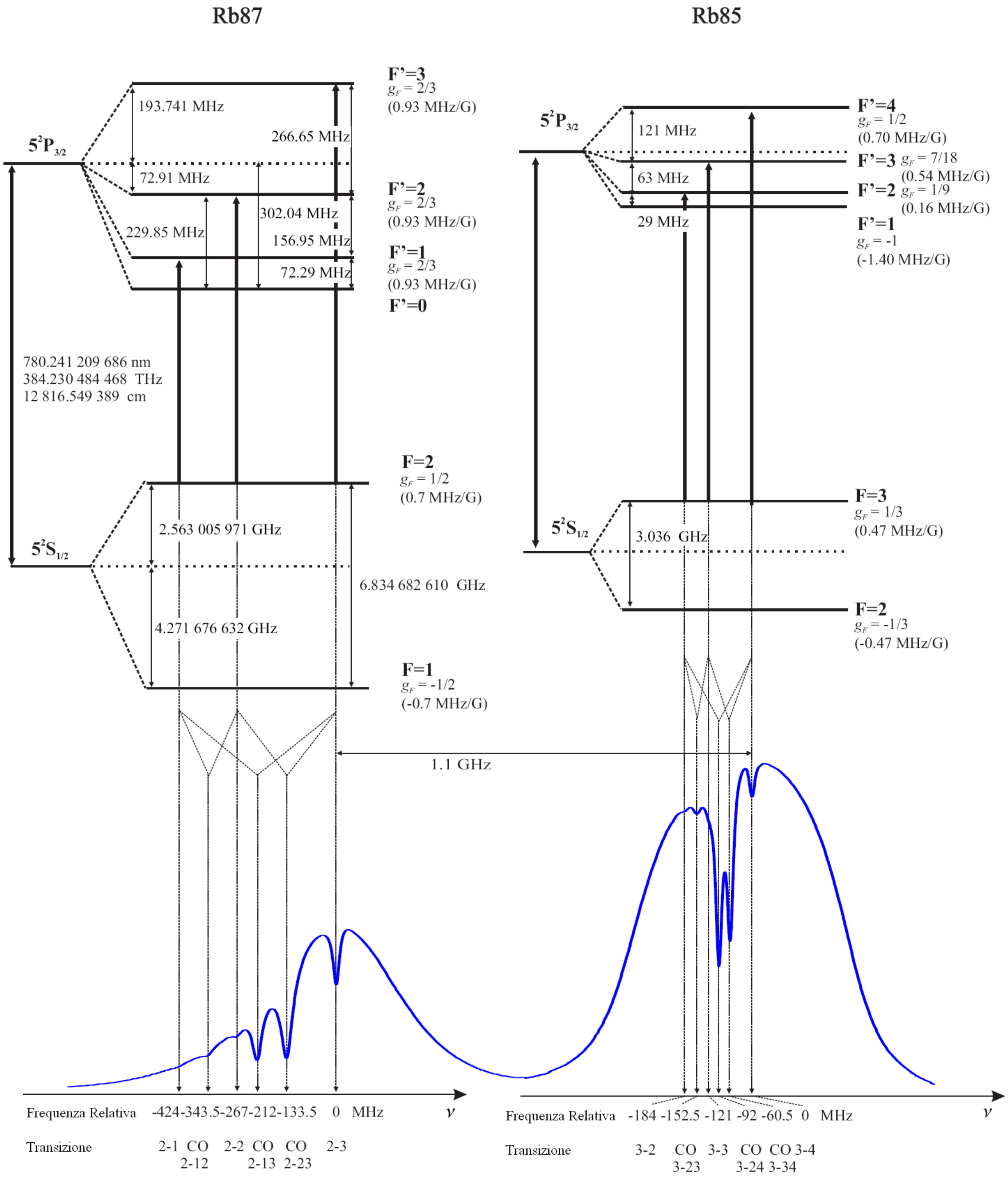

Figure A.2: Rubidium D_2 transitions from the upper hyperfine-level of the ground state. Indicated are transition frequencies, information about the levels and below the corresponding saturated absorption spectroscopy signal. The indications for the Zeeman shift need to be multiplied by the m_F quantum number.

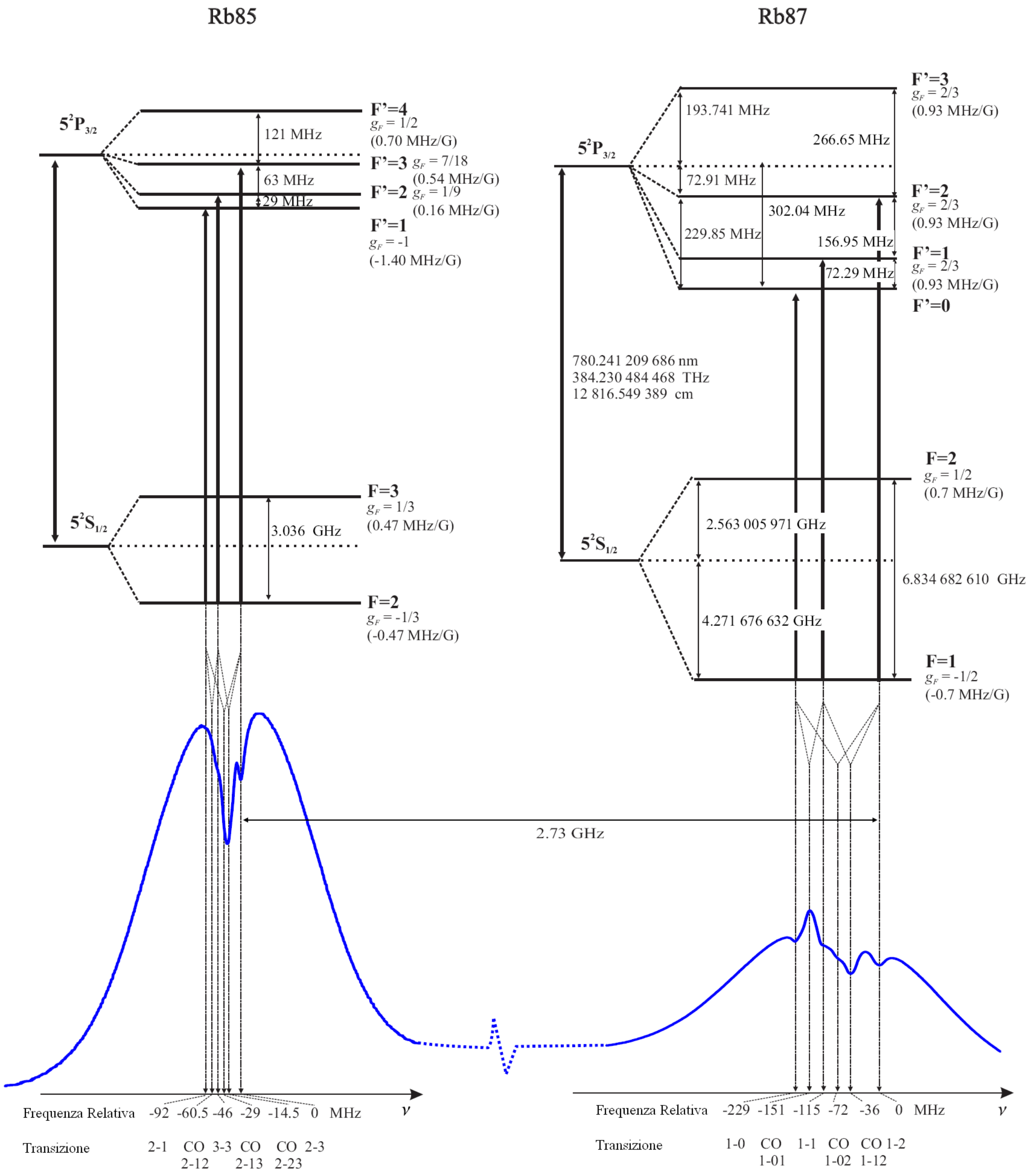

Figure A.3: Rubidium D_2 transitions from the lower hyperfine-level of the ground state. Indicated are transition frequencies, information about the levels and below the corresponding saturated absorption spectroscopy signal.

Bibliography

[1] A. Peters, K. Y. Chung, and S. Chu, *Measurement of the gravitational acceleration by dropping atoms, Nature*, **400**, 849-852 (1999).

[2] A. D. Cronin, J. Schmiedmayer and D. E. Pritchard, *Optics and interferometry with atoms and molecules*, Rev. Mod. Phys. **81**, 1051–1129 (2009)

[3] J. M. McGuirk, G. T. Foster, J. B. Fixler, M. J. Snadden and M. A. Kasevich, *Sensitive absolute-gravity gradiometry using atom interferometry*, Physical Review A (atomic, Molecular and Optical Physics), **65**, 33-60 (2002).

[4] G. Lamporesi, A. Bertoldi, L. Cacciapuoti, M. Prevedelli and G.M. Tino, *Determination of the Newtonian Gravitational Constant Using Atom Interferometry*, Phys. Rev. Lett., **100**, 050801 (2008).

[5] T. L. Gustavson et al., *Rotation sensing with a dual atom interferometer Sagnac gyroscope*, Class. Quantum Grav., **17**, 2385 (2000).

[6] A. Peters, K. Y. Chung and S. Chu, *High-precision gravity measurements using atom interferometry*, Metrologia, **38**, 25-61 (2001).

[7] A. Bresson, Y. Bidel, P. Bouyer, B. Leone, E. Murphy, and P. Silvestrin, *Quantum mechanics for space applications*, Appl. Phys. B, **84**, 545-550, (2006).

[8] H. Müller, S.-W. Chiow, Q. Long, S. Herrmann, and S. Chu, *Atom Interferometry with up to 24-Photon-Momentum-Transfer Beam Splitters*, Phys. Rev. Lett. **100**, 180405 (2008).

[9] S. Dimopoulos, P. W. Graham, J. M. Hogan, and M. A. Kasevich, *Testing General Relativity with Atom Interferometry*, Phys. Rev. Lett., **98**, 111102 (2007).

[10] E. Fermi and L. Marshall, *Interference Phenomena of slow neutrons*, Phys. Rev. **71**, 666 (1947).

[11] L. Marton, Electron interferometer, Phys. Rev. **85**, 1057 (1952).

[12] O. Carnal and J. Mlynek, *Youngs double-slit experiment with atoms: A simple atom interferometer*, Phys. Rev. Lett. **66**, 2689-2692 (1991).

[13] D. W. Keith, Ch. R. Ekstrom, Q. A. Turchette and D. E. Pritchard, *An interferometer for atoms,* Phys. Rev. Lett. **66**, 2693-2696 (1991).

[14] F. Riehle, Th. Kisters, A. Witte, J. Helmcke and Ch. J. Bordè, *Optical Ramsey spectroscopy in a rotating frame: Sagnac effect in a matter-wave interferometer*, Phys. Rev. Lett. **67**, 177-180 (1991).

[15] M. Kasevich and S. Chu, *Atomic Interferometry Using Stimulated Raman Transitions*, Phys. Rev. Lett., **67**, 2 (1991).

[16] K. Moler et al., *Theoretical analysis of velocity-selective Raman transitions*, Phys. Rev. A, **45**, 342-348 (1992).

[17] M.J. Snadden, J.M. McGuirk, P. Bouyer, K.G. Haritos and M.A. Kasevich, *Measurement of the Earth's Gravity Gradient with an Atom Interferometer-Based Gravity Gradiometer*, Phys. Rev. Lett**.**, **81**, 971 (1998).

[18] J. M. McGuirk, G. T. Foster, J. B. Fixler, M. J. Snadden and M. A. Kasevich, *Sensitive absolute-gravity gradiometry using atom interferometry*, Phys. Rev. A, **65**, 033608 (2002).

[19] T.L. Gustavson, A. Landragin and M.A. Kasevich, *Rotation sensing with a dual atom-interferometer Sagnac gyroscope*, Class. Quantum Grav., **17**, 2385 (2000).

[20] Ch. Jentsch, PhD Thesis, Konzeption und Aufbau ... Inertialsensorik mit lasergekuhlten Rubidiumatomen, Cuvillier Verlag Gottingen (2004).

[21] F. Yver-Leduc, P. Cheinet, G. Fils, A. Clairon, N. Dimarcq, D. Holleville, P. Bouyer and A. Landragin, *Reaching the quantum noise limit in a high-sensitivity cold-atom inertial sensor*, J. Optics B, Quant. Semiclass. Opt., **5**, 136 (2003).

[22] G. Lamporesi, A. Bertoldi, L. Cacciapuoti, M. Prevedelli and G. M. Tino, *Determination of the Newtonian gravitational constant using atom interferometry*, Phys. Rev. Lett. **100**, 050801 (2008).

[23] H. Cavendish, Experiments to determine the density of the earth, Phil. Trans. R. Soc. **88**, 469 (1798).

[24] J. H. Gundlach and S. M. Merkovitz, *Measurement of Newton's Constant Using a Torsion Balance with Angular Acceleration Feedback*, Phys. Rev. Lett. **85**, 2869 (2000).

[25] C. H. Bagley and G. G. Luther, *Preliminary Results of a Determination of the Newtonian Constant of Gravitation: A Test of the Kuroda Hypothesys*, Phys. Rev. Lett. **78**, 3047 (1997).

[26] T. J. Quinn, C. C. Speake, S. J. Richman, R. S. Davis and A. Picard, *A New Determination of G Using Two Methods*, Phys. Rev. Lett. **87**, 111101 (2001).

[27] U. Kleinevoss, Bestimmung der Newtonschen Gravitationskonstanten G, PhD thesis, Universität Wuppertal, 2002.

[28] S. Schlamminger, E. Holzschuh and W. Kündig, *Determination of the Gravitational Constant with a Beam Balance*, Phys. Rev. Lett. **89**, 161102 (2002).

[29] T. R. Armstrong and M. P. Fitzgerald, *New Measurements of G Using the Measurement Standards Laboratory Torsion Balance*, Phys. Rev. Lett. **91**, 201101 (2003).

[30] J. Luo, Z. K. Hu, X. H. Fu and S. H. Fan, *Determination of the Newtonian gravitational constant G with a nonlinear fitting method*, Phys. Rev. D **59**, 042001 (1998).

[31] Luo J, Liu Q, Tu LC, Shao CG, Liu LX, Yang SQ, Li Q and Zhang YT, *Determination of the Newtonian gravitational constant G with time-of-swing method,* Phys. Rev. Lett. **98**, 111102 (2009).

[32] Harold V. Parks and James E. Faller, *Simple Pendulum Determination of the Gravitational Constant,* Phys. Rev. Lett. **105**, 110801 (2010).

[33] J.P. Schwarz, D.S. Robertson, T.M. Niebauer and J.E. Faller, *A Free-Fall Determination of the Newtonian Constant of Gravity Science*, 282, 2230 (1998).

[34] F. Sorrentino, Y. Lien, G. Rosi, L. Cacciapuoti, M. Prevedelli and G. M. Tino, *Sensitive gravity-gradiometry with atom interferometry: progress towards an improved determination of the gravitational constant*, New Journal Physics **12**, 095009 1-17 (2010).

[35] R. Legere and K. Gibble, *Quantum Scattering in a Juggling Atomic Fountain*,Phys. Rev. Lett. 81, 5780 (1998).

[36] G. T. Foster, J. B. Fixler, J. M. McGuirk, and M. A. Kasevich, *Method of phase extraction between coupled atom interferometers using ellipse-specific fitting*, Opt. Lett. 27 (2002).

[37] M. Kasevich and S. Chu, *Measurement of the gravitational acceleration of an atom with a lightpulse atom interferometry*, Applied Physics B, **54**, 321-332 (1992).

[38] P. Cheinet, *Conception et Réalisation d'un Gravimètre à Atomes Froids,* PHD thesis, Paris 6 University (2006).

[39] C. J. Bordé, *Atomic interferometry with internal state labelling*, Physics Letters A, **140**, 10-12 (1989).

[40] A. Peters, *High precision gravity measurements using atom interferometry*, PHD thesis, Standford University (1998).

[41] P. Cheinet, B. Canuel, F. P. D Santos, A. Gauguet, F. Lenduc e A. Landragen, *Measurement of the sensitivity function in time-domain atomic interferometer*, IEEE Trans. on Instrum. Meas. (2005).

[42] D. W. Allan, *Statistic of atomic frequency standards*, In Proceedings IEEE, **54**, 221 (1966).

[43] G. Lamporesi, *Determination of the gravitational constant by atom interferometry*, PHD thesis, Florence University (2006).

[44] T. Petelski, *Atom interferometers for precision gravity measurements*, PHD thesis, Paris 6 University (2005).

[45] A. L. Schawlow e C. H. Townes, *Infrared and optical masers*, Physical Review, **112**, 1940–1949 (1958).

[46] M. Schmidt, M. Prevedelli, A. Giorgini, G. M. Tino and A. Peters *A portable laser system for high-precision atom interferometry experiments*, Applied Physics B, **102**, 11-18 (2011).

[47] E. Riis, D. S. Weiss, K. A. Moler and S. Chu *Atom funnel for the production of a slow, high-density atomic beam,* Phys. Rev. Lett. **64** 1658 (1990).

[48] K. Dieckmann, R. J. C. Spreeuw, M. Weidemüller and J. T. M. Walraven, *Two-dimensional magneto-optical trap as a source of slow atoms* Phys. Rev. A **58** 3891 (1998).

[49] E. L. Raab, M. Prentiss, A. Cable, S. Chu, and D. E. Pritchard, *Trapping of neutral sodium atoms with radiation pressure*, Phys. Rev. Lett. **59**, 2631 (1987).

[50] J. Dalibard and C. Cohen-Tannoudji, *Laser cooling below the Doppler limit by polarization gradients: simple theoretical models*, J. Opt. Soc. Am. B **6**, 2023 (1989).

[51] J. Stockton, X. Wu and M. A. Kasevich, *Bayesian estimation of differential interferometer phase* Phys. Rev. A **76** 033613 (2007).

[52] G. Lamporesi, A. Bertoldiand, A. Cecchetti, B. Dulach, M. Fattori, A. Malengo, S. Pettorruso, M. Prevedelli and G. M. Tino *Source Masses and Positioning System for an Accurate Measurement of G,* Rev. Sci. Instrum. **78**, 075109 (2007).

[53] D. A. Steck, *Rubidium 87 D line data* (Disponibile online all'indirizzo: http://steck.us/alkalidata).

[54] S.-Y. Lan, P.-C. Kuan, B. Estey, P. Haslinger and Holger Müller, *Influence of the Coriolis Force in Atom Interferometry*, Phys. Rev. Lett. **108**, 090402 (2012).

[55] S.-w. Chiow, T. Kovachy, H.-C. Chien and Mark A. Kasevich, *102$\hbar k$ Large Area Atom Interferometers*, Phys. Rev. Lett. **107**, 130403 (2011).

[56] A. Giorgini, *Development of a transportable atom interferometer operating as inertial and gravity sensor*, PHD thesis, Naple University (2009).

[57] P. Cheinet, B. Canuel, F. P. D. Santos, A. Gauguet, F. Leduc and A. Landragin, *Measurement of the sensitivity function in time-domain atomic interferometer*, IEEE Trans. Instrum. Meas. **57** 1141 (2008).

[58] G. Brisebois, *Low Noise Amplifi ers for Small and Large Area Photodiodes*, Design Note 399, Linear technology.

[59] A. Gauguet, B. Canuel, T. Leveque, W. Chaibi, A. L. A. Gauguet, B. Canuel, T. Leveque, W. Chaibi and A. Landragin, Phys. Rev. A **80**, 063604 (2009).

[60] R. Geiger, V.Menoret, G. Stern, N. Zahzam4, P. Cheinet, B. Battelier, A. Villing, F. Moron, M. Lours, Y. Bidel, A. Bresson, A. Landragin and P. Bouyer, Nature Communications **2**, 474 (2011).

[61] M. de Angelis, F. Greco, A. Pistorio, N. Poli, M. Prevedelli, G. Saccorotti, F. Sorrentino and G. M. Tino, Eur. Phys. J. Plus **127**, 27 (2012).

[62] J. M. Goodkind, *The superconducting gravimeter*, Rev. Scient. Instr., **70**, 4131-4152 (1999).

[63] F. Sorrentino, K. Bongs, P. Bouyer, L. Cacciapuoti, M. d. Angelis, H. Dittus, W. Ertmer, J. Hartwig, M. Hauth, S. Herrmann, K. Huang, M. Inguscio, E. Kajari, T. Konemann, C. Lammerzahl, A. Landragin, G. Modugno, F. P. d. Santos, A. Peters, M. Prevedelli, E. M. Rasel, W. P. Schleich, M. Schmidt, A. Senger, K. Sengstock, G. Stern, G. M. Tino, T. Valenzuela, R. Walser and P. Windpassinger, *The Space Atom Interferometer project: status and prospects.*, Journal of physics, Conference series **327**, 1-13 (2011).

[64] G. M. Tino and F. Vetrano, *Atom interferometers for gravitational wave detection: a look at a "simple" configuration*, Gen. Relativ. Gravit. **43**, 2037-2051 (2011).

[65] G. M. Tino, F. Vetrano and C. Lammerzahl, Special issue on *Gravitational waves detection with atom interferometry*, Gen. Relativ. Gravit **43**, 1901-1903 (2011).

[66] M. Schmidt, M. Prevedelli, A. Giorgini, G. M. Tino and A. Peters, *A portable laser system for high-precision atom interferometry experiments*, Applied Physics B, Laser and optics, **102**, 11-18 (2011).

[67] G. C. Bjorklund, M. D. Levenson, W. Lenth and C. Ortiz, *Frequency modulation (FM) spectroscopy*, Appl. Phys. B, **32**, 145 (1983).

[68] H. J. Metcalf and P. van der Straten, eds., Laser Cooling and Trapping, Springer Verlag, New York, 1999.

[69] P. Cheinet, B. Canuel, F. Pereira Dos Santos, A. Gauguet, F. Leduc and A. Landragin, *Measurement of the sensitivity function in time-domain atomic interferometer*, IEEE TRANS. ON INSTRUM. MEAS., MARCH 24, (2005)

[70] G. M. Tino, *Lezioni di fisica atomica*, Florence University (2001-2012)

[71] J. Le Gouët, P. Cheinet, J. Kim, D. Holleville, A. Clairon, A. Landragin and F. Pereira Dos Santos, *Influence of lasers propagation delay on the sensitivity of atom interferometers*, Eur. Phys. J. D **44**, 419–425 (2007)

[72] X. Balliard, A. Gauguet, S. Bize, P. Lemonde, Ph. Laurent, A. Clarion and P. Rosenbushc, *Interference-filter-stabilized external-cavity diode laser*, Optics Communications **266**, 609-613 (2006)

[73] G. Dick, *Local oscillator induced instabilities in trapped ion frequency standards*, Proc. of Precise Time and Time Interval, pages 133–147, Redendo Beach (1987).

[74] H. Müller, A. Peters and S. Chu, *A precision measurement of the gravitational redshift by the interference of matter waves*, **463**, 926 (2010).

[75] P. Wolf, L. Blanchet, C. J. Bordé, S. Reynaud, C. Salomon and C. Cohen-Tannoudji, *Atom gravimeters and gravitational redshift*, Nature **467**, E1 (2010).

[76] M. A. Hohensee, B. Estey, P. Hamilton, A. Zeilinger and H. Müller, *Force-Free Gravitational Redshift: Proposed Gravitational Aharonov-Bohm Experiment,* PRL **108**, 230404 (2012)

[77] C. Lämmerzahl and C. J. Bordé, *Rabi oscillations in gravitational fields: exact solution*, Phys. Lett. A, **203**, 59 (1995)

[78] K. Marzlin and J. Audretsch, *State independence in atom interferometry and insensitivity to acceleration and rotation*, Phys. Lett. A, **53**, 312 (1996)

[79] P. Storey and C. Cohen–Tannoudji, *The Feynman path integral approach to atomic interferometry. A tutorial*, J. Phys. II, **4**, 1999–2027 (1994)

[80] C. Antoine and C. J. Bordé, *Exact phase shifts for atom interferometry*, Phys. Lett. A, **306**, 277–284, (2003)

[81] Julien Le Gouët, *Étude des performances d'un gravimètre atomique absolu : sensibilité limite et exactitude préliminaire,* PHD thesis, Paris 11 University (2008)

[82] J. M. Hogan, D. M. S. Johnson and M. A. Kasevich, in Proceedings of the International School of Physics Enrico Fermi Course CLXVIII on Atom Optics and Space Physics, edited by E. Arimondo, W. Ertmer, W. P. Schleich and E. M. Rasel (IOS Press, Oxford, 2007), p. 411

[83] G. Möllenstedt and H. Düker, *Beobachtungen und Messungen an Biprisma-Interferenzen mit Elektronenwellen*, Zeitschrift für Physik, **145**, 377 (1956)

[84] G. Möllenstedt and H. Duker H, *Fresnelscher Interferenzversuch mit einern Biprisma für Elektronenwellen* , Naturwiss **42**, 41 (1954)

[85] Xinan Wu, *Gravity Gradient Survey with a Mobile Atom Interferometer*, Stanford (2009)

[86] A. Bertoldi, G. Lamporesi, L. Cacciapuoti, M. de Angelis, M. Fattori, T. Petelski, A. Peters, M. Prevedelli, J. Stuhler and G. M. Tino, *Atom interferometry gravity-gradiometer for the determination of the Newtonian gravitational constant G*, Eur. Phys. Jour. D **40**, 271 (2006)

[87] A. Louchet-Chauvet, T. Farah, Q. Bodart, A. Clairon, A. Landragin, S. Merlet and F. Pereira Dos Santos, *The influence of transverse motion within an atomic gravimeter*, New Journal of Physics 13, 065025 (2011)

[88] F. Sorrentino, A. Bertoldi, Q. Bodart, L. Cacciapuoti, M. d. Angelis, Y. Lien, M. Prevedelli, G. Rosi and G. M. Tino *Simultaneous measurement of gravity acceleration and gravity gradient with an atom interferometer*, Applied Physics Letters **101**, 114106 (2012)